Research Square

Preprints are preliminary reports that have not undergone peer review.
They should not be considered conclusive, used to inform clinical practice,
or referenced by the media as validated information.

Online behavior tuning of anthropomorphic hands through bioinspired design and Virtual Model Control

Lorenzo Vignoli

lorenzo.vignoli@epfl.ch

EPFL

Yu Zhang

ETH Zurich

Fulvio Forni

University of Cambridge

Josie Hughes

EPFL

Article

Keywords:

Posted Date: November 10th, 2026

DOI: https://doi.org/10.21203/rs.3.rs-11676991/v1

License: This work is licensed under a Creative Commons Attribution 4.0 International License.
Read Full License

Additional Declarations: No competing interests reported.

Online behavior tuning of anthropomorphic hands through bioinspired design and Virtual Model Control

Lorenzo Vignoli[1,2*], Yu Zhang[1], Fulvio Forni[2], Josie Hughes[1]

[1]CREATE Lab, EPFL, Switzerland

[2]Control Robotics Lab, University of Cambridge, UK

[*]To whom correspondence should be addressed; E-mail: lorenzo.vignoli@epfl.ch.

Humans constantly modulate the mechanical compliance of their hands to enable complex behaviors, ranging from gentle guitar strumming to high-force hammer manipulation, including robust multi-object handling and dexterous in-hand manipulation. To achieve this, the hand's rich mechanics through the joints and tendon routing are combined with distributed adaptive compliance arising from muscle structures and control. Collectively, these enable the hand's diverse behavioral capabilities and its ability to maintain contact stability under sparse or uncertain knowledge of the contact state. Inspired by this, we propose a new design and control methodology for an anthropomorphic, tendon-driven robotic hand. Our biomimetic mechanical design, comprising artificial skin, biomimetic tendon routing, and series elastic actuation, defines the intrinsic envelope of achievable stiffness, force, and pose, defining the behavioral range. Overlaid on this hardware, a virtual mechanical layer based on Virtual Model Control dynamically modulates the hand's compliance. By emulating virtual springs and dampers through available actuation, this layer shapes how the hand interacts with its environment while guaranteeing interpretability and tunability. Integrating physical and virtual mechanical components, our co-design framework presents a new paradigm for anthropomorphic robotic hands, enabling contact force estimation via motor feedback (proprioception) and greater versatility across a range of interactive behaviors.

Introduction

The ability to modulate mechanical impedance dynamically is central to human manipulation [1]. The same hand that grips a hammer forcefully can strum a guitar with delicate, expressive control or perform dexterous in-hand re-grasping. However, each of these behaviors calls for a different hand stiffness. This versatility arises from muscles, tendon routing, compliant skin, and rigid bones, combined with continuous and adaptive regulation of the hand's distributed compliance through muscles and actuation mechanisms. Within a single task, the governing variable also shifts: force and position guide the approach to an object, whereas after contact, stiffness shapes the interaction and its sensory feedback [2]. The synergy between the mechanics and control of the human hand lies at the core of hand function, and robotic manipulation likewise requires hardware and control that are collectively designed to regulate force, position, and stiffness while remaining physically resilient and dexterous [3].

The physical structure of the human hand determines the limits of its versatility, dexterity, and safety [4]. These limits arise from the directional passivity of the anisotropic joints, the stiffness and passivity of tendons and muscles, and the compliance and contact stability of the skin [5], which together set the range of achievable force-displacement characteristics. Passivity is central, because it keeps contact with unknown objects stable without a model of the environment, even under sparse or uncertain information [6]. Within these bounds, antagonistic muscle co-contraction regulates stiffness, pose, and force online [7, 8], varying compliance within the passive dynamics of the muscle-tendon system rather than overriding them. This capacity distinguishes human hands from their robotic counterparts, which rely largely on position control [3].

Reproducing this capacity in robotic hands has been approached from both hardware and control perspectives. Tendon-driven hands mirror human physiology and, unlike directly driven

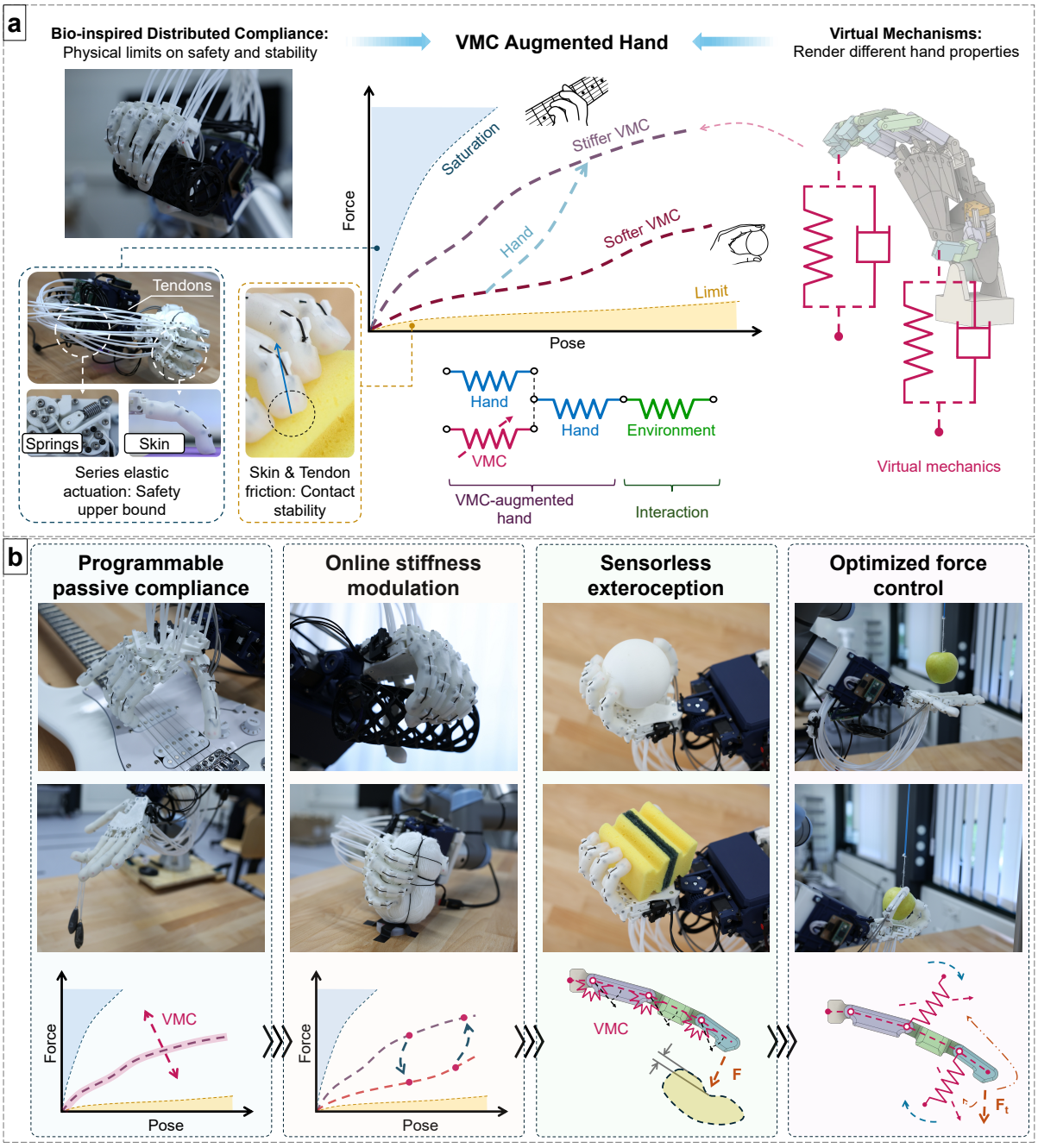


Figure 1: **Overview of concept and capabilities of Virtual Model Control in manipulation**. **a** Compliance augmentation architecture of the tendon-driven hand, with interaction and sensing capability. **b** Demonstration of behaviors enabled by VMC on a single hardware platform: programmable passive compliance of virtual elements, online stiffness modulation in-hand and during dynamic tasks, perception of applied force and environmental stiffness, and model-based force adaptation.

systems, combine low end-effector inertia, which reduces impact forces, with high dexterity and the capacity to regulate fingertip contact dynamics [9]. Underactuated designs with flexure or multi-material joints reproduce human-like nonlinear joint behavior through their mechanical structure rather than through control [10], and their joint design programs the passive response, for example the grasping behavior [11] or the musical playing style [12]. However, unlike human hands, a robotic hand's mechanical response is typically fixed by its fabrication parameters and cannot be dynamically modulated online.

Variable stiffness actuators (VSAs) can be introduced to modulate the force-displacement relationship online by changing the stiffness of a physical elastic element [13, 14]. VSAs have been integrated into tendon-driven systems through shape-memory materials [15, 16] and variable spring geometry [17]. However, the inclusion of VSAs in to a hand increases significantly the mechanical complexity, adds weight and volume, and limits the control bandwidth preventing scaling to tendon-driven anthropomorphic hands [18].

Alternatively, impedance control offers software-based compliance [19, 20, 21]. By shaping the apparent stiffness, damping, and inertia of the end effector [22], it allows the relationship between motion and force to be tuned independently [23, 24]. It has reproduced human-like adaptation of force and impedance [25] and been combined with passive joint compliance for robustness against load peaks [26]. In dexterous hands, it has been applied both at the fingertip level [27] and at the object level, compliantly positioning a grasped object in-hand while distributing the internal forces among the fingers [28]. Despite its success, a systematic, task-oriented methodology for determining the optimal, task-specific impedance of each finger remains lacking. This gap compounds the classical challenge of distributing contact forces across multiple fingers [29, 30]. Furthermore, many impedance controllers cancel the natural dynamics to impose the desired behavior, and therefore rely on accurate models, which are notoriously difficult to obtain for compliant, tendon-driven systems [31]. In addition, not all formulations

of impedance control are passive, which can compromise contact stability [32].

To overcome the trade-off between setting stiffness in hardware and in control, we propose a unified approach to the design and control of anthropomorphic, tendon-driven hands, in which the mechanics and control are both represented within a single mechanical framework (Fig. 1**a**). The mechanical design sets the operational envelope, passivity, and physical response through compliance distributed throughout the hand [33]. Series elastic actuation, through tendons and in-line springs, sets the upper bound by capping the stiffness reached during contact, from both the virtual mechanisms and the environment. This makes the hand physically resilient and safe, and lets it exploit contact rather than avoid it, unlike conventional position-controlled hands. Skin and tendon friction set the lower bound, providing mechanical stiffness and damping where a controller would struggle and hence inherent contact stability. Within this envelope, a virtual mechanical layer based on Virtual Model Control (VMC) [34] adds virtual springs and dampers that dynamically modulate the stiffness, force, or pose at the fingertips.

VMC has previously been applied to compliant reaching and passivity-based tuning on robotic manipulators [35, 37, 38]. In this work, we extend VMC to multi-fingered, tendon-driven hands, introducing the online stiffness modulation and proprioceptive sensing that dexterous manipulation requires. In doing so, we can now obtain dexterous grasping and manipulation by attaching virtual springs and dampers from the fingertips to an object or task. Rather than imposing a single impedance at the end effector or object, this assigns each finger its own virtual elements, whose parameters are set per task and can be optimized online, and the internal forces between fingers follow directly from their configuration. Because each element is attached to a specific hand segment with a defined stiffness, compliance is placed exactly where the task requires it, which guarantees interpretable behavior. Varying the anchoring points and strengths of these elements significantly adapts the hand online, so that most tasks, even complex motions such as in-hand manipulation, are achieved by modifying a single virtual mechanism rather than

through complex kinematic or impedance control. Unlike impedance controllers that cancel the dynamics, VMC acts on the kinematics and leaves the natural dynamics in place, reducing the need for a high-fidelity dynamic model [36]. Mechanical compliance filters high-frequency disturbances, providing robustness, while VMC shapes slower objectives such as stiffness and force tracking. The hand can thus span the force-displacement space, from stiffness programming to position or force control, while maintaining passivity [6], and tuning the virtual mechanisms defines a task-optimized hand configuration on a single fixed hardware platform. In addition, combining the known virtual mechanisms with the mechanical model allows fingertip contact forces to be estimated from motor feedback (proprioception) alone, without tactile sensors. This estimate can in turn drive online optimization of the virtual mechanisms to adapt fingertip forces in response to sensed contact.

To demonstrate our approach, we first evaluate the approach on a single-finger test bed, to characterize low-level behavioral properties, before translating this to our designed ADAPT hand to assess their effect on manipulation tasks (Fig. 1**b**). We demonstrate that programmable passive compliance lets the hand vary guitar-playing styles online, and show that online stiffness modulation supports stable in-hand manipulation and dynamic grasping of soft objects. We validate the resulting sensorless exteroception, a proprioceptive contact-force estimate, against a ground-truth load cell and use it to classify object compliance. Finally, independent optimization of force, position, or stiffness improves tracking performance during online grip-force adaptation while grasping and picking objects. Together, these results show that when the physical mechanics set the bounds and virtual mechanisms tune behavior within them, a single biomimetic hand can move continuously between delicate, forceful, and dexterous interactions.

Results

Virtual Model Control allows the passive response of the hand to be adapted online, from a kinematic model of the transmission alone. We demonstrate this on our adapted version of the ADAPT Hand V3 [39, 40] and on a single-finger test bed which reproduces its index finger (Fig. 2**a**). The ADAPT Hand is a 15-degree-of-freedom (DOF) anthropomorphic hand with five digits. The index, middle, ring, and pinky fingers share the same structure, while the thumb has two additional DOFs at the carpometacarpal (CMC) joints. Its tendon-driven actuation, silicone skin, and a spring in series with each metacarpophalangeal (MCP) joint set the range within which the passive response of the hand can be shaped [33]. The series springs bound the maximum joint stiffness, while the skin, beyond providing a baseline compliance, deforms under contact to increase the contact area and improve grip stability.

The wrist is mounted on a UR5 arm, controlled in position, and in each finger the MCP joint is actuated independently while the proximal interphalangeal (PIP) and distal interphalangeal (DIP) joints are constrained to a common rotation. The finger test bed shares the same silicone skin, tendon routing, and joint design as the hand's index finger, driven via Bowden cables. The PIP and DIP move together through the same actuator. The finger test bed is mounted on a UR5 robot that presses against a load cell, used here as ground truth, recording the normal force with respect to the covered distance.

The robot hand is controlled with VMC, thus combining two sources of compliance: the mechanical properties of the hardware, thanks to tendon-based actuation, silicone skin, and a spring in series to the MCP joint, and the virtual properties set by VMC. Virtual elements are superimposed onto the kinematic structure of the hand and mapped to its actuators according to how these forces interact with the robot's own state, allowing predictable dynamic behaviors to be replicated (Fig. 2**b**). Online tuning of virtual parameters allows modulation of compli-

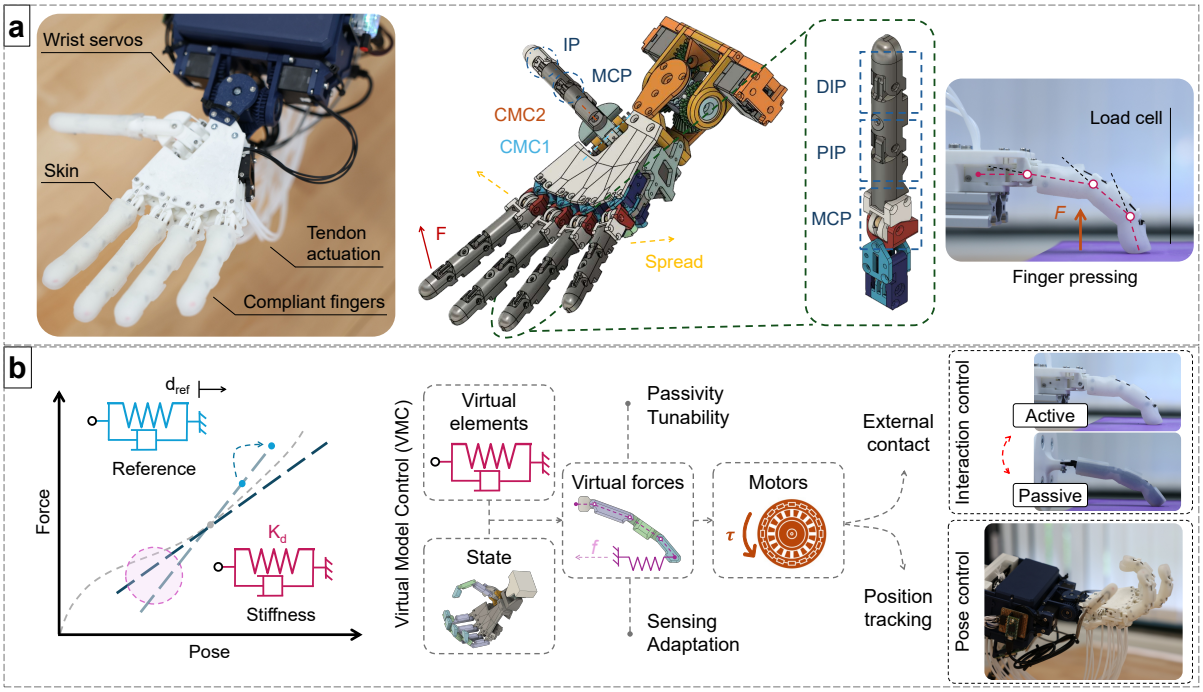


Figure 2: **Control framework on the compliant ADAPT Hand**. **a** Detailed hand hardware and actuation, with finger detail and test bench. **b** Virtual Model Control (VMC) scheme and virtual elements. The control architecture interacts with the state to produce virtual forces, which are then mapped to the motors for interaction control and position tracking.

ance as a function of known control inputs, differentiating the behavior of the fingers during in-hand manipulation or applying different, time-varying wrenches to the grasp. Knowledge of the control architecture, merged with a prior estimation of the tendon-driven transmission loss, allows sensorless force estimation and environmental compliance classification. The same differentiable model used for sensing can also close the loop with the virtual elements, optimizing where on the kinematic structure they act and how their parameters evolve online, to set different robustness to external forces according to the desired grasp force.

To demonstrate this method, we systematically demonstrate the control capabilities on single fingers, evaluating tuning of passive properties, online adaptability, force and stiffness sensing, and contact force regulation. Extending this control to a full hand, we then show how these capabilities translate into robust and varied manipulation, spanning music playing, grasping, in-hand manipulation, and sensor-free force control. In all experiments we introduced friction compensation, consisting of continuous motor wobbling to minimize static effects [41]. This mirrors physiological tremor, thought to keep the motor system in a dynamic rather than static friction regime [42].

Programmable passive compliance

Programmatically varying the passive compliance of the hand is important for passivity-based environmental interactions, which underpin many manipulation and exploration tasks. This lets a hand yield to conform to a surface of unknown shape at contact, modulate the resistance and sound produced while playing an instrument, and absorb impacts or safely bear added weight. To achieve programmable passive compliance on our robot hand, its natural properties are augmented with different virtual elements, including springs and dampers, both cartesian and torsional, carts, and repulsive elements. These elements can be intuitively added to the system to change behaviors [43]. If these elements do not change over time, the controlled robot

can be thought of as a tunable passive system, whose energy does not increase over time and which in turn creates predictable responses while maintaining stability. VMC provides tunable robustness to unplanned contact and absorption of interaction energy, acting as a bidirectional filter for noise and deformations.

To characterize the capacity of our VMC-augmented robot to show programmable passive compliance, we measure the force-displacement profiles of the single finger under different control conditions. Extending this to the full hand, we show how, using the same hardware, we can change how the hand interacts with the environment, through the scenario of wrist-driven guitar playing.

Because a hand must accommodate objects whose shape and stiffness are unknown before contact, dexterous manipulation requires a compliant response that can be shaped independently of the underlying hardware. We first ask how much of this shaping is available through VMC applied to the finger test bed, using the load cell plate to measure the fingertip normal force (Fig. 3). We evaluate this capacity to modulate the magnitude of the change in joint space and task space, the robustness to the initial contact pose, and the programming of directionality.

To first evaluate modulation of joint-space passive compliance, the finger is augmented by virtual torsional springs placed at the MCP, PIP, and DIP joints (Fig. 3**a**), always paired with dampers. All of these share the same stiffness K_θ, regulated during the experiments; the reference angle of each spring, its unloaded target angle, is at 30°. The UR5 always starts from the same initial pose, while the control elements are continuously applied to the system. The arm descends for 20 mm, after which it is lifted and brought back to the initial pose. We plot fingertip normal force, measured by the load cell, with respect to the vertical distance moved. Each measurement is repeated 5 times for reproducibility. We obtain different curves varying K_θ up to $0.6\ \mathrm{N \cdot m/rad}$, up to which we notice that the stiffness of the system remains the same, although the initial force slightly increases. We define this as the *saturation* effect. Because

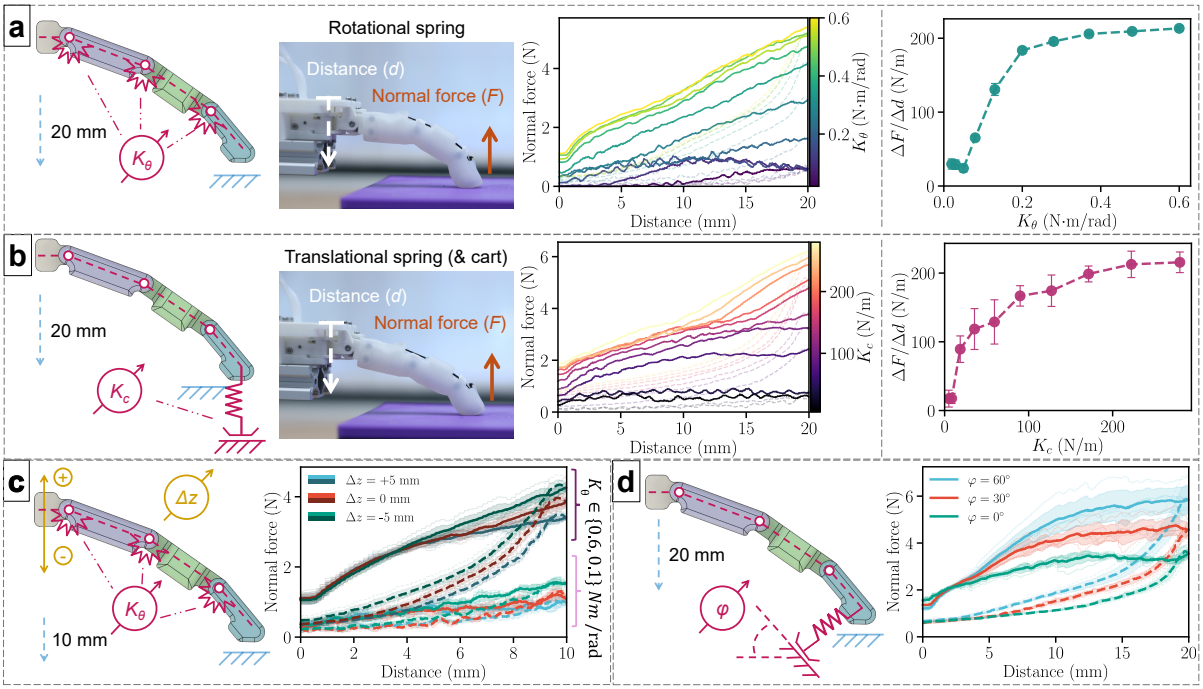


Figure 3: **Passive compliance characterization on the single finger platform and related control architectures**. **a** Torsional virtual springs at the finger joints (MCP, PIP, DIP), composition with real compliance, and *saturation* effect. Loading (solid) and unloading (dashed). **b** Fingertip virtual spring (rest position fixed in the wrist frame) with sliding cart and composition with real compliance. **c** Influence of the initial finger pose in the force-displacement profiles for two different torsional springs, either soft or stiff. **d** Influence of the fingertip cart direction on the passive response of the robot. Across all figures, parameter symbols crossed by a diagonal arrow denote virtual properties that are tuned or adapted online.

the force-distance curves are mediated by the static contribution of the finger elements, including skin, joints fabrication, and tendons, the effective stiffness of the system $\Delta F/\Delta d$ exhibits a nonlinear behavior as K_θ progresses. Moreover, this has a lower bound for small values of the control stiffness. The system can be, as first approximation, modeled as the superposition of three stiffnesses (Fig. 1**a**): a VMC layer on top of the hand, which modulates the compliance transmitted from the motors to the system, a spring parallel to this layer that increases the achievable stiffness and introduces a lower bound, and a series spring that limits the achievable properties to a stiffness of around 200 N/m. Furthermore, due to the static friction between the silicone and the plate of the load cell, the force-distance curve exhibits a hysteretic behavior while the arm rises, with lower forces on average (Supplementary Movie 1).

To show the versatility and intuitiveness of the control architecture we attached a task-space cartesian spring to the fingertip, with its rest position fixed in the frame of the UR5 wrist mount. A cart constrains the spring to act only along this vertical direction, letting the horizontal component of the fingertip's own trajectory pass through unconstrained (Fig. 3**b**). As a result, all the non-vertical force components are zeroed during motion. The spring stiffness K_c spanned values up to 250 N/m. The effective stiffness shows nonlinear behavior as a function of the virtual stiffness, with a saturation effect that settles at very close values compared to the rotational springs setup (Supplementary Movie 2).

During a grasp the finger meets the object at a pose that is not known beforehand, so we test whether the modulation authority shown above still holds when the initial contact pose changes. In this experiment, the initial arm pose was shifted either up or down by 5 mm, with the total descent reduced to 10 mm, to lead to different finger poses. In Fig. 3**c** we compare the curves corresponding to the shifted initial conditions with the baseline set to the usual starting point. The procedure was repeated for K_θ as 0.6 N $\cdot$ m/rad and 0.1 N $\cdot$ m/rad. The stiffness of the finger remains consistently higher in the former case, while in both cases the stiffness increases

when the finger starts closer to the load cell, as the torsional springs are more compressed from the beginning. The ordering between soft and stiff is therefore preserved across poses.

The virtual elements allow full control of passivity, not only in terms of stiffness modulus but also in directionality. For example, by adding a cartesian spring at the fingertip, attached to a cart with tunable direction ϕ, we can change the axis along which the force-displacement model acts on the robot (Fig. 3**d**). The stiffness of the spring is kept constant. The force increases for higher cart angles due to the interplay between the finger kinematics, which is bent, and the mapped virtual force. Since contacts occur at orientations that depend on the object and on how it is presented to the hand, tuning magnitude and direction together allows the compliance to be aligned with the contact rather than with the finger. The same principle can be applied by tuning the stiffness ellipsoid along the normal direction to the fingertip, as shown later.

The tunability of passive compliance should also shape the grasp's dynamic behavior and how the hand interacts with time-varying loads, and is verified via a guitar playing experiment, where varying the torsional spring stiffness changes both the resistance felt during strumming and the resulting sound. The whole hand is kept in a fixed pose through virtual torsional springs at every joint, which keep the thumb and pinky lifted while the other fingers are bent in a fixed position (Fig. 4**a**). During the approaching phase, these three fingers slip beneath the bass string. Although when the hand is not interacting with the guitar its pose is the same for all control parameters, a higher K_θ offers more resistance during strumming. The hand is then lifted by the arm up to a fixed pose, and this allows releasing of the string. The vibration of the plucked string gives a sound readout of the dynamic interaction. It is recorded by a camera microphone and reported as RMS on arbitrary, common units for the three experiments. The peak value during strumming increases with finger stiffness, consistent with a stiffer virtual spring returning more of the string's elastic energy rather than absorbing it, producing a sharper pluck (Supplementary Movie 3, with audio).

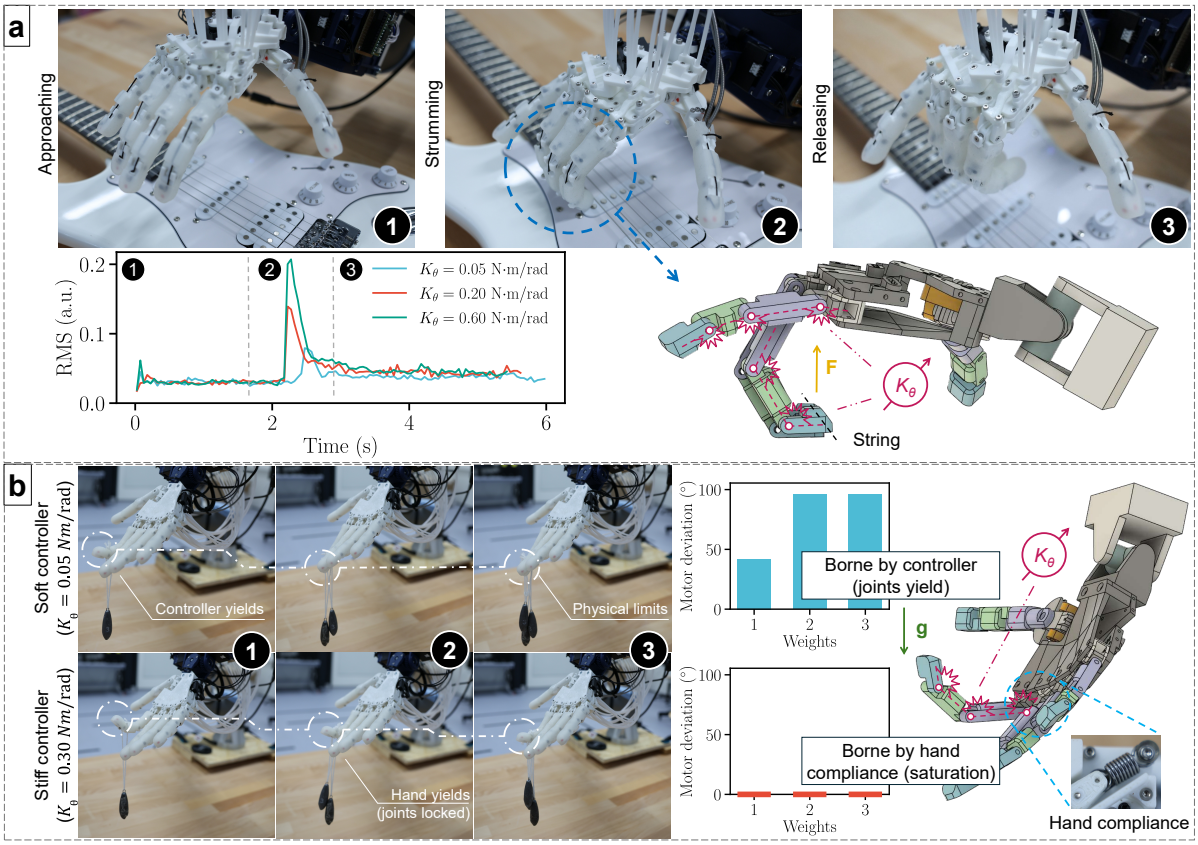


Figure 4: **Effects of passive compliance tuning via Virtual Model Control on full-hand tasks and related control architectures**. **a** Guitar playing with various stiffnesses of the virtual torsional springs and sound RMS (normalized units); photographs correspond to $K_\theta = 0.20$ N · m/rad. **b** Weights bearing with three increasing loading conditions using a soft and a stiff controller.

External loads are shared between control and hardware compliance, and which one yields depends on their relative stiffness. With a soft virtual controller, the load is taken up by the controller. With a stiff one, it is absorbed instead by the hand's own hardware compliance. This defines a safety margin against unexpected or excessive loads that exists independently of what the controller is commanding. This trade-off is validated in Fig. 4**b**. The hand holds a hook grasping pose, where the index is bent to hold a varying weight and an operator iteratively adds three 100 g-loads. This is repeated in two cases: a softer controller, whose compliance overcomes the hand's one, and a stiffer variant that is instead more rigid. The graphs report the cumulated motor deviation across all joints. In the first case the motor encoders record an increasing deviation when adding weights, indicating a deflection of the virtual springs. The deviation remains the same with either 2 or 3 weights as the finger is fully straight already. Conversely, in the second case the virtual spring holds with negligible rotation, while the hand compliance bears the load, leading to a deflection not recorded by the encoders (Supplementary Movie 4).

Online stiffness modulation

A fixed set of virtual elements gives the hand only one interaction response, when dynamic interactions and grasps need temporally varying properties. Approaching an object require a high compliance to conform to an unfamiliar shape. Grasping instead requires a firmer, more stable configuration, with lower compliance and higher rigidity to resist disturbances and support the payload. Different fingers may even need to play these two roles at once, as when some digits shape an object while others already secure it. The hand can access this whole range in real time: rather than replacing the virtual elements introduced above, VMC lets their stiffness and rest configuration be adapted online. This adaptation can happen either across fingers or over the course of a single grasp, so the characterized soft-to-rigid spectrum can be commanded on

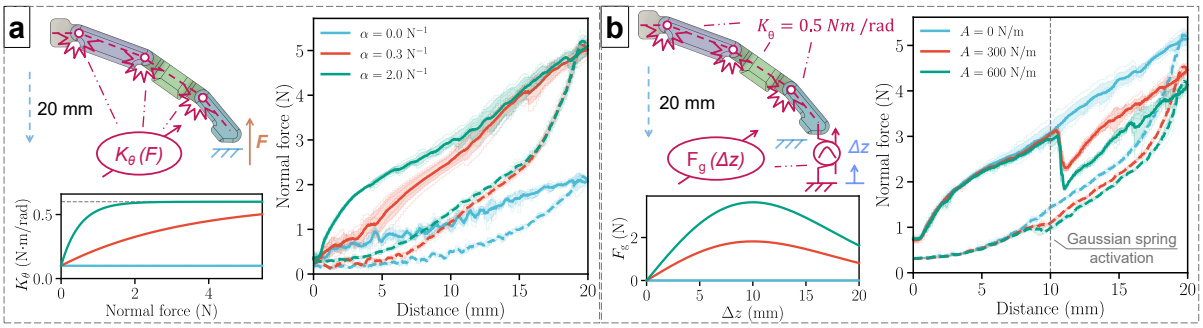


Figure 5: **Online adaptive compliance of the virtual mechanisms on the single finger platform and related control architectures**. **a** Stiffening under contact, with torsional stiffness monotonically increasing with normal force. **b** Effect of introducing a repulsive Gaussian spring on the fingertip (repulsion center fixed in the wrist frame partway through the stroke) on the force-displacement profile.

demand rather than fixed at controller design. To demonstrate this, we carried out a series of experiments on both the finger and hand platforms, first modulating the virtual parameters as a function of a measured or scheduled signal, then adapting them online during in-hand manipulation and dynamic grasping.

Our first stiffness adaptation strategy scales stiffness automatically with contact. A grasp that starts soft and stiffens only once it registers force behaves cautiously during approach and firmly once contact is established, without needing to know in advance when contact will occur. The first experiment on the finger (Fig. 5**a**) implements this stiffening-under-contact behavior: the joint stiffness change is scheduled on the normal force F measured by the load cell, and therefore applied on the fingertip. The control architecture consists of torsional springs attached to the MCP, PIP, and DIP joints, each sharing the same scheduled parameter $K_\theta(F)$. The stiffness of the springs increases monotonically up to saturation, with a slope that increases according to a factor α and is zero if the factor is null. We compare two cases against the constant baseline, the stiffness varying while the arm to which the finger is attached descends. With an intermediate value of α, the force reached by the finger increases considerably as the stiffness

approaches saturation. With an higher value, the force is highest even at low distances, settling at similar values to the intermediate case at greater distances. Notably, although the normal force closes the loop with the load cell output here, the same behavior can be implemented using the force estimation algorithm presented later.

Stiffness properties can also be varied independently of interaction. Because virtual elements compose additively, a new mechanism can be layered onto an existing controller to reshape the response only over part of the stroke, for instance to soften an approach near a known depth without altering the baseline elsewhere. Given the intuitiveness and composition properties of the virtual elements, the controller can be modified online by introducing additional mechanisms that interact with the hand in the same way, further mapping fictitious forces into the motors. We introduce Gaussian repulsive springs in Fig. 5**b** by attaching them to the fingertip while torsional springs remain active at the individual joints. These springs introduce a (passive) repulsive force field F_g that pushes the fingertip away from a fixed reference according to the offset Δz, as shown in the figure. The Gaussian springs are activated halfway through the descent and deactivated halfway through the ascent, reducing the overall force near the reference while leaving the response elsewhere unaffected. Two strengths of repulsion were validated against the baseline controller, showing effective force reduction during the motion.

At the hand level, stiffness regulation is important not only for grasping but also for in-hand manipulation. Dexterous manipulation requires stiffness to be redistributed across fingers or scheduled in time to shape how a multi-contact grasp unfolds. We demonstrate this benefit through two experiments. First, we show that different stiffness profiles can be dynamically assigned to the fingers, resulting in in-hand manipulation without any prior knowledge of the shape of the object or its placement in the hand. Second, we show that tuning the time evolution of the virtual stiffnesses during different grasp phases results in different behaviors when interacting with objects. The controller for both in-hand manipulation and dynamic grasping

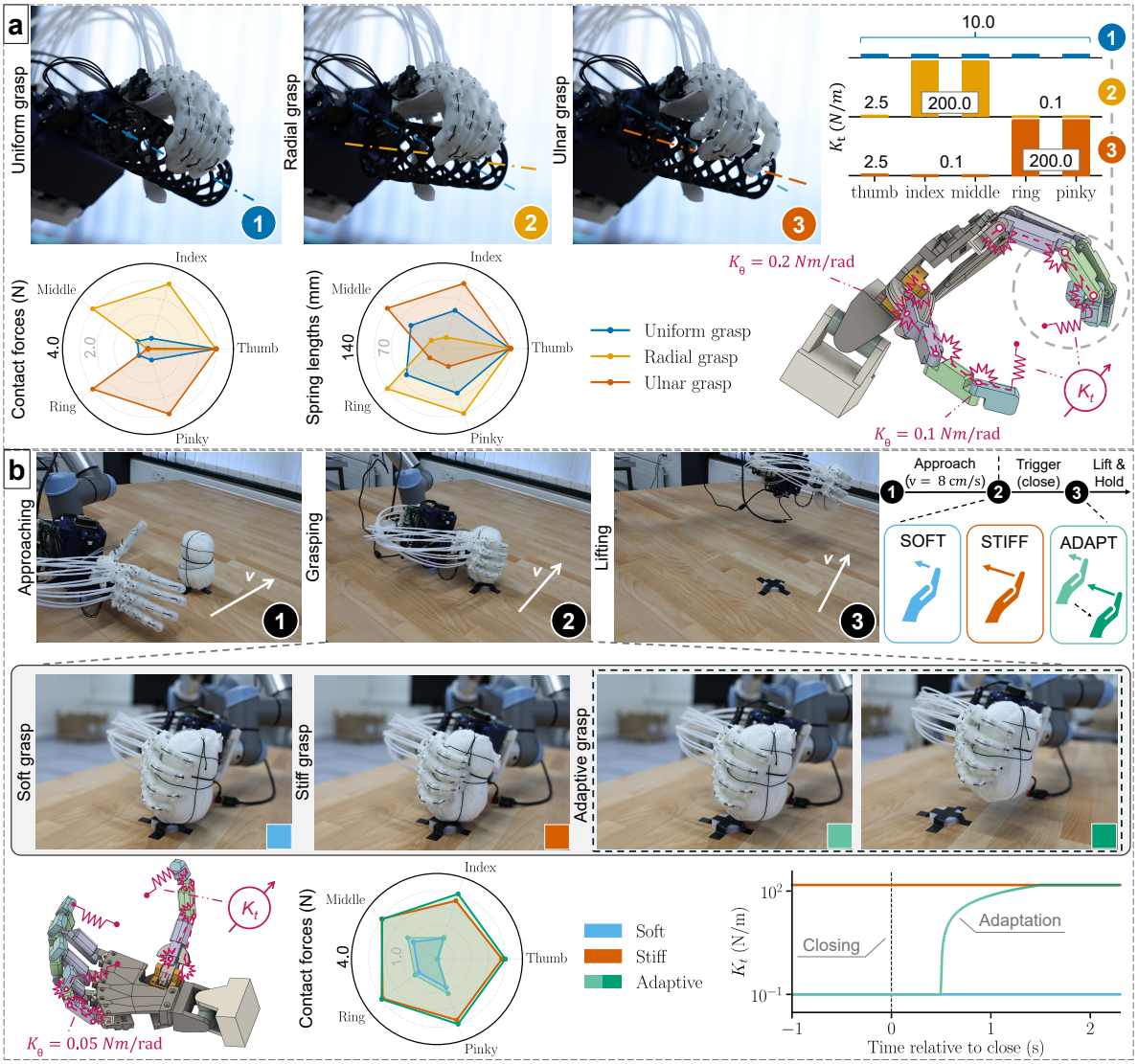


Figure 6: **Grasping capabilities allowed by online compliance tuning of the virtual mechanisms on the hand platform and related control architectures**. **a** In-hand manipulation is allowed by the redistribution of contact stiffness among the fingers to produce predictable contact forces. **b** Dynamic grasping exhibits different object interactions during the closing phase with either a soft, stiff, or adaptive grasp.

consists of lower-stiffness rotational springs at the finger joints, coupled with 5 cartesian springs attached to the fingertips, modulated in stiffness (K_t) during the tasks and whose references mimic the first principal component (PC_1) of human grasp types [44].

In-hand reorientation is typically obtained by planning finger trajectories against a model of the object and regulating the contacts through finger gaiting [45]. We demonstrate that stiffness redistribution alone, with no change in finger position, is sufficient to reorient a grasped object. The fingers are never commanded to a new position; only the stiffness of the virtual elements is redistributed, and the object reorients as the equilibrium of the grasp moves. In-hand manipulation (Fig. 6**a**) is performed using a Thermoplastic PolyUrethane (TPU) helicoidal cylinder as the manipulandum, which is provided to the hand during the grasp by an operator. During the closing phase, denoted as uniform grasp, the fingers wrap around the object keeping a constant and highly compliant cartesian stiffness. This choice allows the hand to conform to the wrapped object, adapting to it without any geometric prior. Then the cartesian stiffness of the fingers is changed linearly, with slow adaptation to limit the amount of energy locally injected into the augmented robot. First, the radial fingers (index and middle) are assigned a very high K_t to increase the exerted force, while the ulnar fingers (ring and pinky) are made more compliant by assigning most of the elastic response to the torsional springs. Then the grasp shifts from radial to ulnar by inverting the stiffness distribution. At the same time, the thumb is made slightly more compliant, as this allows rotation of the cylinder. As the grasp shifts from radial to ulnar, the cylinder's axis tilts accordingly, showing that the redistributed stiffness reorients the manipulandum rather than simply redistributing contact force (Supplementary Movie 5). We show contact forces, estimated with the force sensing algorithm presented below, and cartesian spring lengths per finger according to the three conditions (uniform, radial, and ulnar grasp). Uniform grasp leads to uniform contact forces and spring lengths on all four fingers, while the thumb's contact force is much bigger due to the CMC springs. Conversely, radial and ulnar grasps imply

high forces and low spring lengths on the respective fingers.

The dynamic grasping experiment tests whether scheduling fingertip stiffness over time (soft, stiff, or an adaptive transition between the two) allows a single grasp to conform gently on approach and hold securely once closed (Fig. 6**b**). It consists of the approaching, grasping, and lifting of a yarn ball while the arm moves at a constant speed of 8 cm/s, never stopping the motion when the hand closes (Supplementary Movie 6). The hand starts the motion at a partially flexed posture, then triggers the closing at a known distance. Three grasps were tested: a soft grasp, characterized by low cartesian stiffness, a stiff one, with high K_t, and an adaptive alternative where the cartesian stiffness increases from soft to stiff after the fingers have closed. We plot the estimated contact forces on the five fingers, which are lower for the soft grasp and higher and more uniform for the stiff one. The adaptive grasp, on the other hand, transitions between the two. Although all successful, the various grasps maximize different objectives: the compliant one highly conforms to the object with low deformations and minimal contact force, although less robust to disturbances; conversely, the firmer grasp introduces higher stress and deformation onto the yarn ball, as in the picture, while requiring higher actuator effort. Finally, the adaptive grasp gives the hand time to conform to the object while closing, but increases the hold robustness after that.

Sensorless exteroception

Force control of robotic manipulators allows model-based estimation of the contact wrenches, given kinematic and contact information [46, 47]. As a consequence, open-loop estimation of contact forces and environmental stiffness is possible by merging the virtual elements feedback with the control architecture. The control compliance serves a double purpose, where the deformation that absorbs impacts is the same one that encodes contact force. Using only motor encoders enables both force and displacement estimation during contact, which can be used for

perception, supporting or even replacing costly force sensors as a first approximation (Fig. 7**a**).

We characterize and demonstrate the force sensing capabilities of the hand using the finger test bed (Fig. 7**b**). The control architecture is a set of three rotational springs at the MCP, PIP, and DIP joints, with a fixed rest angle, although the estimation remains valid for a generic set of virtual elements. The model takes as input the estimated contact direction, which in this case is known to be orthogonal to the load cell but can be assumed or sensed otherwise. The virtual elements produce known torques at the motors, which are then mapped through the finger kinematics to the desired force direction. However, tendon losses [48] and unmodeled dynamics introduce a reduction in the applied force, which we model as a linear transformation through a diagonal, less-than-unity transmission gain. To estimate this gain, we pressed the finger on the load cell 200 times, randomly sampling MCP, PIP, and DIP stiffness triplets from $K_\theta \in [0.05, 1.0]$ N $\cdot$ m/rad, and fitted the transmission gain to the acquired data. Across this sweep the fingertip forces span 0.4 to 1.5 N, a range set by the finger's own stiffness bounds and geometry rather than by the sensing method. The resulting model has $R^2 = 83.6\%$, with good accordance between estimated and measured forces. However, the transmission is not perfectly linear, due to friction effects and cable slack or routing. Validation on different VMC architectures is shown in the Supplementary Material.

A grasp that can also tell what it is holding, soft or rigid, gains information useful to plan the rest of the manipulation, without adding a dedicated sensor. When interacting with the environment, the hand can estimate its applied force and measure the resulting displacement of grasped objects. We demonstrate this on three objects of increasing compliance (Fig. 7**c**): a rigid PolyLactic Acid (PLA) sphere, a kitchen sponge, and the yarn ball introduced previously. The control architecture consists of five cartesian springs and dampers, one per fingertip, each attached at a reference pose corresponding to a high-flexion posture along the PC_1 synergy [49]. The stiffness of the four non-opposable digits K_t is kept constant within each phase,

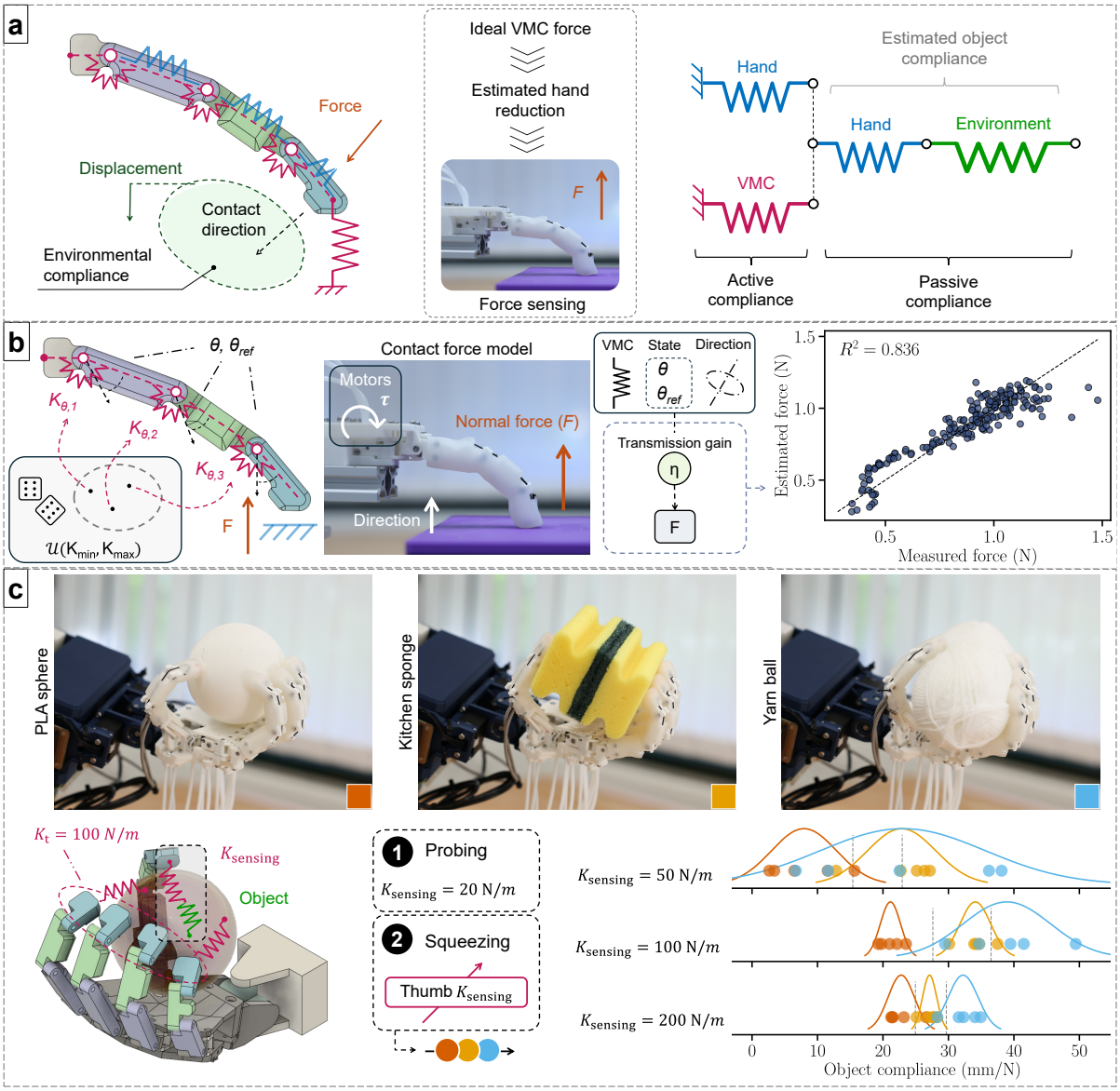


Figure 7: **Model-based sensing capabilities of the Virtual Model Control architecture for force and external compliance estimation**. **a** Working principle of model-based sensing, where the ideal virtual force is scaled by the estimated transmission reduction and the active virtual compliance acts in series with the environment. **b** Force sensing and evaluation of the transmission reduction, combining motor state information with known virtual elements. **c** Compliance sensing of different objects during grasping, exploiting wrench and kinematic variations.

while the thumb stiffness K_{sensing} varies. Compliance is sensed in two phases. During *probing*, the stiffness is set to a low and constant value; once the grasp converges, estimated force and displacement are recorded to establish a baseline. During *squeezing*, the four non-opposable digits remain held at K_t, while K_{sensing} is swept through a range of values, and the displacement with respect to probing at each step is used to estimate the object's compliance (Supplementary Movie 7). Compliance is estimated as the ratio between fingertip displacement and the corresponding force variation, assuming contact to be happening normal to the phalanx. Each experiment is repeated 5 times. Notably, the estimated object compliance includes displacement coming both from the environment and from the compliant hand elements, since only the virtual variations are recorded. This provides more of a classification than an absolute compliance value. At the lowest sensing stiffness, $K_{\text{sensing}} = 50$ N/m, the classification separates the rigid PLA sphere from the two compliant objects, while poorly differentiating sponge and ball. Increasing K_{sensing} leads to increasing forces and displacements, which result in more accurate and consistent classification. Compliance values overall increase due to the hand's own contribution, although the increase is not monotonic, since the saturation effect makes the estimated force variation larger than the effective one at high sensing stiffness.

Optimized force control

Sensorless force estimation shows that, to a first approximation, contact force can be estimated from the motor state alone. Because the same mapping from virtual parameters to fingertip force is built from elementary functions, springs and their kinematic composition, it is differentiable, and the mismatch between estimated and target force can therefore be minimized directly rather than only measured. This turns the model from a sensing tool into a control one, allowing force to be tuned alongside position and stiffness rather than left as a byproduct of a fixed controller. The system can be thought of as a composite mechanism, a passive design over which virtual

elements are placed and can be optimized to satisfy control objectives. In this section, we adapt the stiffness and reference point of the springs to track a desired force profile. Although the resulting wrench is the same, the augmented structure responds differently: tuning compliance implies tuning how the system responds to external perturbations, while shifting the spring operating point modifies the rest pose in the absence of contact. The optimization pathway gives closed-loop control over the full force-displacement relationship (Fig. 8**a**).

The main adaptation algorithm is a gradient descent method which differentiates over the proposed model. As a baseline, we choose a heuristic adaptation method consisting of a scalar proportional update that corrects the virtual model parameters directly from the force error, without evaluating the model's local sensitivity.

We tested the performance of the closed-loop adaptation of the joint stiffness (Fig. 8**b**). We denote this algorithm *force and pose control*, since the spring's rest pose is held fixed, controlling position in the absence of contact, while the joint stiffness is tuned against the load cell force to track contact wrenches. We tracked a square wave, repeating each experiment 5 times. Each plot shows the reference signal, the measured normal force, and its smoothed version $\tilde{F}$, enveloped in its own standard deviation band, which removes the friction-compensation wobbling and lets the underlying trend be appreciated. The gradient descent algorithm minimizes the force loss, defined as the squared error norm, over the stiffness landscape with a given step size; heuristic adaptation instead updates the joint stiffness proportionally to the force error, using the same step size (10^{-4}) for a fair comparison. Performance is quantified by the RMSE between $\tilde{F}$ and the reference, and by the transition time, defined as the time for the response to rise or fall between 10% and 90% of each step's amplitude. On average, including the model sensitivity improved tracking performance by 28% in RMSE and 56% in transition time.

Similarly, we tested the closed-loop adaptation of the operating point (Fig. 8**c**). We denote this algorithm *force and stiffness control*, as it changes the unloaded finger state while keeping

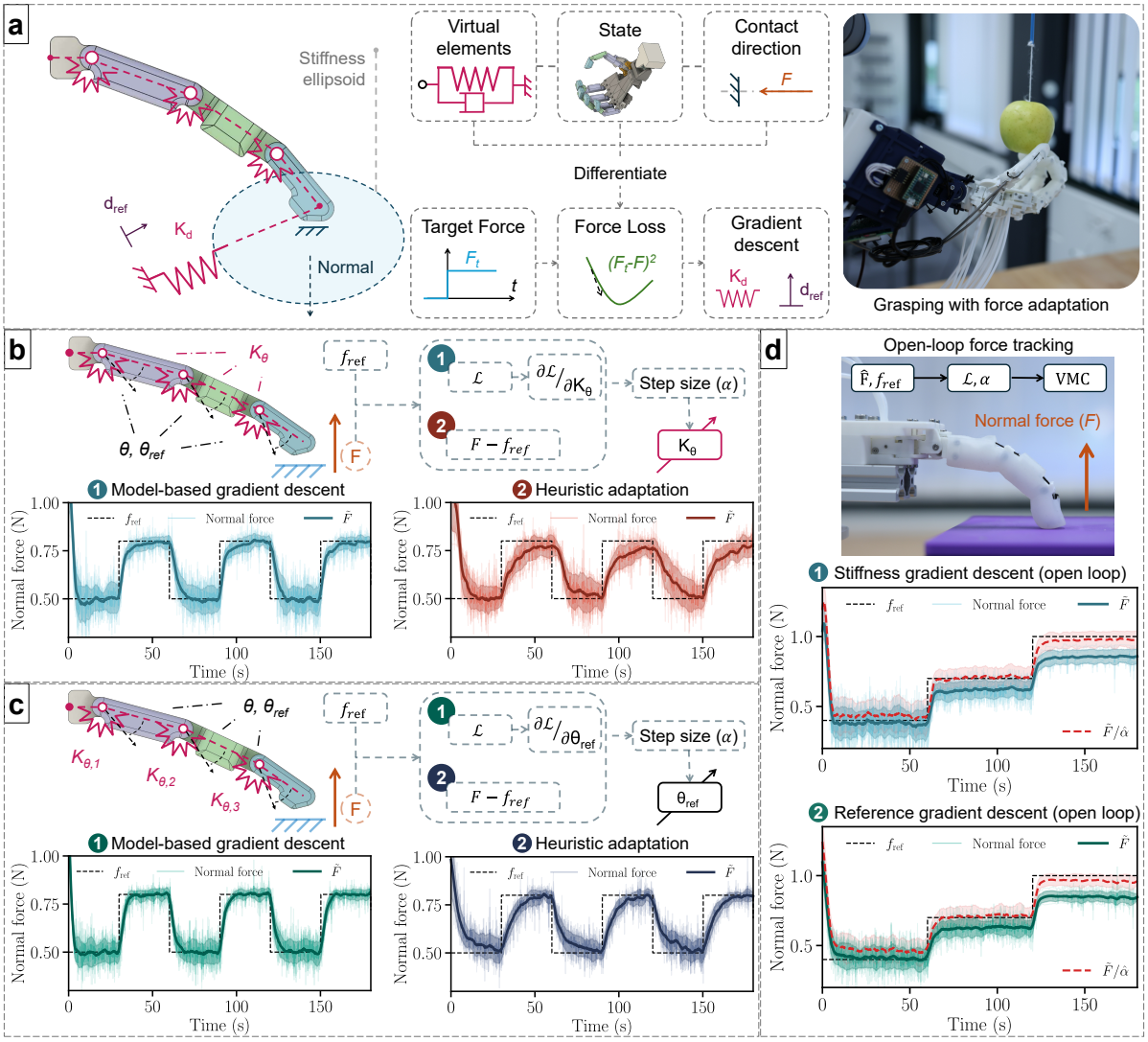


Figure 8: **Force, stiffness and position control via gradient descent algorithms on the differentiable virtual model**. **a** Differentiable adaptation pipeline, where the force loss is differentiated with respect to either the virtual stiffness or the virtual rest position to update the model online. **b** Force tracking via gradient descent versus heuristic adaptation of the virtual element stiffness (*force and pose* control). **c** Force tracking via gradient descent versus heuristic adaptation of the virtual element rest position (*force and stiffness* control). **d** Open-loop tracking of three force setpoints, using model-based force estimation with gradient-based adaptation of either the virtual stiffness or the virtual rest position.

the per-joint stiffness fixed. The gradient is evaluated with respect to the reference position landscape, while heuristic adaptation corresponds to a proportional controller, sharing a step size of $5 \cdot 10^{-4}$. On average, model-based gradient descent improved tracking performance by 23% in RMSE and 60% in transition time.

The VMC sensing capabilities can also be integrated into control to provide open-loop force adaptation. The experimental results are shown in Fig. 8**d**. The finger was asked to track three force setpoints of increasing magnitude, without relying on any feedback, using the same architecture as the closed-loop control, with both gradient-descent algorithms. The measured force followed the shape of the reference at each step, while the model's force estimate slightly overestimated the reference in magnitude. We therefore also plot the rescaled force signal (dashed line), with the scale factor found to be 0.88 for both algorithms. This rescaled curve followed the reference more closely, indicating that the mismatch with the target force was purely multiplicative rather than structural, and could be attributed to higher transmission losses due to either friction or tendon stretch. The model therefore captures the force-displacement relationship reliably even without closing the loop.

Dexterous manipulation requires online tuning of grasping force, modulated by a stiffness that determines how firmly the hold resists being pulled away. We designed the apple grasping experiment (Fig. 9**a**) to demonstrate that online force adaptation lets a grasp's robustness to disturbance be set on demand, holding an unknown object under a sustained pulling force. The same gradient-descent algorithm adapts the estimated holding wrench online. The control architecture consists of five cartesian springs attached to the fingertips, whose stiffness K_t is tuned online to match a desired fingertip force. As with the previous open-loop force estimates on the hand, we assumed contact to be normal to the phalanx. The apple hung from a thread, itself connected to a rubber band acting as a nonlinear spring. The hand first approached the apple from below, then the fingers closed onto the fruit at a fixed cartesian stiffness, after which force was

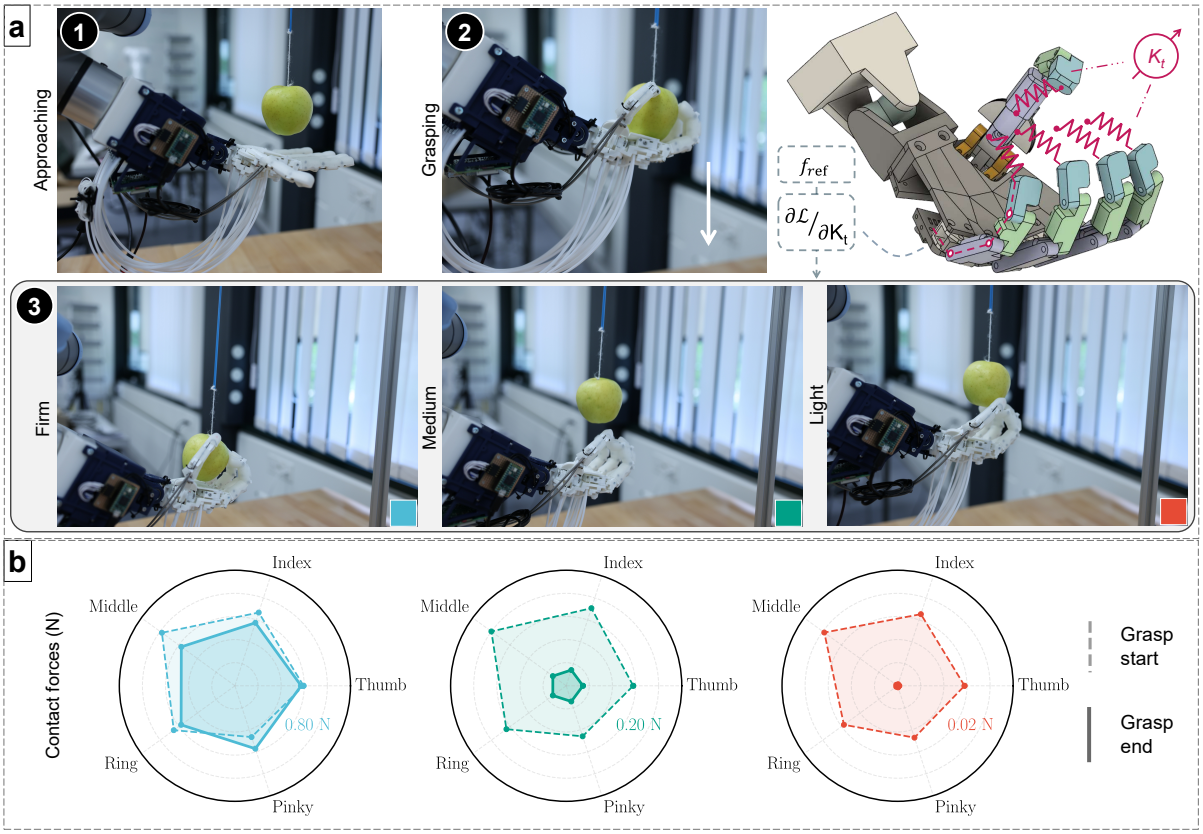


Figure 9: **Apple grasps with online force modulation to three force setpoints and response to the same elastic perturbation**. **a** Experimental phases and snapshots of the hand at release, for the three fingertip force conditions. After grasping the apple, the arm descends and maintains the hold under a firm grasp throughout the elastic disturbance. Under a medium grasp, the hold is lost only once the elastic force exceeds a threshold, while under a light grasp it is lost from the start. **b** Estimated fingertip force distribution for the firm, medium, and light conditions, at the start and end of the apple grasp.

adapted (10^{-5} step size). We repeated the experiment three times, each with a different grasp: firm (0.80 N fingertip force target), medium (0.20 N), and light (0.02 N). After the target was reached, the arm descended by 15 cm while trying to hold the force (Supplementary Movie 8). The elastic band introduced a distance-dependent perturbation that grew as the arm moved from the starting pose, so that the descent swept through increasing disturbance magnitudes. Because stiffer mechanisms reject disturbances more, the hand maintained the hold differently across the three grasps: in the firm case it kept the apple until the end of the descent, in the medium one release happened halfway through, and with a light grasp the hold was lost almost immediately. The algorithm was unaware of the apple's geometry throughout, and adapted force exclusively from motor feedback. We plot the estimated fingertip forces at the start and end of the grasp (Fig. 9**b**). The estimated forces on all five fingers converge to the target. Moreover, the initial cartesian stiffness $K_t = 40$ N/m produced estimated forces already close to the firm wrench, meaning that fingertip force only needs to decrease for the other two grasps.

Benchmarking and controller validation

The previous sections characterized the response of the augmented hand under control, without comparing it to the response of different hardware designed to be compliant. Here we close that gap by using VMC to mimic a specific passive mechanism's interaction behavior in software, aiming to match its tunable stiffness range to a real physical target, and, in the absence of contact, the same virtual elements can instead act as a pure position controller. We benchmark the VMC against two printed fingers whose compliance is fixed at fabrication, and which define the reference force-displacement profile the controller has to reproduce.

The two passive fingers, one soft and one stiff, are fixed physical targets for the controller to match. Their phalanxes share the same length as those of the VMC-modulated finger, as well as width and material (PLA). The two mechanisms differ in the joints, which both maintain

an angle of 30° at rest, but are designed differently with thinner joints for more compliance in the soft finger and thicker ones for more stiffness in the hard finger (Fig. 10**a**). These joints can be described as (nonlinear) torsional springs. We characterized the force-displacement curves by mounting the fingers onto the UR5 arm and descending by 20 mm and back 5 times (Supplementary Movie 9). As with the active finger, these mechanisms exhibited lower average forces when ascending.

The TPU joint stiffness is nonlinear with distance, whereas our controller relies on linear torsional springs at the MCP, PIP, and DIP joints, for simplicity. We therefore consider two cases. In the first, a single linear stiffness is fitted to match the overall compliance of the passive finger over the whole trajectory, without matching the force directly, since we are only interested in reproducing the compliance behavior. In the second, the linear stiffness is instead adapted online to locally linearize the TPU stiffness curve at each point, while simultaneously modulating force by adapting the reference.

The first experiment compares the VMC-tuned finger against the two mechanically passive fingers, matching a single stiffness value for the whole run. To do so, we tune the parameters of a shared VMC architecture, torsional springs at the three finger joints, once per run (Fig. 10**b**). To tune the virtual stiffness, the effective stiffness calibration curve was used to extrapolate the virtual parameters which were in turn fed to the controller during the arm movement, assuming piecewise linear interpolation over the sampled points. The mechanism achieves stiffnesses of 64.0 ± 3.7 and 95.0 ± 4.1 $\mathrm{N/m}$, compared to the passive baselines of 55.6 ± 1.0 and 81.9 ± 1.3 $\mathrm{N/m}$. We report both these values onto the calibration curve and the force-displacement graph comparing TPU and VMC fingers.

The second experiment compares the VMC-tuned finger against the TPU fingers locally, along the whole trajectory rather than at a single stiffness value. To do so, we tune the rotational stiffness K_θ via feedforward stiffness inversion, estimating the local fingertip stiffness K_n from

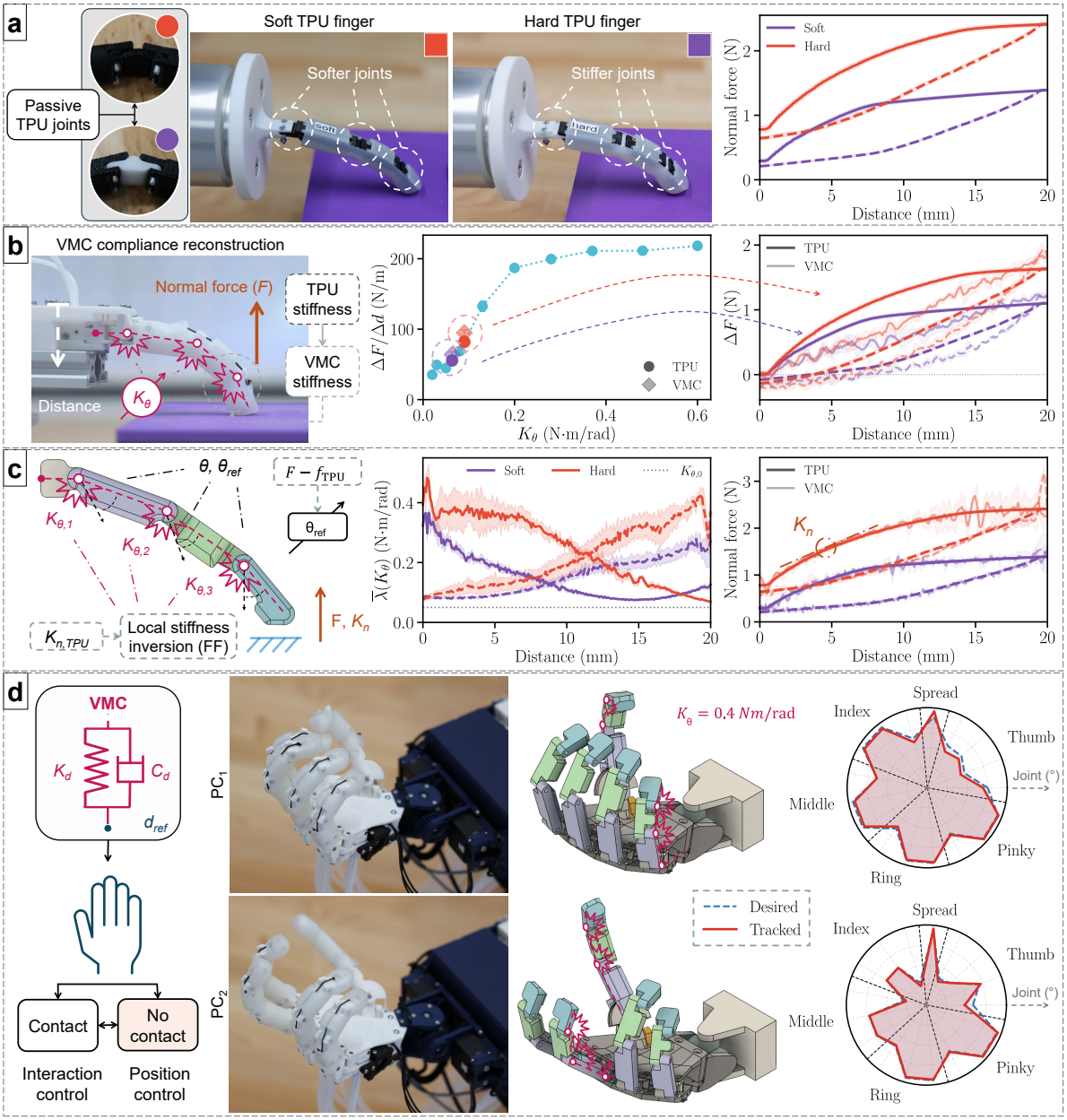


Figure 10: **Controller validation via passive hardware replication and position tracking**. **a** Force-displacement characterization of the soft and hard passive TPU finger joints, loading (solid) and unloading (dashed). **b** VMC compliance reconstruction: calibration between measured TPU stiffness and a uniform virtual stiffness K_θ (left), and resulting force-displacement curves (right), shown relative to each condition's initial contact force. In the hard case, TPU starts at a preload of 0.78 N against 0.38 N for VMC; in the soft case, both start at 0.29 N. **c** Local stiffness inversion: fingertip stiffness K_n is inverted into a joint stiffness matrix (MCP-PIP-DIP), with force further modulated by gradient-tuning θ_{ref}. Average eigenvalue $\bar{\lambda}(K_\theta)$ (left), and force tracking (right). **d** Position tracking without contact: VMC unifies interaction and position control depending on the environment (left), tracked postures PC_1/PC_2 (middle), desired versus tracked joint angles (right). Radar plot axes group joint angles by digit (multiple per digit) and the spread joint, each bounded by its corresponding joint limits.

the TPU curves and projecting it back onto the joints according to the finger's kinematic state. As a result, the system's stiffness is locally equivalent to the (linearized) TPU stiffness. To remain above the lower stiffness bound, a small additional stiffness of $0.05\ \mathrm{N \cdot m/rad}$ is added. We plot the mean eigenvalue of the stiffness matrix as a function of distance for both the descent and ascent phases (Fig. 10**c**), and observe that it mirrors the slope of the TPU force-displacement characterization. To also ensure force tracking, we added a control layer consisting of gradient-descent adaptation of the angular reference; the VMC finger closely tracks the TPU profile during both ascent and descent, with force noise due to friction compensation.

Grasping also requires the hand to reach a prescribed preshape before contact occurs, so the same elements should provide position tracking without a separate controller. When the hand is not grasping, or contact is absent more generally, the VMC layer acts as a pure position controller, mirroring a distributed PD controller. The hand tracks the reference pose by minimizing the overall potential (virtual and mechanical, combined) at equilibrium, with stiffer architectures leading to better accuracy (Fig. 10**d**). To prove this claim, we provide two examples tracking reference poses with a stiff control architecture, consisting of torsional springs on each kinematic joint, even when multiple joints share a single actuator, as with PIP-DIP coupling or finger spread. Both targets are inspired by the first two principal synergies of human grasps [44]. The two radar plots show, for both components, the desired and tracked joint angles clustered by finger, with each axis bounded by the corresponding joint limits (Supplementary Movie 10).

Discussion

To carry out dexterous manipulation, a hand must be able to deal with the forces exerted by objects whose shape, position, and degree of compliance are usually unknown in advance. The controller itself is superimposed on the passive hardware and therefore should not work against

the mechanical characteristics of the body. In this paper we demonstrate that the compliance profile of a tendon-driven hand can be regarded as a control variable rather than as a fixed property determined at design time. Virtual mechanical elements are superimposed on the kinematic structure and mapped to the actuators through virtual work, thereby augmenting the physical compliance rather than compensating for it. The mechanical design sets the stiffness range in which the hand can operate, while the virtual elements shape the response inside this range, in a way that mirrors human manipulation. The mechanical design and the virtual elements therefore serve complementary purposes. Mechanical compliance operates without feedback control and is unaffected by sensor or actuator error, but it is fixed once the hand has been constructed. Virtual compliance can be adjusted in real time and is obtained by addition, although it is limited in bandwidth by the sensors and actuators that implement it. On this basis, the same architecture is able to shape the passive response of the hardware, reproduce compliance that the hand does not naturally possess, manipulate unmodeled objects by redistributing stiffness, estimate contact force and object compliance without dedicated sensors, and regulate grip force in closed loop. All of these functions are derived from the kinematic model alone.

Most grasping strategies assume that a model of the object is available, and therefore that the grasp matrix is known, an assumption that becomes more demanding when the object deforms under contact [50]. Classical force control is likewise built around a known contact geometry [51]. Compliance makes it possible to avoid both requirements. A passive robot that is interconnected with any passive environment remains stable, and physical objects are passive, so preserving passivity removes the need for an object model and turns compliance into a decision that is taken before any control action. A rigid hand responds identically regardless of what it touches, whereas a compliant hand adopts a pose that depends on the object. Our control method shapes virtual elements within the range allowed by the mechanical design, which gives programmable, predictable, and optimized behavior when grasping and manipulating objects.

Because each virtual element is attached to a specific hand segment, the allocation of stiffness across the hand remains explicit and physically interpretable. The method is general and can be applied to realize the desired behavior of any passive hand whose kinematics and transmission are known. Virtual Model Control provides an intuitive framework in which the compliance of the hand can be programmed for each task, including in-hand reorientation and dynamic grasping, without prior knowledge of the shape of the object. In addition, onboard instrumentation can be reduced or complemented by estimating contact forces and inferring properties of the touched object. Finally, the desired grasping forces can be imposed by optimizing the magnitude and placement of the virtual elements.

These properties are well suited to settings in which objects are variable, poorly modeled, or fragile, and where adding sensors to the hand is impractical. Food and agricultural handling is one example, since items differ in size and compliance and tolerate only a narrow band of contact force, which is better respected by a grasp specified in terms of force than of finger position. The absence of additional sensors is also an advantage for prosthetic and assistive hands, where mass, cost, and the fragility of surface-mounted electronics are limiting factors. At the same time, passivity by construction is useful in shared workspaces and in teleoperation, where stability has to hold against an environment that has not been characterized beforehand.

There are a number of limitations that come with this lightweight approach. Passivity is only guaranteed for elements that are frozen in time. Every online modulation of stiffness or reference injects energy, so the adaptation of these elements has to be kept slow relative to the interaction in order to preserve passivity. For the sensing, we assume that contact is always normal to the phalanx, which is the most likely outcome during grasping. Finally, the recorded tendon displacement combines the deflection of the object and of the hand, so compliance sensing ranks objects rather than measuring them. These trade-offs and limitations could be addressed through changes to the VMC method and formulation. Explicit energy accounting,

for instance through a tank budgeting the work done by varying stiffness, would allow faster modulation [52]. Estimating the contact normal online would extend the sensing model beyond enveloping grasps, and a calibrated model of the compliance of the hand itself would make it possible to quantify object compliance. Changes to the hardware, such as stiffer or softer series springs at the MCP joints or a different skin material, could shift these physical limits and extend the approach further. Beyond this hand, since the mapping only requires the kinematics and a transmission model, the same construction can be applied to other compliant systems. In all cases, the controller behavior remains traceable to a small set of mechanical choices, namely springs, dampers, and their references, rather than to a black-box mapping, which makes the approach intuitive and explainable.

Methods

Experimental platforms

Experiments were performed on two platforms sharing the same finger design, actuation principle, and control stack. The full system is the ADAPT Hand [39], an anthropomorphic tendon-driven hand equipped here with modular fingers from a benchmarked design [40]. Of its fifteen actuators, thirteen are torque-controlled and enter the virtual model controller: four for the thumb (CMC1, CMC2, MCP, IP), one driving the spread of all four fingers, and one MCP and one PIP actuator per finger. The two wrist actuators are held in position mode and excluded from the controller. Mechanical compliance is distributed rather than localized [33], arising from the elasticity of the Bowden routing of the tendons, from a spring in series with each MCP joint, and from the silicone skin covering the phalanges. Phalanges are printed in PLA.

The second platform is a single-finger test bed reproducing the index finger, with the same skin, tendon routing, and joint design. Two actuators drive three joints: one commands the MCP, the second the PIP, and the DIP follows the PIP through a mechanical mimic coupling.

The finger is mounted on a UR5 arm commanded over RTDE. Normal contact force is measured by a load cell read through HX711 amplifiers by an Arduino.

All actuators are Dynamixel XC330-T288-T units operated in current mode, addressed through ROS2 Humble on a laptop, with the USB latency timer reduced to 1 ms. The virtual model controller runs at 900 Hz on the single finger and at 330 Hz on the full hand, the difference reflecting the number of actuators polled per cycle.

For the benchmarking experiments, two additional passive fingers were fabricated, matching the test bed's phalanx dimensions and material (PLA), with joints in Thermoplastic PolyUrethane (TPU) and the same silicone skin, one softer and one stiffer, serving as fixed physical references.

Virtual Model Control

Virtual Model Control augments a robot by attaching fictitious mechanical elements to its kinematic structure and mapping the forces they generate onto the actuators through virtual work [34, 35]. The controller does not command a trajectory, as it specifies a mechanism that the robot is asked to behave as though it carried. This distinguishes the approach from impedance control, which shapes apparent dynamics by usually canceling the natural one [21, 22]: here no dynamic model is required, only the kinematics enter the mapping, and the physical compliance of the hand is left in place rather than compensated away. For a tendon-driven hand, whose dynamics are dominated by friction, routing and distributed elasticity that no identified model captures well, this is the decisive practical difference.

Throughout, $\mathbf{q}$ denotes the vector of *actuator* angles, not of joint angles $\boldsymbol{\theta}$. This distinction is essential because the mapping between the two is a property of the tendon transmission rather than the link geometry itself. Accordingly, $\mathbf{J}_{\boldsymbol{\theta}} = \partial\boldsymbol{\theta}/\partial\mathbf{q}$ is a transmission Jacobian mapping actuator displacements to joint displacements, while $\mathbf{J}_x = \partial\mathbf{x}/\partial\mathbf{q}$ composes the transmission

with the link kinematics to describe the Cartesian position $\mathbf{x}$ of a point rigidly attached to the hand. Treating tendon actuation as a distinct kinematic and static stage in this way follows from the standard formulation for multifingered hands [53]. The formulation that follows is independent of the particular geometry.

A virtual element is specified by a stiffness $\mathbf{K}_d$, a damping $\mathbf{D}_d$ and a rest configuration $\mathbf{d}_{\text{ref}}$, all defined on a generalized coordinate $\mathbf{d}$ with Jacobian $\mathbf{J}_d = \partial\mathbf{d}/\partial\mathbf{q}$. The coordinate is unrestricted: it may be a joint angle, a fingertip position, a distance between two points on the hand, or any differentiable function of the configuration. Any number of elements, defined in any combination of coordinates, contribute additively to the actuator torque. For linear elements,

$$\boldsymbol{\tau} = \sum_i \mathbf{J}_{d_i}^T \left[\mathbf{K}_{d_i}(\mathbf{d}_{\text{ref},i} - \mathbf{d}_i) - \mathbf{D}_{d_i} \mathbf{J}_{d_i} \dot{\mathbf{q}} \right]. \tag{1}$$

Additivity is not incidental: a controller can be assembled by superposition, each element contributing an effect that can be reasoned about in isolation, and elements living in different coordinate spaces combine without a change of formalism. The consequences at the point of contact are made quantitative later.

Damping is specified per element rather than left to the hardware, but is kept small. Tendon-driven transmissions already dissipate substantially through their routing, unlike other manipulation hardware, which is often built with low intrinsic damping and must obtain any damped behavior from control [54].

Each spring is defined not only by the force it returns but by the energy it stores. Writing $\mathbf{e} = \mathbf{d}_{\text{ref}} - \mathbf{d}$ for its deflection, an element is conservative when its force derives from a storage function, $\mathbf{F} = -\partial U/\partial\mathbf{d}$ with $U \geq 0$ and $U(\mathbf{0}) = 0$. This is the property on which everything below rests, so we state $\mathbf{F}$ and U for each element used here. The linear spring returns $\mathbf{F} = \mathbf{K}_d\mathbf{e}$ and stores $U = \frac{1}{2}\mathbf{e}^T\mathbf{K}_d\mathbf{e}$. Constraining that spring to a cart, so that it acts only along a single admissible direction $\mathbf{n}_c$, amounts to projecting its stiffness and damping on both

sides through the rank-one projector $\mathbf{P}_c = \mathbf{n}_c\mathbf{n}_c^T$. The force becomes $\mathbf{F} = \mathbf{P}_c\mathbf{K}_d\mathbf{P}_c\mathbf{e}$ and the stored energy $U = \frac{1}{2}\mathbf{e}^T\mathbf{P}_c\mathbf{K}_d\mathbf{P}_c\mathbf{e}$, which is always non-negative and stores nothing in the constrained directions. The Gaussian repulsive element, used to reshape the force response over a bounded region of the stroke while leaving it unchanged elsewhere, acts on the offset $\Delta\mathbf{z}$ from the repulsion center,

$$\mathbf{F}_g = A\exp\left(-\frac{\|\Delta\mathbf{z}\|^2}{2\sigma^2}\right)\Delta\mathbf{z}, \qquad U_g = A\,\sigma^2\exp\left(-\frac{\|\Delta\mathbf{z}\|^2}{2\sigma^2}\right) \tag{2}$$

and is a bounded potential of maximum $A\sigma^2$: it can store only a finite amount of energy, which is what makes it safe to superimpose on an existing controller. Deadzone springs keep the joints inside their mechanical range without affecting the response elsewhere. With limits $[\theta_-, \theta_+]$, each returns $\tau_{\text{lim}} = K_{\text{lim}}\left[\max(\theta_- - \theta, 0) - \max(\theta - \theta_+, 0)\right]$ and stores $U_{\text{lim}} = \frac{1}{2}K_{\text{lim}}\left[\max(\theta_- - \theta, 0)^2 + \max(\theta - \theta_+, 0)^2\right]$, zero inside the interval and quadratic outside it, so the element is conservative. Dampers store nothing and dissipate $\dot{\mathbf{d}}^T\mathbf{D}_d\dot{\mathbf{d}} \geq 0$. The Supplementary Material derives each of these and gives the remaining variants.

Because the elements are conservative, the whole controller derives from a single scalar potential $U = \sum_i U_i$, so that Eq. (1) reads $\boldsymbol{\tau} = -\partial U/\partial\mathbf{q} - \sum_i \mathbf{J}_{d_i}^T\mathbf{D}_{d_i}\mathbf{J}_{d_i}\dot{\mathbf{q}}$: a gradient plus a dissipative term. Take as storage the total energy of the augmented system, $E = U + U_{\text{hand}} + \frac{1}{2}\dot{\mathbf{q}}^T\mathbf{M}\dot{\mathbf{q}}$, where $U_{\text{hand}} \geq 0$ is the elastic energy stored in the tendons, series springs and skin. Differentiating along the closed-loop trajectories, the kinetic term contributes $\dot{\mathbf{q}}^T\boldsymbol{\tau}$ together with the elastic and external torques, and the two gradient terms cancel exactly against the potentials they derive from, leaving:

$$\dot{E} = \dot{\mathbf{x}}^T\mathbf{f}_{\text{ext}} - \sum_i \dot{\mathbf{d}}_i^T\mathbf{D}_{d_i}\dot{\mathbf{d}}_i - \mathcal{P}_{\text{hand}} \;\leq\; \dot{\mathbf{x}}^T\mathbf{f}_{\text{ext}}, \tag{3}$$

where $\mathcal{P}_{\text{hand}} \geq 0$ is the power dissipated by the physical damping of the hand, principally friction in the tendon routing. Both loss terms are non-negative, so the stored energy can grow only through work done at the external port: the augmented hand is passive with respect to that

port, for any number of elements in any combination of coordinates and with no model of the environment.

Stiffness may also be scheduled during the interaction, and whether Eq. (3) survives depends on what it is scheduled on. If the stiffness depends only on the element's own deflection, the force remains a memoryless function of $\mathbf{e}$, a potential still exists, and passivity is preserved however sharply the stiffness varies. If instead it is scheduled on an exogenous signal, as in the law that stiffens with the measured contact force, no potential exists and passivity is no longer guaranteed. Both families are given explicitly in the Supplementary Material.

Three configurations recur throughout. In the *finger-space* configuration, torsional elements act at MCP, PIP, and DIP, defining a stiffness matrix $\mathbf{K}_d$. In the *task-space* configuration, cartesian elements act at the fingertips, optionally cart-constrained, although they can be placed in other hand positions (see Supplementary Material). The *mixed-space* configuration superimposes both. In all cases the number of elements may exceed the number of actuators, since Eq. (1) maps their forces onto the actuators through $\mathbf{J}_d^T$ rather than solving for them. On the hand, rest positions are usually placed along the first principal component of human grasp postures [44, 49], as the interaction is mainly shaped by the stiffness rather than by position.

Because every virtual element and the hand itself are passive, their interconnection is passive [55, 6]. Therefore, the augmented hand remains stable in contact with any passive environment, which physical objects are [55, 56]. Passivity is thus a property of how the controller is assembled rather than a constraint imposed during synthesis [57, 58]. The parameters here are the stiffnesses, dampings, and rest lengths of a mechanism, and are set directly.

This guarantee holds for elements frozen in time. Every online modulation of $\mathbf{K}_d$ or $\mathbf{d}_{\mathrm{ref}}$ injects energy into the closed loop and suspends it. All modulations reported here were made slow relative to the interaction so that the injected energy remains small. Faster modulation would require explicit energy accounting, for instance through an energy tank that budgets

the work done by varying stiffness [59]. Additional theoretical guarantees are reported in the Supplementary Material.

Contact force and stiffness from virtual work

The virtual elements are known exactly, because they are defined in software rather than identified from hardware. As first approximation, their effect at the point of contact can therefore be estimated from kinematics alone, without measuring force. This prediction is the basis of both the sensing results and the closed-loop control that follows. In the following analysis, we consider only linear springs, although it can be easily extended to nonlinear elements. With no loss of generality, all the generalized VMC coordinates are assumed to be stacked into the vector $\mathbf{d}$.

At quasi-static equilibrium the virtual work performed by the generalized virtual force $\boldsymbol{\tau}_d = \mathbf{K}_d(\mathbf{d}_{\text{ref}} - \mathbf{d})$ equals the work performed at the physical output, represented by a point $\mathbf{x}$ rigidly attached to the hand, such that $\dot{\mathbf{d}}^T \boldsymbol{\tau}_d = \dot{\mathbf{x}}^T \mathbf{f}_x$. Contact restricts which components of the output motion can perform work. Modeling the interaction as a frictionless point contact [53] along a normal $\mathbf{n}$, admissible motion is confined to that direction, and $\dot{\mathbf{x}}$ is replaced by $\mathbf{P}\dot{\mathbf{x}}$ with the rank-one projector $\mathbf{P} = \mathbf{n}\mathbf{n}^T$:

$$\dot{\mathbf{d}}^T \boldsymbol{\tau}_d = \left(\mathbf{P}\dot{\mathbf{x}}\right)^T \mathbf{f}_x. \tag{4}$$

Setting $\mathbf{P} = \mathbf{I}$ recovers the unconstrained generalized force in all directions, so Eq. (4) covers free motion and contact within one expression.

Torques are not transmitted to the joints without loss. Tendon routing and the power stored in the series compliance dissipate part of the commanded torque [48], which we model by a diagonal efficiency matrix $\boldsymbol{\eta}$ in actuator space, with entries in $(0, 1]$ and assumed constant with respect to $\mathbf{q}$. It approximates transmission losses only (friction in the Bowden sheaths, tendon stretch, and energy stored rather than delivered by the series elasticity) and not electrical

losses in the motor, already accounted for by the torque constant, nor actuator stiction, which is compensated a priori by keeping the actuators in a kinetic friction regime. The efficiency matrix is identified from data.

Substituting $\dot{\mathbf{d}} = \mathbf{J}_d\dot{\mathbf{q}}$ and $\dot{\mathbf{x}} = \mathbf{J}_x\dot{\mathbf{q}}$ into Eq. (4), requiring equality for arbitrary $\dot{\mathbf{q}}$, and including the efficiency gives the balance $\boldsymbol{\eta}\,\mathbf{J}_d^T\boldsymbol{\tau}_d = (\mathbf{P}\mathbf{J}_x)^T\mathbf{f}_x$. Solving in the least-squares sense yields the force the fingertip exerts on the environment:

$$\mathbf{f}_x = \left((\mathbf{P}\mathbf{J}_x)^*\right)^T \boldsymbol{\eta}\,\mathbf{J}_d^T\,\mathbf{K}_d\,(\mathbf{d}_{\mathrm{ref}} - \mathbf{d})\,, \tag{5}$$

where $(\cdot)^*$ denotes the Moore–Penrose pseudoinverse. Every quantity on the right is either commanded or read from the actuator encoders, so Eq. (5) is an estimator of contact force requiring no force sensor. Practically, the equation computes the torque transmitted by the actuators $\boldsymbol{\eta}\,\mathbf{J}_d^T\,\mathbf{K}_d\mathbf{e}$ and maps it onto the contact normal $\mathbf{n}$. When $\mathbf{K}_d$ is block-diagonal it decomposes into a sum of independent contributions, one per element, irrespective of the coordinate in which each is defined. Consequently, joint-space and task-space elements acting on the same digit contribute to the tip force by simple summation.

Differentiating the same balance with respect to $\mathbf{q}$ gives the stiffness seen at the output. Retaining only the terms in which the Jacobians are held constant:

$$\mathbf{K}_x \;=\; -\frac{\partial \mathbf{f}_x}{\partial \mathbf{x}} \;=\; \left((\mathbf{P}\mathbf{J}_x)^*\right)^T \boldsymbol{\eta}\,\mathbf{J}_d^T\,\mathbf{K}_d\,\mathbf{J}_d\,(\mathbf{P}\mathbf{J}_x)^*, \tag{6}$$

a congruence transformation that generalizes the classical joint-to-Cartesian stiffness mapping [60] by including the generalized virtual elements and the transmission efficiency. Because $\mathbf{J}_x$ depends on configuration, so does $\mathbf{K}_x$: the same virtual parameters deliver different output stiffness at different poses.

Eq. (6) is a first-order expression. Retaining the terms in which the Jacobians vary with configuration gives:

$$\mathbf{K}_x = \left((\mathbf{P}\mathbf{J}_x)^*\right)^T \left[\,\boldsymbol{\eta}\,\mathbf{J}_d^T\mathbf{K}_d\mathbf{J}_d + \frac{\partial(\mathbf{P}\mathbf{J}_x)^T}{\partial\mathbf{q}}\,\mathbf{f}_x - \frac{\partial(\boldsymbol{\eta}\,\mathbf{J}_d^T)}{\partial\mathbf{q}}\,\boldsymbol{\tau}_d\,\right](\mathbf{P}\mathbf{J}_x)^*, \tag{7}$$

whose two correction terms are the geometric stiffness contributions. Physically, these terms represent the change in the manipulator's effective stiffness due to its kinematic reconfiguration under applied loads and internal virtual torques, captured by introducing the Hessians of the output and virtual-element coordinates. This formulation extends the conservative congruence transformation [61] to include generalized virtual elements and transmission losses. Both Hessians are available analytically, so Eq. (7) could be evaluated at every control cycle to provide a more complete approximation. However, geometric stiffness is negligible compared to the main elastic stiffness unless the system is subjected to exceptionally large forces, so our experiments use the first-order form throughout.

These two expressions connect directly to what is measured in the experiments: $F = \mathbf{n}^T \mathbf{f}_x$ is the component of Eq. (5) along the contact normal, compared against the load cell on the finger test bed or estimated directly on the hand, and $K_n = \mathbf{n}^T \mathbf{K}_x \mathbf{n}$ is the corresponding component of $\mathbf{K}_x$, the stiffness reported at the fingertip.

The model estimate rests on four assumptions: (i) quasi-static equilibrium, so the generalized virtual force reduces to its elastic component; (ii) a frictionless point contact, so only the normal force is transmitted, with the normal $\mathbf{n}$ known, assumed, or sensed; (iii) transmission efficiency $\boldsymbol{\eta}$ constant over the configuration space; and (iv), on the hand, contact normal to the phalanx, the most likely outcome during enveloping grasps.

Identification of the tendon transmission efficiency

The efficiency $\boldsymbol{\eta}$ is the only quantity in Eq. (5) not known a priori, and was identified experimentally on the single-finger test bed. With the arm stationary at the contact pose, the finger repeatedly lifted clear of the load cell, adopted a new virtual torsional stiffness, lowered onto the plate, settled for 3 s and was recorded for 5 s. 200 configurations were collected. Three joint stiffnesses were drawn independently from a uniform distribution over $[0.05, 1.0]$ $\mathrm{N} \cdot \mathrm{m/rad}$,

spanning fingertip forces from 0.4 to 1.5 N. The diagonal entries of $\boldsymbol{\eta}$ were then fitted by least squares so that Eq. (5) best reproduced the measured normal force, giving $\eta_{\mathrm{MCP}} = 0.837$ and $\eta_{\mathrm{PIP}} = 0.359$. The marked asymmetry reflects the longer and more curved routing of the PIP tendon. These two values were reused unchanged on the hand, η_{MCP} being assigned to every MCP-type axis and η_{PIP} to every PIP-type axis of all five digits, while unit efficiency was assumed for the thumb CMC1 and CMC2 axes and for the spread actuator. This extrapolation is the principal approximation in the sensing model, assuming that digits built to the same design and routed the same way lose the same fraction of torque.

Model-based force and stiffness adaptation

Because Eq. (5) is analytic in the virtual parameters, the contact force can be optimized rather than merely tuned. We minimize:

$$\mathcal{L} = \tfrac{1}{2} \left\| \mathbf{f}_x - \mathbf{f}_{x,\mathrm{ref}} \right\|^2 . \tag{8}$$

Solving Eq. (5) directly for $\mathbf{K}_d$ or $\mathbf{d}_{\mathrm{ref}}$ is not viable, and the reason is physical rather than numerical: the equilibrium $\mathbf{d}$ is set by the interaction with the environment, so it moves as the parameters change and the equation to be inverted changes with its own solution. The problem is implicit, and we then descend the gradient of Eq. (8) along one of two independent directions, with step size $\alpha > 0$:

$$\mathbf{K}_d^{(i+1)} = \mathbf{K}_d^{(i)} - \alpha \, \nabla_{\mathbf{K}_d} \mathcal{L}, \qquad \mathbf{d}_{\mathrm{ref}}^{(i+1)} = \mathbf{d}_{\mathrm{ref}}^{(i)} - \alpha \, \nabla_{\mathbf{d}_{\mathrm{ref}}} \mathcal{L}. \tag{9}$$

Adapting the stiffness while holding the rest configuration fixed gives the rank-one update:

$$\mathbf{K}_d^{(i+1)} = \mathbf{K}_d^{(i)} - \alpha \left[\mathbf{J}_d \, \boldsymbol{\eta}^T (\mathbf{P}\mathbf{J}_x)^* \right] \left(\mathbf{f}_x - \mathbf{f}_{x,\mathrm{ref}} \right) \left(\mathbf{d}_{\mathrm{ref}} - \mathbf{d} \right)^T . \tag{10}$$

The bracketed term is the sensitivity carrying the force error from the output back to the coordinates of $\mathbf{K}_d$. The outer product with the current deflection means the update only acts along

directions the element is actually deflected in: an element at rest is untouched, however large the force error. Since $\mathbf{d}_{\mathrm{ref}}$ is unchanged, the pose the hand adopts in the absence of contact is preserved, and the scheme controls force and position jointly. Adapting instead the rest configuration at fixed stiffness gives:

$$\mathbf{d}_{\mathrm{ref}}^{(i+1)} = \mathbf{d}_{\mathrm{ref}}^{(i)} - \alpha\, \mathbf{K}_d^T\, \mathbf{J}_d\, \boldsymbol{\eta}^T (\mathbf{P}\mathbf{J}_x)^*\, (\mathbf{f}_x - \mathbf{f}_{x,\mathrm{ref}})\,, \tag{11}$$

where the same force error and the same sensitivity now appear weighted by $\mathbf{K}_d^T$ rather than by the deflection, so a stiffer element takes a larger step for the same force error, since the sensitivity of force to changes in rest position is itself larger. This update leaves the stiffness free and therefore controls force and stiffness independently. The two schemes reach the same force through different mechanisms: one changes how strongly the finger resists a given deflection, the other changes where it rests. Together they set the slope and operating point of the force-displacement relation separately.

The update of Eq. (10) does not in general preserve the symmetry of $\mathbf{K}_d$. Symmetrizing at each step would be straightforward, at the cost of departing from the gradient direction, but it turns out not to be strictly necessary: as shown in the Supplementary Material, under sufficient damping the resulting asymmetric element still dissipates energy.

Each scheme was compared against a model-free baseline that updates the same parameter proportionally to the force error, without evaluating the local sensitivity of the model, using an identical step size so that the comparison isolates the contribution of the model rather than of the gain. Step sizes were $\alpha = 10^{-4}$ for Eq. (10) and 5×10^{-4} for Eq. (11) on the finger, and 10^{-5} on the hand. Admissible step sizes, and the conditions preserving positive definiteness of $\mathbf{K}_d$ under Eq. (10), are derived in the Supplementary Material.

When a stiffness profile rather than a force is prescribed, the virtual parameters follow from inverting Eq. (6). Writing it as $\mathbf{K}_x = \mathbf{L}\mathbf{K}_d\mathbf{R}$, with $\mathbf{L} = ((\mathbf{P}\mathbf{J}_x)^*)^T \boldsymbol{\eta}\, \mathbf{J}_d^T$ mapping a virtual

torque to the output force and $\mathbf{R} = \mathbf{J}_d(\mathbf{P}\mathbf{J}_x)^*$ mapping an output deflection to the virtual coordinates, $\mathbf{K}_d$ is sandwiched between the two maps rather than isolated as a vector multiplied by a single matrix, so the relation cannot yet be inverted with a pseudoinverse. Denoting by $\mathrm{vec}(\cdot)$ the column-wise stacking of a matrix into a vector and by $\otimes$ the Kronecker product, the identity $\mathrm{vec}(\mathbf{AXB}) = (\mathbf{B}^T \otimes \mathbf{A})\,\mathrm{vec}(\mathbf{X})$ rewrites it as an explicit linear system in $\mathrm{vec}(\mathbf{K}_d)$, with $\mathbf{L}$ and $\mathbf{R}$ combined into the single matrix $\mathbf{R}^T \otimes \mathbf{L}$:

$$\mathrm{vec}\big(\mathbf{K}_d^{\mathrm{ff}}\big) = \big(\mathbf{R}^T \otimes \mathbf{L}\big)^* \,\mathrm{vec}(\mathbf{K}_{x,\mathrm{des}})\,, \tag{12}$$

returning the minimum-norm virtual stiffness that reproduces the desired output stiffness, exactly when the target is achievable and in the least-squares sense otherwise. It generalizes to several element groups acting on one fingertip by stacking their maps horizontally before inversion (Supplementary Material).

Kinematic model and tendon transmission

The finger is modeled as a planar chain of three revolute joints rotating about a common axis, with proximal, middle, and distal phalanx lengths ℓ_p, ℓ_m and ℓ_d. Each actuator drives its joint through a linear transmission,

$$\theta_{\mathrm{MCP}} = \frac{r_p}{r_m}\, q_{\mathrm{MCP}}, \qquad \theta_{\mathrm{PIP}} = \frac{r_m}{c}\, q_{\mathrm{PIP}}, \qquad \theta_{\mathrm{DIP}} = \theta_{\mathrm{PIP}}, \tag{13}$$

where r_m is the actuator pulley radius, r_p the finger MCP pulley radius and c a cable-driven transmission constant. Their values for the test bed and for every digit of the hand, together with phalanx lengths, the wrist reductions and the spread coupling ratios, are listed in the Supplementary Material. The Supplementary Material verifies the linearity assumed in Eq. (13) experimentally, for every joint of both platforms.

Joint origins and axes for the hand were taken from its URDF description, together with link masses and centers of mass. Forward kinematics, Jacobians and Hessians were derived

symbolically and compiled to numerical functions, so that every geometric quantity entering the controller and the stiffness model, including the second-order terms, is available analytically at each control cycle rather than estimated by finite differences.

Compensation of gravity, friction, and joint limits

Three torque contributions are computed alongside the virtual model and added to it before the command reaches the actuators. Gravity is compensated link by link as $\boldsymbol{\tau}_g = \sum_\ell \mathbf{J}_{\mathrm{cog},\ell}^T \mathbf{F}_{g,\ell}$, using the robot masses and centers of mass. On the hand, the wrist orientation is read from the UR5 so that compensation remains valid as the arm reorients the palm. Assuming this compensation exact, the gravitational potential cancels from the closed loop, which is why it does not appear in E in Eq. (3). Joint limits are enforced by deadzone springs producing no torque inside the admissible range and a linear restoring torque outside it.

Actuator stiction is compensated by a Stribeck term,

$$\boldsymbol{\tau}_f = F_{\max}\, \exp\!\big(-\,(\dot{\mathbf{q}}/v_{\lim})^2\big) \odot \operatorname{sign}(\boldsymbol{\tau}_{\mathrm{cmd}})\,, \tag{14}$$

with $v_{\lim} = 0.03$ rad/s on both platforms and $F_{\max}$ between 0.01 and 0.20 N $\cdot$ m, tuned per experiment (Supplementary Table 2), and $\odot$ denoting the element-wise product. The envelope is largest at low velocity, so the compensation pushes the actuator into motion and switches itself off, producing a continuous low-amplitude oscillation. This addition keeps the actuators in a kinetic rather than a static friction regime [41] and thereby removes the dead band that otherwise masks small virtual forces, a mechanism also proposed as a function of physiological tremor [42]. Its cost is a persistent ripple in the measured force, which is why force tracking signals are reported both raw and smoothed.

Experimental protocols

Single-finger experiments followed a common sequence. The arm was brought to the contact pose with the finger lifted clear of the plate; after 3 s the experimental condition was applied and the joint references set to 30°. After a further 3 s the arm descended 20 mm (or 10 when comparing initial poses) at 2 mm$/$s and returned at the same speed, with force and actuator state recorded throughout. Passive characterization swept the virtual stiffness in the finger-space and then in the cart-constrained task-space configuration; pose dependence was assessed by displacing the initial arm height, and directional dependence by rotating the cart axis ϕ. Online modulation used the stiffness laws of the Supplementary Material and a Gaussian repulsive fingertip spring active over the middle half of the stroke. Force tracking followed a square reference over three cycles; an open-loop variant tracked a rising staircase driven by the force predicted from Eq. (5), with the load cell logged but excluded from the loop.

On the hand, the guitar task held index, middle, and ring closed at fixed flexion while the arm performed a single upward strum, one per stiffness condition so that each yields an independent audio recording. The weight bearing task held the index in a hook posture while an operator added three 100 g loads in succession. In-hand manipulation closed the hand onto a printed TPU cylinder and redistributed fingertip stiffness towards the radial and then the ulnar digits, the thumb being softened throughout. Dynamic grasping triggered closure during a constant-speed arm translation, under a soft, a stiff, and an adaptive schedule. Compliance sensing probed each object at low thumb stiffness and then swept the thumb stiffness upwards while the opposing digits were held fixed. The apple task closed the hand at fixed stiffness, adapted it by Eq. (10) towards three force targets, and then descended 0.15 m against an elastic band. Stiffnesses, sweep ranges, step sizes, ramp durations, and repetition counts are given per figure panel in the Supplementary Material.

Data analysis and statistics

Unless stated otherwise, each finger experiment was repeated $N = 5$ times and results are reported as the mean with shaded bands spanning $\pm$ 1 standard deviation. On the hand, only compliance sensing was repeated five times; the remaining tasks are reported from a single trial per condition, as they demonstrate a qualitative behavior rather than estimate a quantity. Measured forces retain the ripple introduced by friction compensation, and are therefore shown raw and, where a trend is compared against a reference, also smoothed with a Savitzky-Golay filter of window 21 samples and polynomial order 3, denoted $\tilde{F}$. Tracking accuracy is the RMSE between $\tilde{F}$ and the reference over the tracking window; responsiveness is the transition time, the interval taken by $\tilde{F}$ to move between 10% and 90% of a step amplitude, averaged over rising and falling transitions. Effective stiffness is obtained by linear regression of force against imposed displacement d over the descent window, reported as $\Delta F/\Delta d$. Audio was extracted from the video recordings to 16-bit PCM and normalized to a single global peak across the three strumming conditions, so that the reported RMS intensities are comparable.

Data availability

The data generated in this study are available at
`https://github.com/CREATE-Lab-EPFL/HumanManipulationVMC`.

Code availability

The code supporting the findings of this study is available at
`https://github.com/CREATE-Lab-EPFL/HumanManipulationVMC`.

References

[1] Burdet, E., Osu, R., Franklin, D. W., Milner, T. E. & Kawato, M. The Central Nervous System Stabilizes Unstable Dynamics by Learning Optimal Impedance. *Nature* **414**, 446–449 (2001).

[2] Milner, T. E. & Cloutier, C. Compensation for Mechanically Unstable Loading in Voluntary Wrist Movement. *Experimental Brain Research* **94** (1993).

[3] Billard, A. & Kragic, D. Trends and Challenges in Robot Manipulation. *Science* **364**, eaat8414 (2019).

[4] Sobinov, A. R. & Bensmaia, S. J. The Neural Mechanisms of Manual Dexterity. *Nature Reviews Neuroscience* **22**, 741–757 (2021).

[5] Kuo, P.-H. & Deshpande, A. D. Muscle-Tendon Units Provide Limited Contributions to the Passive Stiffness of the Index Finger Metacarpophalangeal Joint. *Journal of Biomechanics* **45**, 2531–2538 (2012).

[6] Hogan, N. On the Stability of Manipulators Performing Contact Tasks. *IEEE Journal on Robotics and Automation* **4**, 677–686 (1988).

[7] Tee, K. P., Franklin, D. W., Kawato, M., Milner, T. E. & Burdet, E. Concurrent Adaptation of Force and Impedance in the Redundant Muscle System. *Biological Cybernetics* **102**, 31–44 (2010).

[8] Höppner, H., Große-Dunker, M., Stillfried, G., Bayer, J. & Van Der Smagt, P. Key Insights into Hand Biomechanics: Human Grip Stiffness Can Be Decoupled from Force by Cocontraction and Predicted from Electromyography. *Frontiers in Neurorobotics* **11**, 17 (2017).

[9] Piazza, C., Grioli, G., Catalano, M. G. & Bicchi, A. A Century of Robotic Hands. *Annual Review of Control, Robotics, and Autonomous Systems* **2**, 1–32 (2019).

[10] Gilday, K., Sirithunge, C., Iida, F. & Hughes, J. Embodied Manipulation with Past and Future Morphologies through an Open Parametric Hand Design. *Science Robotics* (2025).

[11] Gilday, K., Pyeon, D., Dhanush, S., Cho, K. & Hughes, J. Exploiting Passive Behaviours for Diverse Musical Playing Using the Parametric Hand. *Frontiers in Robotics and AI* **11**, 1463744 (2024).

[12] Hughes, J. A. E., Maiolino, P. & Iida, F. An Anthropomorphic Soft Skeleton Hand Exploiting Conditional Models for Piano Playing. *Science Robotics* **3**, eaau3098 (2018).

[13] Yang, Y., Li, Y. & Chen, Y. Principles and Methods for Stiffness Modulation in Soft Robot Design and Development. *Bio-Design and Manufacturing* **1**, 14–25 (2018).

[14] Wolf, S., Grioli, G., Eiberger, O., Friedl, W., Grebenstein, M., Hoppner, H. et al. Variable Stiffness Actuators: Review on Design and Components. *IEEE/ASME Transactions on Mechatronics* **21**, 2418–2430 (2016).

[15] Yan, J., Xu, Z., Shi, P. & Zhao, J. A Human-Inspired Soft Finger with Dual-Mode Morphing Enabled by Variable Stiffness Mechanism. *Soft Robotics* **9**, 399–411 (2022).

[16] Yang, Y., Chen, Y., Li, Y., Wang, Z. & Li, Y. Novel Variable-Stiffness Robotic Fingers with Built-In Position Feedback. *Soft Robotics* **4**, 338–352 (2017).

[17] Junge, K., Noda, T. & Hughes, J. Mod-VSA: A Modular Variable Stiffness Actuator for Multi-fingered Robotic Hands. *2025 IEEE 8th International Conference on Soft Robotics (RoboSoft)* 1–6 (IEEE, 2025).

[18] Kamadan, A., Kiziltas, G. & Patoglu, V. Co-Design Strategies for Optimal Variable Stiffness Actuation. *IEEE/ASME Transactions on Mechatronics* **22**, 2768–2779 (2017).

[19] Abu-Dakka, F. J. & Saveriano, M. Variable Impedance Control and Learning–A Review. *Frontiers in Robotics and AI* **7**, 590681 (2020).

[20] Song, P., Yu, Y. & Zhang, X. Impedance Control of Robots: An Overview. *2017 2nd International Conference on Cybernetics, Robotics and Control (CRC)* 51–55 (IEEE, 2017).

[21] Albu-Schaffer, A. & Hirzinger, G. Cartesian Impedance Control Techniques for Torque Controlled Light-Weight Robots. *Proceedings 2002 IEEE International Conference on Robotics and Automation* 657–663 (IEEE, 2002).

[22] Hogan, N. Impedance Control: An Approach to Manipulation. *1984 American Control Conference* 304–313 (IEEE, 1984).

[23] Albu-Schäffer, A., Ott, C. & Hirzinger, G. A Unified Passivity-based Control Framework for Position, Torque and Impedance Control of Flexible Joint Robots. *The International Journal of Robotics Research* **26**, 23–39 (2007).

[24] Ott, C., Albu-Schaffer, A., Kugi, A. & Hirzinger, G. On the Passivity-Based Impedance Control of Flexible Joint Robots. *IEEE Transactions on Robotics* **24**, 416–429 (2008).

[25] Yang, C., Ganesh, G., Haddadin, S., Parusel, S., Albu-Schaeffer, A. & Burdet, E. Human-Like Adaptation of Force and Impedance in Stable and Unstable Interactions. *IEEE Transactions on Robotics* **27**, 918–930 (2011).

[26] Petit, F. & Albu-Schaffer, A. Cartesian Impedance Control for a Variable Stiffness Robot Arm. *2011 IEEE/RSJ International Conference on Intelligent Robots and Systems* 4180–4186 (IEEE, 2011).

[27] Biagiotti, L., Liu, H., Hirzinger, G. & Melchiorri, C. Cartesian Impedance Control for Dexterous Manipulation. *Proceedings 2003 IEEE/RSJ International Conference on Intelligent Robots and Systems* 3270–3275 (IEEE, 2003).

[28] Pfanne, M., Chalon, M., Stulp, F., Ritter, H. & Albu-Schaffer, A. Object-Level Impedance Control for Dexterous In-Hand Manipulation. *IEEE Robotics and Automation Letters* **5**, 2987–2994 (2020).

[29] Song, P., Yu, Y. & Zhang, X. A Tutorial Survey and Comparison of Impedance Control on Robotic Manipulation. *Robotica* **37**, 801–836 (2019).

[30] Bicchi, A. & Kumar, V. Robotic Grasping and Contact: A Review. *Proceedings 2000 ICRA. Millennium Conference. IEEE International Conference on Robotics and Automation. Symposia Proceedings* 348–353 (IEEE, 2000).

[31] Al-Shuka, H. F. N., Leonhardt, S., Zhu, W., Song, R., Ding, C. & Li, Y. Active Impedance Control of Bioinspired Motion Robotic Manipulators: An Overview. *Applied Bionics and Biomechanics* **2018**, 1–19 (2018).

[32] Kronander, K. & Billard, A. Stability Considerations for Variable Impedance Control. *IEEE Transactions on Robotics* **32**, 1298–1305 (2016).

[33] Junge, K. & Hughes, J. Spatially Distributed Biomimetic Compliance Enables Robust Anthropomorphic Robotic Manipulation. *Communications Engineering* **4**, 76 (2025).

[34] Pratt, J., Chew, C., Torres, A., Dilworth, P. & Pratt, G. Virtual Model Control: An Intuitive Approach for Bipedal Locomotion. *The International Journal of Robotics Research* **20**, 129–143 (2001).

[35] Zhang, Y., Larby, D., Iida, F. & Forni, F. Virtual Model Control for Compliant Reaching under Uncertainties. *2024 IEEE/RSJ International Conference on Intelligent Robots and Systems (IROS)* 795–801 (IEEE, 2024).

[36] Siciliano, B. & Khatib, O. *Springer Handbook of Robotics* (Springer International Publishing, 2016).

[37] Larby, D. & Forni, F. Optimal Virtual Model Control for Robotics: Design and Tuning of Passivity-Based Controllers. *IEEE Transactions on Robotics* **42**, 439–454 (2026).

[38] Faris, O., Tadeja, S. K. & Forni, F. A Virtual Mechanical Interaction Layer Enables Resilient Human-to-Robot Object Handovers. *IEEE Robotics and Automation Letters* **11**, 7780–7787 (2026).

[39] Junge, K. & Hughes, J. ADAPT-Teleop: Robotic Hand with Human Matched Embodiment Enables Dexterous Teleoperated Manipulation. *npj Robotics* **3**, 31 (2025).

[40] Zhang, Y., Wang, H. & Hughes, J. Modular Anthropomorphic Hand Design via Multi-Parameter Finger Benchmarking and Selection. Preprint at https://arxiv.org/abs/2606.11826 (2026).

[41] Márton, L. & Lantos, B. Control of Mechanical Systems with Stribeck Friction and Backlash. *Systems & Control Letters* **58**, 141–147 (2009).

[42] Goodman, D. & Kelso, J. A. S. Exploring the Functional Significance of Physiological Tremor: A Biospectroscopic Approach. *Experimental Brain Research* **49**, 419–431 (1983).

[43] Chen, G., Guo, S., Hou, B. & Wang, J. Virtual Model Control for Quadruped Robots. *IEEE Access* **8**, 140736–140751 (2020).

[44] Santello, M., Flanders, M. & Soechting, J. F. Postural Hand Synergies for Tool Use. *Journal of Neuroscience* **18**, 10105–10115 (1998).

[45] Morgan, A. S., Hang, K., Wen, B., Bekris, K. & Dollar, A. M. Complex In-Hand Manipulation Via Compliance-Enabled Finger Gaiting and Multi-Modal Planning. *IEEE Robot. Autom. Lett.* **7**, 4821–4828 (2022).

[46] Wahrburg, A., Bos, J., Listmann, K. D., Dai, F., Matthias, B. & Ding, H. Motor-Current-Based Estimation of Cartesian Contact Forces and Torques for Robotic Manipulators and Its Application to Force Control. *IEEE Transactions on Automation Science and Engineering* **15**, 879–886 (2018).

[47] Van Damme, M., Beyl, P., Vanderborght, B., Grosu, V., Van Ham, R., Vanderniepen, I. et al. Estimating Robot End-Effector Force from Noisy Actuator Torque Measurements. *2011 IEEE International Conference on Robotics and Automation* 1108–1113 (IEEE, 2011).

[48] Wagner, C. R. & Emmanouil, E. Efficiency and Power Limits of Electrical and Tendon-Sheath Transmissions for Surgical Robotics. *Frontiers in Robotics and AI* **5**, 50 (2018).

[49] Wimbock, T., Jahn, B. & Hirzinger, G. Synergy Level Impedance Control for Multifingered Hands. *2011 IEEE/RSJ International Conference on Intelligent Robots and Systems* 973–979 (IEEE, 2011).

[50] Zaidi, L., Corrales, J. A., Bouzgarrou, B. C., Mezouar, Y. & Sabourin, L. Model-Based Strategy for Grasping 3D Deformable Objects Using a Multi-Fingered Robotic Hand. *Robotics and Autonomous Systems* **95**, 196–206 (2017).

[51] Zeng, G. & Hemami, A. An Overview of Robot Force Control. *Robotica* **15**, 473–482 (1997).

[52] Dietrich, A., Wu, X., Bussmann, K., Ott, C., Albu-Schäffer, A. & Stramigioli, S. Passive Hierarchical Impedance Control Via Energy Tanks. *IEEE Robotics and Automation Letters* **2**, 522–529 (2017).

[53] Murray, R. M., Li, Z. & Sastry, S. S. *A Mathematical Introduction to Robotic Manipulation* (CRC Press, 2017).

[54] Petit, F. & Albu-Schaffer, A. State Feedback Damping Control for a Multi DOF Variable Stiffness Robot Arm. *2011 IEEE International Conference on Robotics and Automation (ICRA)* 5561–5567 (IEEE, 2011).

[55] Willems, J. C. Dissipative Dynamical Systems. *European Journal of Control* **13**, 134–151 (2007).

[56] Larby, D. & Forni, F. A Generalized Approach to Impedance Control Design for Robotic Minimally Invasive Surgery. *IFAC-PapersOnLine* **56**, 8548–8555 (2023).

[57] Hatanaka, T., Chopra, N. & Spong, M. W. Passivity-Based Control of Robots: Historical Perspective and Contemporary Issues. *2015 54th IEEE Conference on Decision and Control (CDC)* 2450–2452 (IEEE, 2015).

[58] Larby, D. & Forni, F. A Passivity Preserving H-infinity Synthesis Technique for Robot Control. *2022 IEEE 61st Conference on Decision and Control (CDC)* 1416–1422 (IEEE, 2022).

[59] Ferraguti, F., Secchi, C. & Fantuzzi, C. A Tank-Based Approach to Impedance Control with Variable Stiffness. *2013 IEEE International Conference on Robotics and Automation* 4948–4953 (IEEE, 2013).

[60] Salisbury, J. Active Stiffness Control of a Manipulator in Cartesian Coordinates. *1980 19th IEEE Conference on Decision and Control* 95–100 (IEEE, 1980).

[61] Chen, S. & Kao, I. Conservative Congruence Transformation for Joint and Cartesian Stiffness Matrices of Robotic Hands and Fingers. *The International Journal of Robotics Research* **19**, 835–847 (2000).

Acknowledgements

We thank the Control Robotics Lab at the University of Cambridge for hosting L.V. and for the discussions on passivity theory, and the Sycamore Lab at EPFL for the use of their space and camera equipment. This work was supported by the Swiss National Science Foundation (SNSF) through the Starting Grant no. 503062, Mechanisms, Modeling and Control for Musculoskeletal Morphing Robots.

Author contributions

Conceptualization: L.V., F.F. and J.H. **Methodology**: L.V., F.F. and J.H. **Resources**: L.V. and Y.Z. **Investigation**: L.V. **Data analysis**: L.V. **Visualization**: L.V. and J.H. **Supervision**: F.F. and J.H. **Writing, original draft**: L.V. **Writing, review and editing**: all authors.

Competing interests

The authors declare that they have no competing interests.

Supplementary Material

We provide additional data and specifications that we use to support the statements in the main text. The Supplementary Material is organized as follows:

- **A: System characterization**
- **B: VMC control, theoretical formulation for the apparatus**
- **C: Full force and stiffness theorem, CCT correction, and optimization for online tuning**
- **D: Description of additional experiments**
- **E: Description of videos**
- **F: Description of further results**

A: System characterization

This section reports the experimental characterization of the two platforms:

1. **Finger kinematics**
2. **Hand kinematics**
3. **Friction compensation validation**
4. **Identified parameters**

A.1: Finger kinematics

The virtual model controller maps forces onto the actuators through the transmission Jacobian $\mathbf{J}_{\boldsymbol{\theta}} = \partial\boldsymbol{\theta}/\partial\mathbf{q}$, where $\mathbf{q}$ collects the actuator angles and $\boldsymbol{\theta}$ the joint angles. This mapping presupposes that the actuator-to-joint relation is linear, that is:

$$\theta_{\mathrm{MCP}} = \frac{r_p}{r_m}\, q_{\mathrm{MCP}}, \qquad \theta_{\mathrm{PIP}} = \frac{r_m}{c}\, q_{\mathrm{PIP}}, \qquad \theta_{\mathrm{DIP}} = \theta_{\mathrm{PIP}}, \tag{S1}$$

with r_m the actuator pulley radius, r_p the finger MCP pulley radius, and c a cable-driven transmission constant. We verified this assumption directly on every joint of both platforms.

Joint angles were measured with a goniometer while each actuator was driven through its admissible range, and a linear model was fitted to the resulting pairs. Fig. S1 reports the single-finger test bed in terms of both actuation routing and joint calibration. The DIP joint is not calibrated independently, being mechanically constrained to follow the PIP.

A.2: Hand kinematics

The same procedure was applied to every digit of the ADAPT Hand. Fig. S2 reports the thumb, whose four joints (CMC1, CMC2, MCP, IP) are driven by a dedicated actuator, and Fig. S3 the MCP and PIP joints of the index, middle, ring, and pinky. As on the test bed, the DIP follows

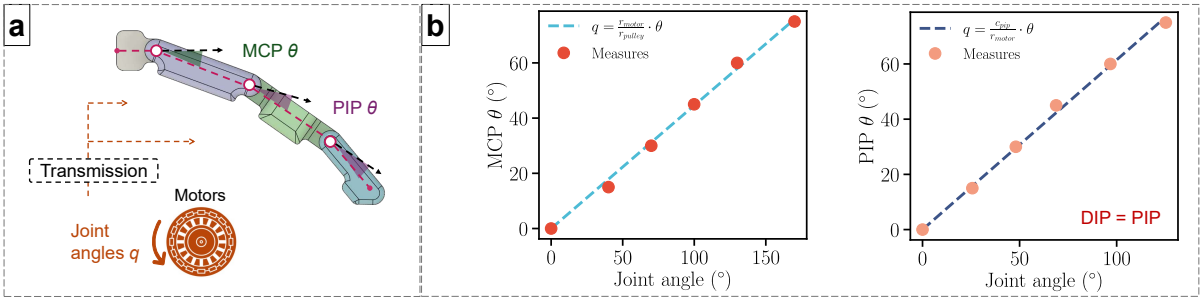


Figure S1: **Kinematic transmission calibration of the finger test bed**. **a** Schematic of the motor-to-joint transmission, relating motor rotation to the MCP and PIP joint angles. **b** Calibration of the MCP (left) and PIP (right) joint angles against motor angles, with linear fits to the measured points; the DIP joint is mechanically coupled to PIP.

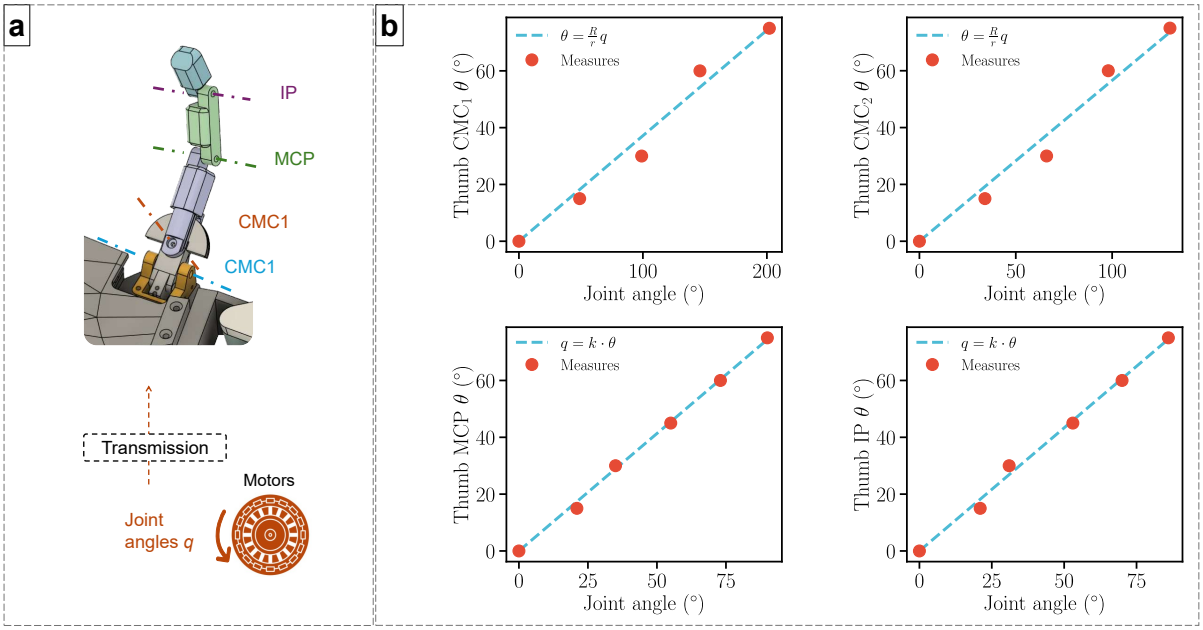


Figure S2: **Kinematic transmission calibration of the thumb**. **a** Thumb kinematic diagram, with the CMC1, CMC2, MCP, and IP joints and their motor transmission. **b** Calibration of the CMC1, CMC2, MCP, and IP joint angles against motor angle, with linear fits to the measured points.

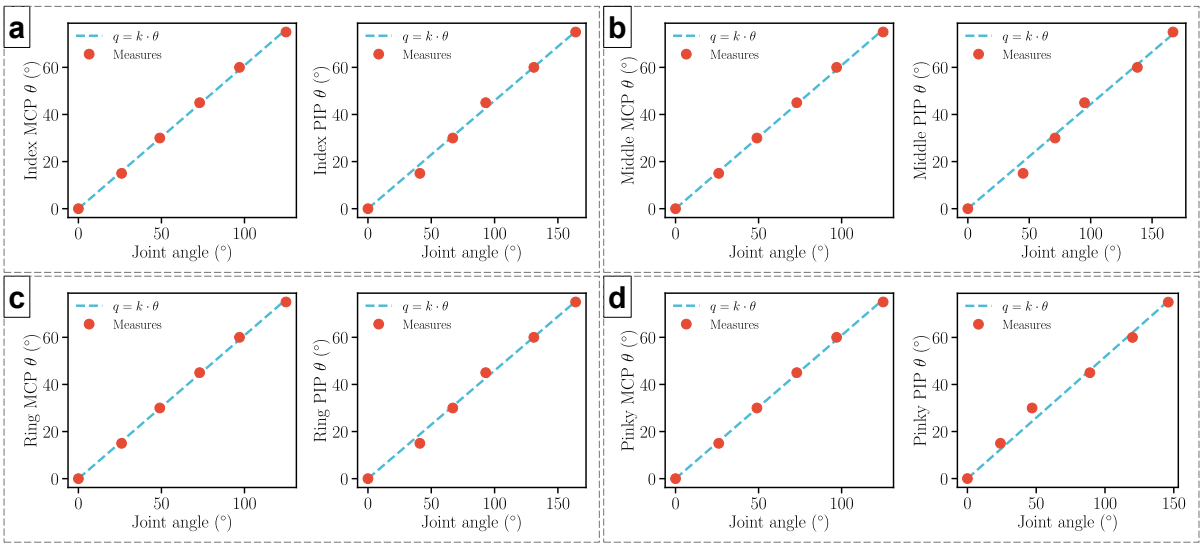


Figure S3: **Kinematic transmission calibration of the index, middle, ring, and pinky fingers**. **a** Index MCP and PIP calibration. **b** Middle MCP and PIP calibration. **c** Ring MCP and PIP calibration. **d** Pinky MCP and PIP calibration.

the PIP through a mimic coupling and is not calibrated separately. The fitted slopes give the transmission constants of Table S3. Differences between the constants of the hand and of the finger reflect their different transmission designs.

A.3: Finger friction compensation validation

Actuator stiction is compensated by a Stribeck term whose envelope is largest at low velocity:

$$\boldsymbol{\tau}_f = F_{\max}\, \exp\!\left(-\left(\dot{\mathbf{q}}/v_{\lim}\right)^2\right) \odot \operatorname{sign}(\boldsymbol{\tau}_{\mathrm{cmd}})\,, \tag{S2}$$

with $\odot$ the element-wise product. Since the envelope decays with velocity, the compensation pushes the actuator into motion and switches itself off, producing a continuous low-amplitude oscillation. To validate it (Fig. S4**a**), the finger was controlled in free space with torsional virtual springs, tracking a step and a ramp reference with and without the Stribeck term. Without compensation both joints exhibit a dead band: small commanded torques produce no motion until the stiction is exceeded, leaving a steady-state offset between the commanded and the

Table S1: **Notation: kinematics and virtual elements**. Bold lowercase denotes vectors, bold uppercase matrices.

Symbol	Meaning	Unit
Coordinates and kinematics		
$\mathbf{q}$	Actuator (motor) angles	rad
$\boldsymbol{\theta}$	Joint angles (MCP, PIP, DIP)	rad
$\mathbf{x}$	Position of the output point, typically the fingertip	m
$\mathbf{d}$	Generalized coordinate hosting a virtual element	varies
$\mathbf{J}_{\boldsymbol{\theta}}$	Transmission Jacobian, $\partial\boldsymbol{\theta}/\partial\mathbf{q}$	—
$\mathbf{J}_x$	Output Jacobian, $\partial\mathbf{x}/\partial\mathbf{q}$	m/rad
$\mathbf{J}_d$	Virtual-element Jacobian, $\partial\mathbf{d}/\partial\mathbf{q}$	varies
ℓ_p, ℓ_m, ℓ_d	Proximal, middle, distal phalanx lengths	m
$r_m,\ r_p$	Actuator and finger MCP pulley radii	m
c	Cable-driven transmission constant	m
Virtual elements		
$\mathbf{K}_d,\ \mathbf{D}_d$	Virtual stiffness and damping on $\mathbf{d}$	varies
$\mathbf{d}_{\text{ref}}, \mathbf{e}$	Virtual rest configuration; deflection $\mathbf{d}_{\text{ref}} - \mathbf{d}$	varies
$\boldsymbol{\tau}_d$	Generalized virtual force, $\mathbf{K}_d\mathbf{e}$	varies
U	Storage function (potential) of an element	J
K_θ	Shared scalar torsional stiffness, finger-space configuration	N·m/rad
K_c	Cart-constrained fingertip stiffness, test bed	N/m
K_t	Fingertip cartesian stiffness, hand	N/m
K_{sensing}	Thumb stiffness during compliance probing	N/m
$A,\ \sigma,\ \Delta\mathbf{z}$	Gaussian strength, width, offset from the repulsion center	N/m, m, m
α	Rate of a stiffness law; *also* the gradient-descent step size	varies
p	Order of the polynomial stiffness law	—
ϕ	Cart direction angle in the sagittal plane	deg

Table S2: **Notation: contact, adaptation, and analysis**. Bold lowercase denotes vectors, bold uppercase matrices.

Symbol	Meaning	Unit
Contact, force, and stiffness		
$\mathbf{n}$	Contact normal (unit); *distinct* from the sample count N	—
$\mathbf{P} = \mathbf{n}\mathbf{n}^T$	Contact projection, acting on the *output*	—
$\mathbf{P}_c = \mathbf{n}_c\mathbf{n}_c^T$	Cart projection, acting on the *virtual element*	—
$\boldsymbol{\eta}$	Diagonal transmission efficiency, $\eta_i \in (0, 1]$	—
$\mathbf{f}_x$, $F = \mathbf{n}^T\mathbf{f}_x$	Contact force at the output; its normal component	N
$\mathbf{K}_x$, $K_n = \mathbf{n}^T\mathbf{K}_x\mathbf{n}$	Output stiffness; its normal component	N/m
$(\cdot)^*$	Moore–Penrose pseudoinverse	—
Adaptation, stability, and analysis		
$\mathcal{L}$	Force-tracking loss, $\frac{1}{2}\|\mathbf{f}_x - \mathbf{f}_{x,\mathrm{ref}}\|^2$	N^2
$\mathbf{L}$, $\mathbf{R}$	Congruence maps in $\mathbf{K}_x = \mathbf{L}\mathbf{K}_d\mathbf{R}$	varies
$\mathbf{S}$	Sensitivity of the force to the rest configuration	varies
e_i, $\mathbf{e}_i$	Scalar and vector force error at iteration i	N
γ_i, λ_i, β_i	Step-size bounds in Lemma 1 and Proposition 3	varies
ς	$\|\mathbf{K}_{\mathrm{skew}}\|_2$, asymmetry of $\mathbf{K}_d$	varies
d	Imposed arm displacement; *distinct* from the vector $\mathbf{d}$	m
$\Delta F/\Delta d$	Effective stiffness, by regression over the descent window	N/m
$\tilde{F}$	Smoothed normal force (Savitzky–Golay, window 21, order 3)	N
N	Number of independent repetitions per condition	—

Table S3: **Identified and measured parameters**. Values used by the controller and by the stiffness model on both platforms.

Parameter	**Value**	**Unit**
Link geometry (both platforms)		
Phalanx lengths $\ell_p,\ \ell_m,\ \ell_d$	40.0, 30.0, 17.5	mm
Fingertip offset along the distal axis	17.5	mm
Transmission, single-finger test bed		
Actuator pulley r_m	5.00	mm
Finger MCP pulley r_p	2.23	mm
PIP transmission constant c	8.13	mm
Transmission, ADAPT Hand		
Actuator pulley r_m, all digits	5.00	mm
Finger MCP pulley r_p, four fingers	3.04	mm
c: index / middle / ring / pinky	10.90 / 11.27 / 10.90 / 9.67	mm
Thumb CMC1 / CMC2 pulley radii	13.46 / 8.83	mm
Thumb MCP / IP transmission constants	6.05 / 5.77	mm
Wrist spur / bevel reduction	0.800 / 0.857	—
Spread ratios: index / middle / ring / pinky	1.0 / 0 / -1.0 / -1.5	—
Transmission efficiency (identified)		
η_{MCP}, all MCP-type axes	0.837	—
η_{PIP}, all PIP-type axes	0.359	—
η, thumb CMC1, CMC2, and spread	1.0 (assumed)	—
Friction compensation		
Stribeck velocity v_{lim}, both platforms	0.03	rad/s
$F_{\max}$, single-finger test bed	0.20	N·m
$F_{\max}$, hand: guitar / weight bearing	0.02 / 0.01	N·m
$F_{\max}$, hand: in-hand and dynamic grasp	0.06	N·m
$F_{\max}$, hand: compliance sensing / apple	0.04 / 0.05	N·m
Limits and control		
Deadzone limit stiffness, finger / hand	1.0 / 0.6	N·m/rad
Commanded torque saturation	0.8	N·m
Joint range, MCP	$[0,\ \pi/2]$	rad
Joint range, PIP and DIP	$[0,\ 1.22]$	rad
Control rate, finger / hand	900 / 330	Hz
Torque-controlled actuators, finger / hand	2 / 13	—

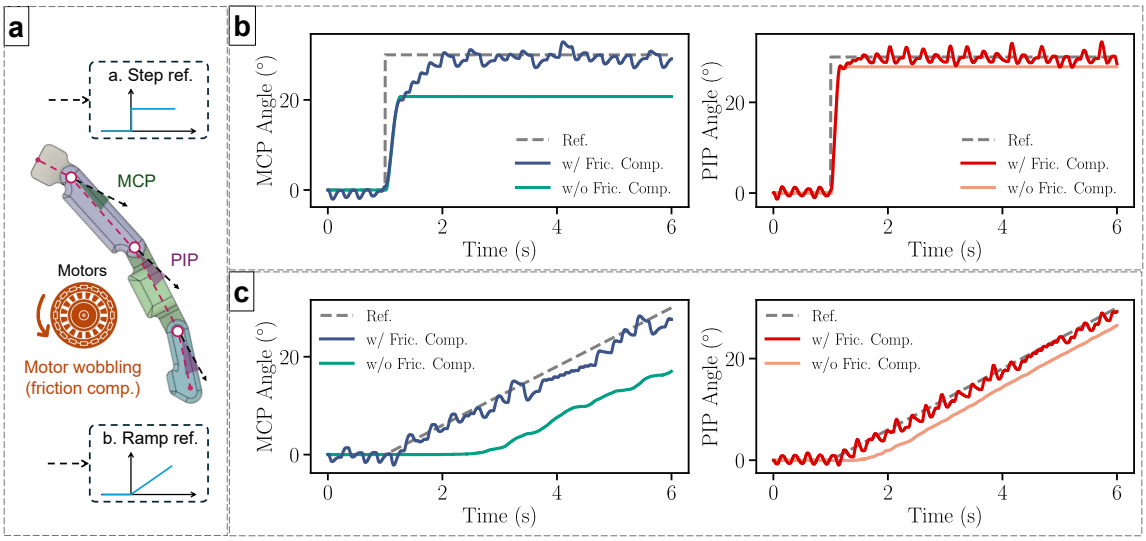


Figure S4: **Validation of friction compensation via continuous motor wobbling**. **a** Friction-compensation scheme: continuous motor wobbling superimposed on the reference command, tested against a step and a ramp reference. **b** Step response of the MCP and PIP joints, with and without friction compensation. **c** Ramp response of the MCP and PIP joints, with and without friction compensation.

reached joint angle (Fig. S4**b**), and under a ramp reference the same effect appears as stick–slip (Fig. S4**c**). With compensation the dead band is removed and tracking becomes continuous at both joints, the MCP benefiting more, at the cost of a persistent ripple at the joint and, consequently, in the measured contact force. The trade is favorable here because the forces of interest are small: a dead band of the order of the stiction torque would suppress precisely the low-force regime in which the compliance modulation operates. The ripple can be removed at analysis time by the smoothing described in the Methods.

A.4: Identified parameters

Table S1 and Table S2 list the notation used throughout the main text and this document. Table S3 collects every identified and measured parameter. All values are those used by the controller and by the stiffness model, and corresponds to the constants defined in the code repository.

B: VMC control, theoretical formulation for the apparatus

This section gives the complete element library, with the force and the stored energy of each element, and then the concrete virtual-element configurations used on the two platforms.

B.1: Element library and storage functions

Let $\mathbf{e} = \mathbf{d}_{\mathrm{ref}} - \mathbf{d}$ denote the deflection of an element and $\dot{\mathbf{d}}$ its rate. Each spring is specified by the force it returns: the actuator torque follows by mapping that force through $\mathbf{J}_d^T$ and summing over elements. Every spring below is conservative, and we give its storage function U explicitly, since $\mathbf{F} = -\partial U/\partial \mathbf{d}$ with $U \geq 0$ and $U(\mathbf{0}) = 0$ is what makes the element passive. Dampers store nothing and are characterized instead by the power they dissipate.

Linear spring and damper. The baseline elements, used wherever no other law is stated:

$$\mathbf{F} = \mathbf{K}_d\,\mathbf{e}, \qquad U = \tfrac{1}{2}\,\mathbf{e}^T\mathbf{K}_d\,\mathbf{e}, \qquad \mathbf{F} = -\mathbf{D}_d\,\dot{\mathbf{d}}, \qquad \mathcal{P} = \dot{\mathbf{d}}^T\mathbf{D}_d\,\dot{\mathbf{d}} \geq 0. \tag{S3}$$

$U \geq 0$ for $\mathbf{K}_d \succeq 0$ and $\mathcal{P} \geq 0$ for $\mathbf{D}_d \succeq 0$, so the pair is passive for any admissible gains.

Cart-constrained elements. A cart admits motion along a single direction $\mathbf{n}_c$ and resists nothing in the orthogonal complement. With $\mathbf{P}_c = \mathbf{n}_c\mathbf{n}_c^T$ the gain is projected on both sides, which keeps the element symmetric and stores no energy in the constrained directions:

$$\mathbf{F} = \mathbf{P}_c\,\mathbf{K}_d\,\mathbf{P}_c\,\mathbf{e}, \qquad U = \tfrac{1}{2}\,\mathbf{e}^T\mathbf{P}_c\,\mathbf{K}_d\,\mathbf{P}_c\,\mathbf{e}, \qquad \mathbf{F} = -\mathbf{P}_c\,\mathbf{D}_d\,\mathbf{P}_c\,\dot{\mathbf{d}}. \tag{S4}$$

Since $\mathbf{P}_c\mathbf{K}_d\mathbf{P}_c \succeq 0$ whenever $\mathbf{K}_d \succeq 0$, the cart element is passive. Rotating $\mathbf{n}_c$ in the sagittal plane by an angle ϕ produces the directional responses reported in the main text.

Gaussian repulsive spring. A bounded repulsive field that decays with distance, used to reshape the force response over part of the stroke while leaving it unchanged elsewhere. With $\Delta\mathbf{z}$

the offset from the repulsion center,

$$\mathbf{F}_g = A \exp\left(-\frac{\|\Delta\mathbf{z}\|^2}{2\sigma^2}\right) \Delta\mathbf{z}, \qquad U_g = A\,\sigma^2 \exp\left(-\frac{\|\Delta\mathbf{z}\|^2}{2\sigma^2}\right). \tag{S5}$$

Direct differentiation confirms $\mathbf{F}_g = -\partial U_g / \partial \Delta\mathbf{z}$. The potential is a bounded barrier of height $A\sigma^2$ at the center, decaying to zero far from it, so the element can store only a finite amount of energy. The force magnitude vanishes both at the center and at infinity and peaks at $\|\Delta\mathbf{z}\| = \sigma$. A cart-constrained variant replaces $\Delta\mathbf{z}$ by $\mathbf{P}_c\Delta\mathbf{z}$ and projects the result.

Deadzone limit spring. Joint limits are enforced by an element inactive inside $[\theta_-, \theta_+]$ and linear outside it:

$$\begin{aligned} \tau_{\text{lim}} &= K_{\text{lim}} \left[\max(\theta_- - \theta, 0) - \max(\theta - \theta_+, 0)\right], \\ U_{\text{lim}} &= \tfrac{1}{2} K_{\text{lim}} \left[\max(\theta_- - \theta, 0)^2 + \max(\theta - \theta_+, 0)^2\right]. \end{aligned} \tag{S6}$$

U_{lim} is continuous and continuously differentiable at both breakpoints, so the element is conservative and does not compromise passivity.

B.2: Stiffness laws and the limits of the potential argument

Two families of element schedule their stiffness during the interaction rather than holding it fixed. Whether a potential still exists depends on *what the stiffness is scheduled on*, and the distinction separates the experiments that remain passive from those that do not.

Scheduled on the element's own deflection. If the stiffness depends only on the deflection of the element itself, the force $F(e) = K(e)\,e$ is a memoryless function of e and a potential always exists:

$$U(e) = \int_0^e K(\xi)\,\xi\,\mathrm{d}\xi \;\geq\; 0 \quad \text{for } K(\cdot) \geq 0, \tag{S7}$$

so the element is passive however sharply the stiffness varies. For the polynomial law the integral is elementary,

$$K(d) = K_0 \left(\frac{d}{d_{\text{norm}}} \right)^p, \qquad U(d) = \frac{K_0 \, d^{p+2}}{(p+2) \, d_{\text{norm}}^p}, \tag{S8}$$

recovering the linear spring at $p = 0$. For the sigmoidal law,

$$K(d) = K_{\max} - \frac{K_{\max} - K_{\min}}{1 + e^{-\alpha(d - d_{\text{th}})}}, \tag{S9}$$

which switches between two regimes about a threshold d_{th} at a rate set by α, the integral of Eq. (S7) has no elementary closed form but is bounded between the potentials of the two linear springs $K_{\min}$ and $K_{\max}$, and is evaluated numerically. The polynomial stiffness is also clamped below at $K_{\min}$ near $d = 0$ for numerical stability.

Scheduled on an exogenous signal. The contact-dependent laws are different. Here the stiffness is a function of the measured contact force F:

$$K_\theta^{\uparrow}(F) = K_{\min} + (K_{\max} - K_{\min}) \left(1 - e^{-\alpha F} \right) \tag{S10}$$

$$K_\theta^{\downarrow}(F) = K_{\min} + (K_{\max} - K_{\min}) \, e^{-\alpha F} \tag{S11}$$

for stiffening and softening respectively. Both reach the midpoint of $[K_{\min}, K_{\max}]$ at the half-transition force $F_{1/2} = \ln 2 / \alpha$, which is how the swept values of α were chosen to span the accessible force range logarithmically; $\alpha = 0$ recovers a constant stiffness, $K_{\min}$ for stiffening and $K_{\max}$ for softening, giving the baseline against which each is compared.

Because F is an external measurement rather than a function of the element's own state, the torque is no longer a memoryless function of the deflection and no potential exists: these elements are not passive by construction, and the same holds for any law scheduled on the arm displacement rather than on the element's deflection. The energy they can inject is nonetheless bounded, since the stiffness is confined to $[K_{\min}, K_{\max}]$ and the stored energy at any deflection therefore lies between the potentials of the two extreme linear springs.

B.3: Configurations on the single-finger test bed

The actuator vector is $\mathbf{q} = [q_{\mathrm{MCP}}, q_{\mathrm{PIP}}]^T$ and the joint vector $\boldsymbol{\theta} = [\theta_{\mathrm{MCP}}, \theta_{\mathrm{PIP}}, \theta_{\mathrm{DIP}}]^T$, related by Eq. (S1). Three main configurations are defined and used.

In the *finger-space* configuration the virtual coordinate is the joint vector itself, $\mathbf{d} = \boldsymbol{\theta}$, so $\mathbf{J}_d = \mathbf{J}_{\boldsymbol{\theta}} \in \mathbb{R}^{3\times 2}$, constant and given by the transmission ratios. With a shared stiffness, $\mathbf{K}_d = K_\theta \mathbf{I}_3$. Note that $\mathbf{J}_d$ has more rows than columns: three virtual coordinates are driven by two actuators, so the elements are not independently realizable and only their projection onto the actuator space is transmitted. In the *task-space* configuration the virtual coordinate is the position of a point on the distal phalanx, $\mathbf{d} = \mathbf{x}_{\mathrm{tip}} \in \mathbb{R}^3$, and $\mathbf{J}_d = \mathbf{J}_x \in \mathbb{R}^{3\times 2}$ is configuration-dependent. A cart constraint is imposed as in Eq. (S4). The cart projection $\mathbf{P}_c$ acts on the virtual element and must not be confused with the contact projection $\mathbf{P} = \mathbf{n}\mathbf{n}^T$, which acts on the output. The *mixed-space* configuration concatenates the two, $\mathbf{d} = [\boldsymbol{\theta}^T, \mathbf{x}_{\mathrm{tip}}^T]^T \in \mathbb{R}^6$, with $\mathbf{J}_d$ the vertical stacking of $\mathbf{J}_{\boldsymbol{\theta}}$ and $\mathbf{J}_x$, and $\mathbf{K}_d$ block-diagonal.

B.4: Configurations on the ADAPT Hand

The thirteen torque-controlled actuators are ordered as thumb CMC1, CMC2, MCP, and IP; the spread actuator; and then MCP and PIP for index, middle, ring, and pinky. The wrist actuators are held in position mode and do not appear in $\mathbf{q}$. Each digit contributes an independent block. Joint-space elements act on the flexion chain of each digit, giving a block-diagonal $\mathbf{K}_d$ with one block per digit; the spread joints of all four fingers are driven by a single actuator through fixed motion ratios, so their four virtual elements share one column of $\mathbf{J}_d$ and cannot be set independently. Task-space elements are attached to the five fingertips. Since the digits are kinematically independent, $\mathbf{J}_d$ is block-diagonal for these elements too. Task-space rest position are often placed by evaluating the forward kinematics at joint targets taken along the first principal component of human grasp postures. The specific joint targets differ between tasks.

C: Full force and stiffness theorem, CCT correction, and optimization for online tuning

C.1: General derivation

Let $\mathbf{q}$ be the actuator vector, $\mathbf{x}$ the output point, and $\mathbf{d}$ a vector of generalized coordinates hosting the virtual elements, with Jacobians $\mathbf{J}_x = \partial\mathbf{x}/\partial\mathbf{q}$ and $\mathbf{J}_d = \partial\mathbf{d}/\partial\mathbf{q}$. Let $\mathbf{P}$ project onto the directions along which the output performs virtual work (i.e., a force $\mathbf{f}_x$ is applied), and let $\boldsymbol{\eta}$ be the diagonal transmission efficiency in actuator space. The generalized virtual force in static conditions, without damping contributions, is $\boldsymbol{\tau}_d = \mathbf{K}_d(\mathbf{d}_{\text{ref}} - \mathbf{d})$.

Equating the virtual work performed by the elements to that performed at the output, and substituting $\dot{\mathbf{d}} = \mathbf{J}_d\dot{\mathbf{q}}$ and $\dot{\mathbf{x}} = \mathbf{J}_x\dot{\mathbf{q}}$, gives for arbitrary $\dot{\mathbf{q}}$ the balance:

$$\boldsymbol{\eta}\,\mathbf{J}_d^T\boldsymbol{\tau}_d = (\mathbf{P}\mathbf{J}_x)^T\,\mathbf{f}_x, \tag{S12}$$

whose least-squares solution is the contact force:

$$\mathbf{f}_x = ((\mathbf{P}\mathbf{J}_x)^*)^T\,\boldsymbol{\eta}\,\mathbf{J}_d^T\,\mathbf{K}_d\,(\mathbf{d}_{\text{ref}} - \mathbf{d})\,. \tag{S13}$$

Theorem 1 (VMC stiffness composition)**.** *Consider a tendon-driven system with actuator vector* $\mathbf{q} \in \mathbb{R}^{n_q}$*, output Jacobian* $\mathbf{J}_x$*, output projection* $\mathbf{P}$*, and diagonal transmission efficiency* $\boldsymbol{\eta}$ *with entries in* $(0, 1]$*, constant with respect to* $\mathbf{q}$*. Let a set of virtual elements be defined on generalized coordinates* $\mathbf{d}$ *with Jacobian* $\mathbf{J}_d$ *and positive semi-definite stiffness* $\mathbf{K}_d$*. Then the output-space stiffness is, to first order,*

$$\mathbf{K}_x = ((\mathbf{P}\mathbf{J}_x)^*)^T\,\boldsymbol{\eta}\,\mathbf{J}_d^T\mathbf{K}_d\mathbf{J}_d\,(\mathbf{P}\mathbf{J}_x)^*,$$

and, if the elements are decoupled so that $\mathbf{K}_d$ *is block-diagonal with blocks* k_i*,*

$$\mathbf{K}_x = ((\mathbf{P}\mathbf{J}_x)^*)^T\,\boldsymbol{\eta}\left(\sum_i \mathbf{J}_{d_i}^T\,k_i\,\mathbf{J}_{d_i}\right)(\mathbf{P}\mathbf{J}_x)^*.$$

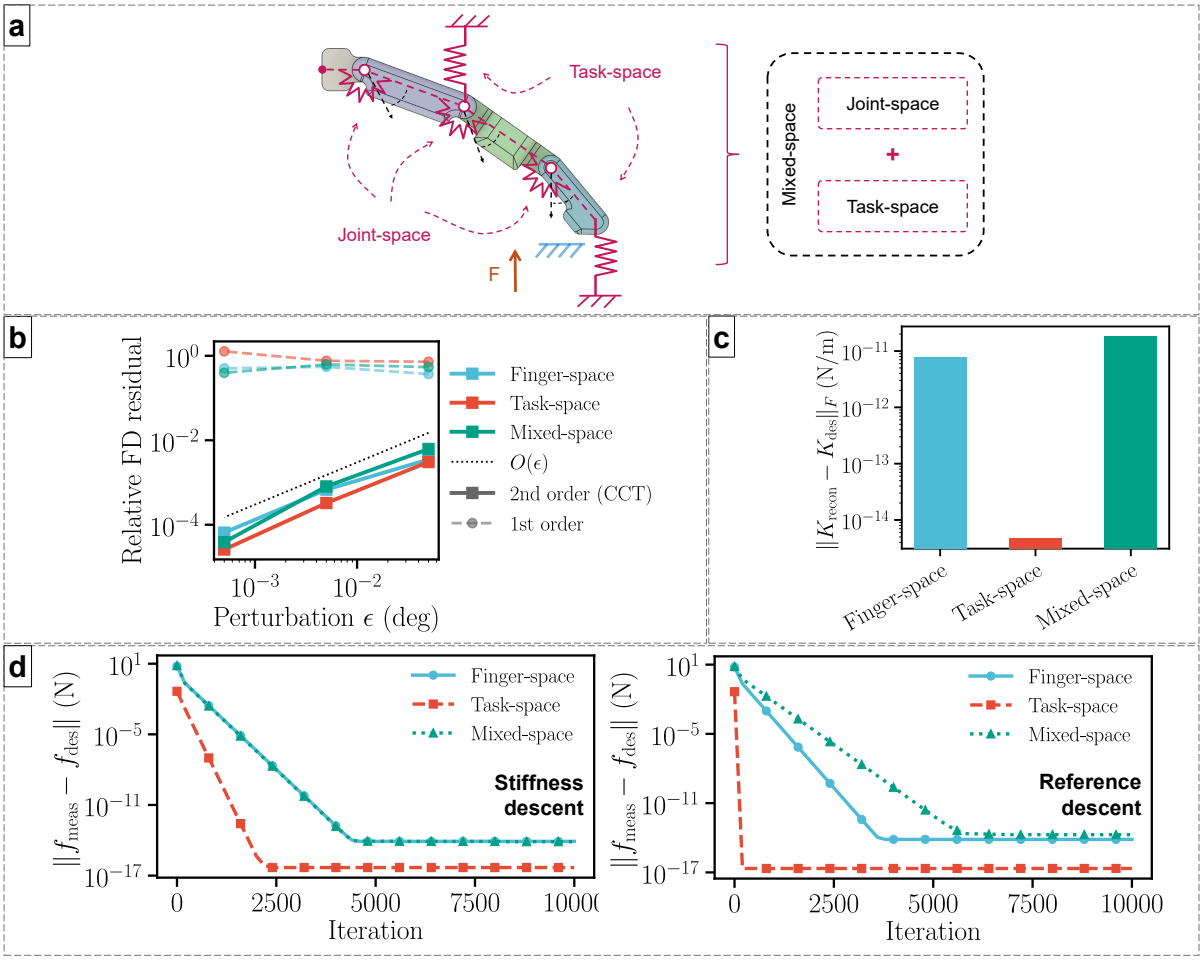


Figure S5: **Numerical validation of the VMC stiffness model and of the force-tracking gradient descent on the single-finger platform**. **a** Finger-space, task-space, and mixed-space virtual element configuration used for validation. **b** Relative residual between the analytically predicted stiffness and a local, finite-difference estimated obtained by perturbing the configuration, as a function of perturbation size, compared to first-order and second-order (CCT-corrected) predictions. **c** Fröbenius-norm error of the feed-forward stiffness inversion: the task-space stiffness achieved by inverting a desired stiffness into virtual-element parameters, compared to that desired stiffness, fo reach configuration. **d** Convergence of the force error during gradient-descent adaptation of the virtual stiffness (left) and the virtual reference (right), across the three control configurations.

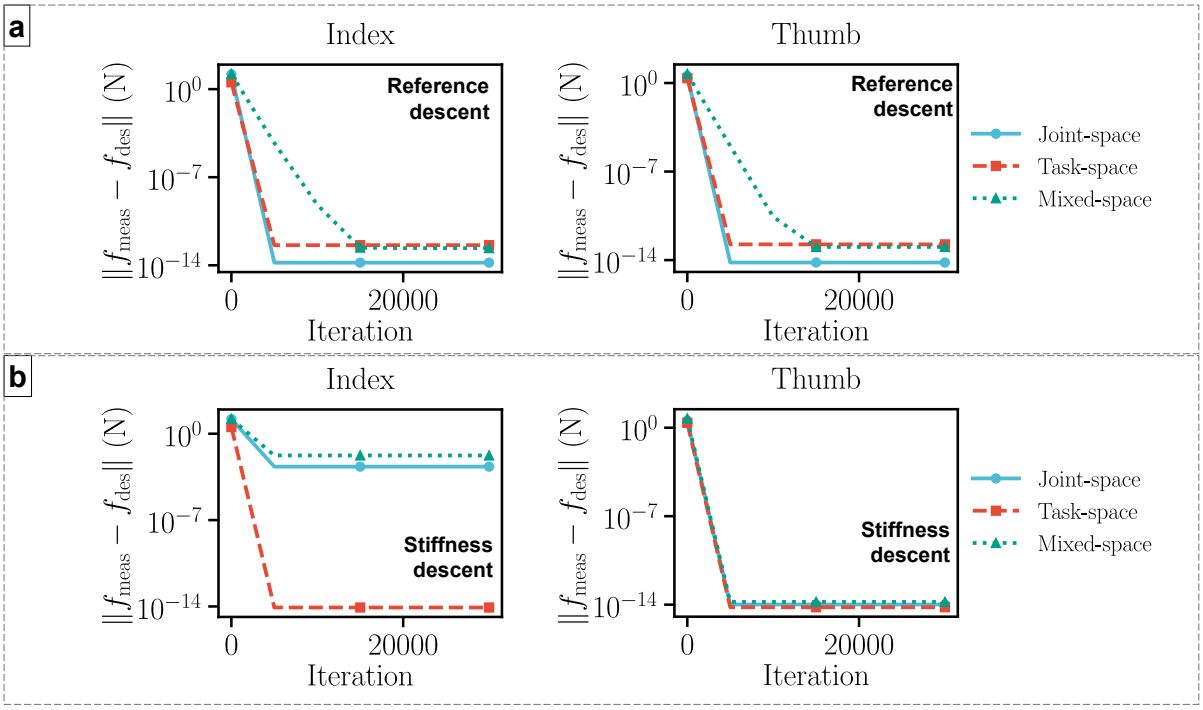


Figure S6: **Convergence of force-tracking gradient descent on the hand platform**. **a** Convergence of the force error during reference-descent adaptation for the index and thumb fingers, across joint-space, task-space, and mixed-space virtual elements. **b** Convergence of the force error during stiffness-descent adaptation for the index and thumb fingers, across the same three configurations.

The force and stiffness at the output are therefore fully determined by the virtual parameters, the kinematic structure, the transmission efficiency, and the output projection, and contributions from elements defined in different coordinate spaces compose additively.

Proof. Differentiate Eq. (S12) with respect to $\mathbf{q}$. Writing $d\boldsymbol{\tau}_d = -\mathbf{K}_d\, d\mathbf{d} = -\mathbf{K}_d\mathbf{J}_d\, d\mathbf{q}$ and $d\mathbf{f}_x = -\mathbf{K}_x\, d(\mathbf{P}\mathbf{x}) = -\mathbf{K}_x\mathbf{P}\mathbf{J}_x\, d\mathbf{q}$, and retaining only the terms in which the Jacobians are held constant, gives

$$-\boldsymbol{\eta}\,\mathbf{J}_d^T\mathbf{K}_d\mathbf{J}_d = -\left(\mathbf{P}\mathbf{J}_x\right)^T\mathbf{K}_x\left(\mathbf{P}\mathbf{J}_x\right).$$

Solving in the least-squares sense yields the stated expression. The decoupled form follows by partitioning $\mathbf{J}_d$ row-wise into the blocks associated with each element and expanding the block-diagonal $\mathbf{K}_d$, the cross terms vanishing. Since the derivation nowhere inverts $\mathbf{J}_d$, no rank condition on $\mathbf{J}_d$ is needed. □

Corollary 2 (Exact second-order stiffness)**.** *Retaining the terms in which the Jacobians vary with configuration,*

$$\mathbf{K}_x = \left((\mathbf{P}\mathbf{J}_x)^*\right)^T\left[\boldsymbol{\eta}\,\mathbf{J}_d^T\mathbf{K}_d\mathbf{J}_d + \frac{\partial(\mathbf{P}\mathbf{J}_x)^T}{\partial\mathbf{q}}\,\mathbf{f}_x - \frac{\partial(\boldsymbol{\eta}\,\mathbf{J}_d^T)}{\partial\mathbf{q}}\,\boldsymbol{\tau}_d\right](\mathbf{P}\mathbf{J}_x)^*. \tag{S14}$$

The two correction terms are the geometric stiffness contributions, involving the Hessians of the output and virtual-element Jacobians weighted respectively by the external force and by the virtual torque.

Proof. Immediate from the same differentiation, retaining the Jacobian derivatives. Both Hessians are available analytically from the symbolic kinematic model, so Eq. (S14) is evaluable at every control cycle. □

C.2: Feed-forward inversion with several element groups

Consider first a single group of virtual elements. Theorem 1 gives $\mathbf{K}_x = \mathbf{L}\mathbf{K}_d\mathbf{R}$ with $\mathbf{L} = \left((\mathbf{P}\mathbf{J}_x)^*\right)^T\boldsymbol{\eta}\,\mathbf{J}_d^T$ and $\mathbf{R} = \mathbf{J}_d(\mathbf{P}\mathbf{J}_x)^*$, both fixed at the current configuration. The unknown $\mathbf{K}_d$

appears between the two maps, so the relation is not in the form of a single matrix acting on a vector of unknowns and cannot be inverted directly. Applying the identity $\mathrm{vec}(\mathbf{AXB}) = (\mathbf{B}^T \otimes \mathbf{A})\,\mathrm{vec}(\mathbf{X})$ with $\mathbf{A} = \mathbf{L}$, $\mathbf{X} = \mathbf{K}_d$ and $\mathbf{B} = \mathbf{R}$:

$$\mathrm{vec}(\mathbf{K}_x) = \left(\mathbf{R}^T \otimes \mathbf{L}\right)\mathrm{vec}(\mathbf{K}_d) =: \mathbf{M}\,\mathrm{vec}(\mathbf{K}_d), \tag{S15}$$

a linear system in the stacked unknowns. Inverting it in the least-squares sense:

$$\mathrm{vec}\left(\mathbf{K}_d^{\mathrm{ff}}\right) = \mathbf{M}^*\,\mathrm{vec}(\mathbf{K}_{x,\mathrm{des}})\,. \tag{S16}$$

Because $\|\,\mathrm{vec}(\mathbf{X})\|_2 = \|\mathbf{X}\|_F$, the residual minimized by the pseudoinverse is the Frobenius distance $\|\mathbf{L}\mathbf{K}_d\mathbf{R} - \mathbf{K}_{x,\mathrm{des}}\|_F$, and among all minimizers the solution returned is the one of smallest $\|\mathbf{K}_d\|_F$. The requested stiffness is reproduced exactly when $\mathrm{vec}(\mathbf{K}_{x,\mathrm{des}})$ lies in the range of $\mathbf{M}$, that is when $\mathbf{M}\mathbf{M}^*\,\mathrm{vec}(\mathbf{K}_{x,\mathrm{des}}) = \mathrm{vec}(\mathbf{K}_{x,\mathrm{des}})$, and approximated in the above sense otherwise. When several groups of virtual elements act on a single output point, the stiffness is $\mathbf{K}_x = \sum_g \mathbf{L}_g\mathbf{K}_{d_g}\mathbf{R}_g$, with $\mathbf{L}_g = ((\mathbf{P}\mathbf{J}_x)^*)^T\boldsymbol{\eta}\,\mathbf{J}_{d_g}^T$ and $\mathbf{R}_g = \mathbf{J}_{d_g}(\mathbf{P}\mathbf{J}_x)^*$. Because each unknown is bounded by a different kinematic map, the groups must be inverted jointly rather than separately. Defining $\mathbf{M}_g = \mathbf{R}_g^T \otimes \mathbf{L}_g$, with $\otimes$ the Kronecker product, and stacking horizontally,

$$\begin{bmatrix} \mathrm{vec}(\mathbf{K}_{d_1}) \\ \vdots \\ \mathrm{vec}(\mathbf{K}_{d_G}) \end{bmatrix} = \begin{bmatrix} \mathbf{M}_1 & \cdots & \mathbf{M}_G \end{bmatrix}^* \mathrm{vec}(\mathbf{K}_{x,\mathrm{des}})\,, \tag{S17}$$

which distributes the requested stiffness optimally across the available groups and can be re-evaluated at each time step to track a time-varying profile.

C.3: Numerical validation

Figure S5 validates the model and the gradient-descent schemes on the three single-finger configurations. Fig. S5**a** shows the element layouts. Fig. S5**b** compares the analytically predicted

stiffness against a finite-difference estimate obtained by perturbing the configuration, as a function of the perturbation magnitude: the second-order expression is the more accurate of the two, and the error of both decreases as the perturbation is refined. Fig. S5**c** reports the Frobenius-norm error of the feed-forward inversion, which remains of the order of 10^{-11}. Fig. S5**d** shows the convergence of the force error under both adaptation schemes, on the stiffness and on the rest configuration, across the three configurations. The same force adaptation schemes on the hand index and thumb are shown in Fig. S6.

C.4: Convergence and admissible step sizes

The adaptation schemes are gradient steps on a loss whose model is exact only instantaneously, since the configuration moves as the parameters change. This section establishes the step sizes for which each scheme is well posed. Throughout, $\mathbf{A}_i = ((\mathbf{P}\mathbf{J}_x)^*)^T \boldsymbol{\eta}\, \mathbf{J}_d^T$ evaluated at iteration i, $\boldsymbol{u}_i = \mathbf{d}_{\text{ref}} - \mathbf{d}_i$, $\boldsymbol{v}_i = \mathbf{A}_i^T \mathbf{n}$, and $e_i = F_i - F_{\text{ref}}$ is the scalar force error along the contact normal. With this notation the contact force of Eq. (S13) reads $\mathbf{f}_{x,i} = \mathbf{A}_i \mathbf{K}_d^{(i)} \mathbf{u}_i$, and the corresponding loss becomes:

$$\mathcal{L} = \tfrac{1}{2} \left\| \mathbf{A}_i \mathbf{K}_d^{(i)} \mathbf{u}_i - \mathbf{f}_{x,\text{ref}} \right\|^2 = \tfrac{1}{2}\, \mathbf{e}_i^T \mathbf{e}_i, \qquad \mathbf{e}_i = \mathbf{f}_{x,i} - \mathbf{f}_{x,\text{ref}}. \tag{S18}$$

Both gradients are obtained by perturbing one parameter at frozen configuration: $\mathbf{d}_i$, and with it $\mathbf{A}_i$, are treated as independent of the parameters, so the terms $\partial \mathbf{d}/\partial \mathbf{K}_d$ and $\partial \mathbf{d}/\partial \mathbf{d}_{\text{ref}}$ are neglected. This instantaneous approximation is the reason the admissible step sizes derived below are necessary conditions on the frozen problem. In both cases the first variation of the loss is $\delta\mathcal{L} = \mathbf{e}_i^T \delta \mathbf{e}_i$, so only $\delta \mathbf{e}_i$ has to be computed.

Stiffness. Perturbing $\mathbf{K}_d^{(i)}$ by $\delta\mathbf{K}$, at fixed $\mathbf{u}_i$, gives $\delta \mathbf{e}_i = \mathbf{A}_i\, \delta\mathbf{K}\, \mathbf{u}_i$ and therefore

$$\delta\mathcal{L} = \mathbf{e}_i^T \mathbf{A}_i\, \delta\mathbf{K}\, \mathbf{u}_i = \left(\mathbf{A}_i^T \mathbf{e}_i\right)^T \delta\mathbf{K}\, \mathbf{u}_i. \tag{S19}$$

This is a scalar of the form $\mathbf{a}^T\,\delta\mathbf{X}\,\mathbf{b}$, whose gradient with respect to $\mathbf{X}$ is $\mathbf{a}\mathbf{b}^T$, so

$$\nabla_{\mathbf{K}_d}\mathcal{L} = \mathbf{A}_i^T\mathbf{e}_i\,\mathbf{u}_i^T, \qquad \mathbf{A}_i^T = \mathbf{J}_d\,\boldsymbol{\eta}^T(\mathbf{P}\mathbf{J}_x)^*. \tag{S20}$$

For a frictionless point contact, $\mathbf{P} = \mathbf{n}\mathbf{n}^T$ and the force is directed along the normal, so $\mathbf{e}_i = e_i\mathbf{n}$ and $\mathbf{A}_i^T\mathbf{e}_i = e_i\mathbf{A}_i^T\mathbf{n} = e_i\mathbf{v}_i$, giving the rank-one form used below. This is an outer product of the sensitivity $\mathbf{v}_i$ and the deflection $\mathbf{u}_i$; since the two need not be aligned, this may leave $\mathbf{K}_d$ asymmetric, addressed in Proposition 5.

Rest configuration. Perturbing $\mathbf{d}_{\text{ref}}$ by $\delta\mathbf{d}_{\text{ref}}$, at fixed $\mathbf{K}_d^{(i)}$, gives $\delta\mathbf{u}_i = \delta\mathbf{d}_{\text{ref}}$ and hence $\delta\mathbf{e}_i = \mathbf{A}_i\mathbf{K}_d^{(i)}\,\delta\mathbf{d}_{\text{ref}} = \mathbf{S}_i\,\delta\mathbf{d}_{\text{ref}}$, where $\mathbf{S}_i := \mathbf{A}_i\mathbf{K}_d^{(i)}$ is the sensitivity of the force to the rest configuration. Therefore:

$$\delta\mathcal{L} = \mathbf{e}_i^T\mathbf{S}_i\,\delta\mathbf{d}_{\text{ref}} = \left(\mathbf{S}_i^T\mathbf{e}_i\right)^T\delta\mathbf{d}_{\text{ref}}. \tag{S21}$$

This is a scalar of the form $\mathbf{c}^T\,\delta\mathbf{y}$, whose gradient with respect to $\mathbf{y}$ is $\mathbf{c}$, so

$$\nabla_{\mathbf{d}_{\text{ref}}}\mathcal{L} = \mathbf{S}_i^T\mathbf{e}_i = \mathbf{K}_d^{(i)T}\mathbf{A}_i^T\mathbf{e}_i. \tag{S22}$$

The two updates therefore read:

$$\mathbf{K}_d^{(i+1)} = \mathbf{K}_d^{(i)} - \alpha\,e_i\,\boldsymbol{v}_i\boldsymbol{u}_i^T, \qquad \mathbf{d}_{\text{ref}}^{(i+1)} = \mathbf{d}_{\text{ref}}^{(i)} - \alpha\,\mathbf{S}_i^T\left(\mathbf{f}_{x,i} - \mathbf{f}_{x,\text{ref}}\right), \tag{S23}$$

with $\mathbf{S}_i = ((\mathbf{P}\mathbf{J}_x)^*)^T\boldsymbol{\eta}\,\mathbf{J}_d^T\mathbf{K}_d^{(i)}$ and $\alpha > 0$ the step size.

Lemma 1 (Preservation of positive definiteness)**.** *Let $\mathbf{K}_d^{(i)}$ be positive definite and set $\lambda_i = \lambda_{\min}\left(\frac{1}{2}(\mathbf{K}_d^{(i)} + \mathbf{K}_d^{(i)T})\right) > 0$ and $\beta_i = |e_i|\,\|\boldsymbol{u}_i\|\,\|\boldsymbol{v}_i\|$.* (a) *If $0 < \alpha < \lambda_i/\beta_i$, then $\mathbf{K}_d^{(i+1)}$ from Eq.* (S23) *is positive definite.* (b) *If in addition $\lambda_i \geq \underline{\lambda} > 0$ and $\beta_i \leq \overline{\beta}$ for $i = 0, \ldots, N-1$, then any constant $0 < \alpha < \underline{\lambda}/\overline{\beta}$ keeps $\mathbf{K}_d^{(i)}$ positive definite for all $i = 0, \ldots, N$.*

Proof. For any unit vector $\boldsymbol{x}$, $\boldsymbol{x}^T\mathbf{K}_d^{(i+1)}\boldsymbol{x} = \boldsymbol{x}^T\mathbf{K}_d^{(i)}\boldsymbol{x} - \alpha e_i(\boldsymbol{x}^T\boldsymbol{v}_i)(\boldsymbol{u}_i^T\boldsymbol{x})$. The first term is at least λ_i, and by Cauchy–Schwarz the second is bounded in magnitude by $\alpha\beta_i$, so $\boldsymbol{x}^T\mathbf{K}_d^{(i+1)}\boldsymbol{x} \geq \lambda_i - \alpha\beta_i > 0$ under the stated condition, proving (a). Under the uniform bounds, $\lambda_i/\beta_i \geq \underline{\lambda}/\overline{\beta}$ for every i, so the condition of (a) holds at each step and (b) follows by induction. □

Proposition 3 (Convergence of stiffness adaptation)**.** *For a frictionless point contact with* $\mathbf{P} = \mathbf{n}\mathbf{n}^T$*, the stiffness update of Eq.* (S23) *produces the error recursion* $e_{i+1} = (1 - \alpha\gamma_i)e_i$ *with* $\gamma_i = \|\boldsymbol{v}_i\|^2\|\boldsymbol{u}_i\|^2$*. The error is therefore convergent if and only if* $0 < \alpha < 2/\gamma_i$*, and monotone if* $0 < \alpha < 1/\gamma_i$*. If* $\gamma_i = 0$ *the error is unchanged.*

Proof. The scalar force along the contact normal follows from Eq. (S13): $F_i = \mathbf{n}^T\mathbf{f}_{x,i} = \mathbf{n}^T\mathbf{A}_i\mathbf{K}_d^{(i)}\boldsymbol{u}_i = \boldsymbol{v}_i^T\mathbf{K}_d^{(i)}\boldsymbol{u}_i$ so the force is a bilinear form in the stiffness, with $\boldsymbol{v}_i$ and $\boldsymbol{u}_i$ fixed by the configuration. Holding the configuration frozen, so that $\boldsymbol{v}_i$ and $\boldsymbol{u}_i$ are unchanged by the update, and substituting the stiffness update of Eq. (S23),

$$F_{i+1} = \boldsymbol{v}_i^T\mathbf{K}_d^{(i+1)}\boldsymbol{u}_i = \boldsymbol{v}_i^T\mathbf{K}_d^{(i)}\boldsymbol{u}_i - \alpha e_i\,\boldsymbol{v}_i^T\big(\boldsymbol{v}_i\boldsymbol{u}_i^T\big)\boldsymbol{u}_i = F_i - \alpha e_i\|\boldsymbol{v}_i\|^2\|\boldsymbol{u}_i\|^2,$$

where the rank-one term collapses because $\boldsymbol{v}_i^T\boldsymbol{v}_i\boldsymbol{u}_i^T\boldsymbol{u}_i = \|\boldsymbol{v}_i\|^2\|\boldsymbol{u}_i\|^2$. Subtracting the constant reference F_{ref} from both sides gives $e_{i+1} = e_i - \alpha\gamma_i e_i = (1 - \alpha\gamma_i)e_i$. The recursion is a scalar contraction, so $e_i \to 0$ if and only if $|1 - \alpha\gamma_i| < 1$, that is $0 < \alpha\gamma_i < 2$; the error additionally keeps its sign at every step when $1 - \alpha\gamma_i > 0$, that is $\alpha\gamma_i < 1$. If $\gamma_i = 0$, either $\boldsymbol{u}_i = \mathbf{0}$, the element is undeflected, or $\boldsymbol{v}_i = \mathbf{0}$, the contact normal lies in the null space of $\mathbf{A}_i^T$: in both cases the update produces no force change. □

Proposition 4 (Convergence of reference adaptation)**.** *For a frictionless point contact with* $\mathbf{P} = \mathbf{n}\mathbf{n}^T$*, the reference update of Eq.* (S23) *produces the error recursion* $e_{i+1} = (1 - \alpha\nu_i)e_i$ *with* $\nu_i = \|\boldsymbol{s}_i\|^2$ *and* $\boldsymbol{s}_i = \mathbf{S}_i^T\mathbf{n}$*. The error is therefore convergent if and only if* $0 < \alpha < 2/\nu_i$*, and monotone if* $0 < \alpha < 1/\nu_i$*. If* $\nu_i = 0$ *the error is unchanged.*

Proof. Eq. (S13) is linear in the rest configuration, $\mathbf{f}_{x,i} = \mathbf{S}_i(\mathbf{d}_{\text{ref}}^{(i)} - \mathbf{d}_i)$, so the scalar force along the contact normal is

$$F_i = \mathbf{n}^T \mathbf{f}_{x,i} = \mathbf{n}^T \mathbf{S}_i \left(\mathbf{d}_{\text{ref}}^{(i)} - \mathbf{d}_i \right) = \boldsymbol{s}_i^T \left(\mathbf{d}_{\text{ref}}^{(i)} - \mathbf{d}_i \right),$$

linear in the rest configuration with $\boldsymbol{s}_i$ fixed by the configuration and the current stiffness. Holding $\mathbf{d}_i$ and $\boldsymbol{s}_i$ frozen and substituting the update $\mathbf{d}_{\text{ref}}^{(i+1)} = \mathbf{d}_{\text{ref}}^{(i)} - \alpha e_i \boldsymbol{s}_i$,

$$F_{i+1} = \boldsymbol{s}_i^T \left(\mathbf{d}_{\text{ref}}^{(i)} - \alpha e_i \boldsymbol{s}_i - \mathbf{d}_i \right) = F_i - \alpha e_i \|\boldsymbol{s}_i\|^2.$$

Subtracting the constant reference F_{ref} from both sides gives $e_{i+1} = (1 - \alpha\nu_i)e_i$. As in Proposition 3 the recursion is a scalar contraction, so $e_i \to 0$ if and only if $|1 - \alpha\nu_i| < 1$, that is $0 < \alpha\nu_i < 2$, and the error keeps its sign at every step when $\alpha\nu_i < 1$. If $\nu_i = 0$ the contact normal lies in the null space of $\mathbf{S}_i^T$ and the update produces no force change. □

Both propositions describe the instantaneous behavior at frozen configuration. In practice $\mathbf{d}$ moves as the parameters change, which is why the step sizes used experimentally are well below the bounds and why several iterations are required.

C.5: Dissipativity under an asymmetric stiffness

A virtual element with symmetric $\mathbf{K}_d$ is passive by construction, since $\mathbf{K}_d$ is then the Hessian of a quadratic potential. The update of Eq. (S23) does not enforce this symmetry, and when $\mathbf{K}_d$ is not symmetric it no longer derives from a potential. The following proposition covers this case directly, showing that the closed loop remains dissipative under sufficient damping regardless.

Proposition 5 (Dissipativity under sufficient damping)**.** *Consider the linearized response about equilibrium,* $\boldsymbol{\xi} := \mathbf{d}_{\text{ref}} - \mathbf{d}$*, under the total damping* $\mathbf{B} \succ 0$ *collecting the physical and the virtual contributions, and reflected inertia* $\mathbf{M} \succ 0$*,*

$$\mathbf{M}\ddot{\boldsymbol{\xi}} + \mathbf{B}\dot{\boldsymbol{\xi}} + \mathbf{K}_d\boldsymbol{\xi} = \mathbf{0}, \qquad \mathbf{K}_d = \mathbf{K}_{\text{sym}} + \mathbf{K}_{\text{skew}},$$

with $\mathbf{K}_{\mathrm{sym}} \succ 0$. *Let* $\mu = \lambda_{\max}(\mathbf{M})$, $\underline{\beta} = \lambda_{\min}(\mathbf{B})$, $\overline{\beta} = \lambda_{\max}(\mathbf{B})$, $\kappa = \lambda_{\min}(\mathbf{K}_{\mathrm{sym}})$, *and let* $\varsigma = \|\mathbf{K}_{\mathrm{skew}}\|_2$ *be the induced 2-norm of the skew part, that is its largest singular value. If*

$$\varsigma \;<\; \underline{\beta}\left(\sqrt{\kappa/\mu} - \overline{\beta}/(2\mu)\right),$$

then the origin is exponentially stable and the element dissipates net energy along every trajectory.

Proof. Let $\varepsilon = \underline{\beta}/(2\mu)$ and take

$$E = \tfrac{1}{2}\dot{\boldsymbol{\xi}}^T\mathbf{M}\dot{\boldsymbol{\xi}} + \tfrac{1}{2}\boldsymbol{\xi}^T\mathbf{K}_{\mathrm{sym}}\boldsymbol{\xi} + \varepsilon\,\boldsymbol{\xi}^T\mathbf{M}\dot{\boldsymbol{\xi}},$$

the mechanical energy of the symmetric part plus a cross term. Differentiating and substituting $\mathbf{M}\ddot{\boldsymbol{\xi}} = -\mathbf{B}\dot{\boldsymbol{\xi}} - \mathbf{K}_d\boldsymbol{\xi}$ in the two terms that carry $\ddot{\boldsymbol{\xi}}$,

$$\dot{E} = \dot{\boldsymbol{\xi}}^T\mathbf{M}\ddot{\boldsymbol{\xi}} + \boldsymbol{\xi}^T\mathbf{K}_{\mathrm{sym}}\dot{\boldsymbol{\xi}} + \varepsilon\dot{\boldsymbol{\xi}}^T\mathbf{M}\dot{\boldsymbol{\xi}} + \varepsilon\,\boldsymbol{\xi}^T\mathbf{M}\ddot{\boldsymbol{\xi}},$$

$$\dot{E} = -\dot{\boldsymbol{\xi}}^T\mathbf{B}\dot{\boldsymbol{\xi}} - \dot{\boldsymbol{\xi}}^T\mathbf{K}_d\boldsymbol{\xi} + \boldsymbol{\xi}^T\mathbf{K}_{\mathrm{sym}}\dot{\boldsymbol{\xi}} + \varepsilon\dot{\boldsymbol{\xi}}^T\mathbf{M}\dot{\boldsymbol{\xi}} - \varepsilon\,\boldsymbol{\xi}^T\mathbf{B}\dot{\boldsymbol{\xi}} - \varepsilon\,\boldsymbol{\xi}^T\mathbf{K}_d\boldsymbol{\xi}.$$

Two simplifications follow from the splitting of $\mathbf{K}_d$. In the last term $\boldsymbol{\xi}^T\mathbf{K}_{\mathrm{skew}}\boldsymbol{\xi} = 0$, because a skew-symmetric form vanishes on its own argument, so it reduces to $-\varepsilon\,\boldsymbol{\xi}^T\mathbf{K}_{\mathrm{sym}}\boldsymbol{\xi}$. In the second and third terms the symmetric parts cancel, since $\dot{\boldsymbol{\xi}}^T\mathbf{K}_{\mathrm{sym}}\boldsymbol{\xi} = \boldsymbol{\xi}^T\mathbf{K}_{\mathrm{sym}}\dot{\boldsymbol{\xi}}$, leaving only the skew contribution. Hence

$$\dot{E} = -\dot{\boldsymbol{\xi}}^T(\mathbf{B} - \varepsilon\mathbf{M})\dot{\boldsymbol{\xi}} - \varepsilon\,\boldsymbol{\xi}^T\mathbf{K}_{\mathrm{sym}}\boldsymbol{\xi} - \dot{\boldsymbol{\xi}}^T\mathbf{K}_{\mathrm{skew}}\boldsymbol{\xi} - \varepsilon\,\boldsymbol{\xi}^T\mathbf{B}\dot{\boldsymbol{\xi}}.$$

Bound the four terms. Since $\varepsilon\mathbf{M} \preceq \varepsilon\mu\mathbf{I} = (\underline{\beta}/2)\mathbf{I}$ and $\mathbf{B} \succeq \underline{\beta}\mathbf{I}$, the first gives $\mathbf{B} - \varepsilon\mathbf{M} \succeq (\underline{\beta}/2)\mathbf{I}$. The second is at least $\varepsilon\kappa\|\boldsymbol{\xi}\|^2$. The two cross terms are bounded by Cauchy–Schwarz by $\varsigma\|\boldsymbol{\xi}\|\|\dot{\boldsymbol{\xi}}\|$, since $\|\mathbf{K}_{\mathrm{skew}}\boldsymbol{\xi}\| \le \varsigma\|\boldsymbol{\xi}\|$, and by $\varepsilon\overline{\beta}\|\boldsymbol{\xi}\|\|\dot{\boldsymbol{\xi}}\|$. Therefore

$$\dot{E} \;\le\; -\tfrac{\underline{\beta}}{2}\|\dot{\boldsymbol{\xi}}\|^2 - \varepsilon\kappa\|\boldsymbol{\xi}\|^2 + (\varsigma + \varepsilon\overline{\beta})\|\boldsymbol{\xi}\|\|\dot{\boldsymbol{\xi}}\|,$$

a quadratic form in $(\|\boldsymbol{\xi}\|, \|\dot{\boldsymbol{\xi}}\|)$. It is negative definite exactly when its discriminant is negative, that is when $(\varsigma + \varepsilon\overline{\beta})^2 < 4 \cdot \frac{\underline{\beta}}{2} \cdot \varepsilon\kappa = 2\underline{\beta}\varepsilon\kappa$. Substituting $\varepsilon = \underline{\beta}/(2\mu)$ turns the right-hand side into $\underline{\beta}^2\kappa/\mu$, and taking square roots gives $\varsigma + \underline{\beta}\,\overline{\beta}/(2\mu) < \underline{\beta}\sqrt{\kappa/\mu}$, which is the stated condition.

The condition also makes E a valid storage function. Writing $\mathbf{z} = [\boldsymbol{\xi}^T, \dot{\boldsymbol{\xi}}^T]^T$ gives $E = \frac{1}{2}\mathbf{z}^T\mathbf{P}\mathbf{z}$ with $\mathbf{P} = \left[\begin{smallmatrix} \mathbf{K}_{\mathrm{sym}} & \varepsilon\mathbf{M} \\ \varepsilon\mathbf{M} & \mathbf{M} \end{smallmatrix}\right]$, and by the Schur complement $\mathbf{P} \succ 0$ if and only if $\mathbf{K}_{\mathrm{sym}} \succ \varepsilon^2\mathbf{M}$, for which $\varepsilon < \sqrt{\kappa/\mu}$ suffices. Since $\varsigma \geq 0$ the stated condition forces $\sqrt{\kappa/\mu} > \overline{\beta}/(2\mu) \geq \underline{\beta}/(2\mu) = \varepsilon$, so $\mathbf{P} \succ 0$. With E positive definite and $\dot{E} \leq -c(\|\boldsymbol{\xi}\|^2 + \|\dot{\boldsymbol{\xi}}\|^2)$ for some $c > 0$, exponential stability and the dissipation inequality follow. $\square$

D: Description of additional experiments

This section contains the description of additional experiments and characterizations supporting the results in the main text, and is divided as follows:

1. **Stiffness sweep with torsional and linear springs**
2. **Softening on contact**
3. **Sigmoidal and polynomial stiffness sweep**
4. **Force prediction for various VMC configurations**

Table S4 and Table S5 collect the element configuration and parameters of every experiment reported in the main text and here.

D.1: Stiffness sweep with torsional and linear springs

Fig. S7 shows the sweeps of the main text on three representative springs values, with loading and unloading shown separately. Fig. S7**a** reports the torsional configuration and Fig. S7**b** the cart-constrained fingertip spring. Both exhibit hysteresis, the unloading branch lying below the loading branch because of static friction between the silicone skin and the load-cell plate.

D.2: Softening on contact

Fig. S8 reports the inverse of the stiffening law of the main text. The finger begins stiff and softens with contact force according to the expression in Eq. (S11). Softening flattens the force-displacement curve as contact develops, the opposite of the stiffening behavior and the regime appropriate to fragile objects.

Table S4: **Virtual element configuration per experiment, single-finger test bed**. One row per figure panel, giving the element configuration, its parameters, and the number of independent repetitions N. Shared protocol: 20 mm descent at 2 mm/s, references at 30°, and virtual damping 0.003 N $\cdot$ m $\cdot$ s/rad.

Panel	Configuration	Parameters	N
Passive compliance			
Fig. 3a	finger-space	$K_\theta = 0.10,\ 0.20,\ 0.60$ N $\cdot$ m/rad; dense sweep of 10 values over $[0.02, 0.60]$	5
Fig. 3b	task-space, cart	$K_c = 10,\ 20,\ 100$ N/m; dense sweep of 10 over $[5, 280]$; cart offset 0.10 m, damping 1.0 N $\cdot$ s/m	5
Fig. 3c	finger-space	$K_\theta = 0.1,\ 0.6$ N $\cdot$ m/rad; start offset $-5, 0, +5$ mm; descent 10 mm	5
Fig. 3d	task-space, cart	$K_c = 100$ N/m fixed; $\phi = 0,\ -30,\ -60°$	5
Online modulation			
Fig. 5a	finger-space	stiffening, $[K_{\min}, K_{\max}] = [0.10, 0.60]$, $\alpha = 0,\ 0.3,\ 2.0$ N^{-1}	5
Fig. 5b	mixed	base $K_\theta = 0.5$ N $\cdot$ m/rad; Gaussian $\sigma = 10$ mm, $A = 0,\ 300,\ 600$ N/m, active over the middle half	5
Sensing and force control			
Fig. 7b	finger-space	transmission identification; stiffness triplets from $K_\theta \in [0.05, 1.0]$ N $\cdot$ m/rad; fingertip forces 0.4 to 1.5 N	200
Fig. 8b	finger-space	$\mathbf{K}_d$-descent, $\alpha = 10^{-4}$; square $0.5 \leftrightarrow 0.8$ N, 30 s holds, 3 cycles	5
Fig. 8c	finger-space	$\mathbf{d}_{\text{ref}}$-descent, $\alpha = 5 \times 10^{-4}$; same reference	5
Fig. 8d	finger-space	open loop, both schemes; staircase $0.4,\ 0.7,\ 1.0$ N, 60 s holds	5
Controller validation			
Fig. 10a	passive, no VMC	printed TPU fingers, soft and hard joints, rest angle 30°	5
Fig. 10b	finger-space	K_θ set once per run from the effective stiffness calibration, piecewise linear interpolation	5
Fig. 10c	finger-space	feed-forward inversion of the local K_n from the TPU curves, offset 0.05 N$\cdot$m/rad; $\boldsymbol{\theta}_{\text{ref}}$-descent for force tracking	5
Supplementary experiments			
Fig. S8	both	extended sweeps, as Fig. 3a and 3b	5
Fig. S9	finger-space	softening, $[0.10, 0.60]$, $\alpha = 0,\ 0.3,\ 2.0$ N^{-1}	5
Fig. S10	task-space	sigmoidal and polynomial laws on the fingertip element, joint elements disabled	5
Fig. S11	task, mixed	40 random trials; $K_t \in [10, 40]$ N/m, $K_\theta \in [0.01, 0.20]$ N $\cdot$ m/rad; 1.5 s averaging	40

Table S5: **Virtual element configuration per experiment, ADAPT Hand**. One row per figure panel, giving the element configuration, its parameters, and the number of independent repetitions N.

Panel	Configuration	Parameters	N
Passive compliance			
Fig. 4a	joint-space	$K_\theta = 0.05,\ 0.20,\ 0.60$ N $\cdot$ m/rad; strum 0.05 m at 0.30 m/s; ramp 3 s	1
Fig. 4b	joint-space	$K_\theta = 0.05,\ 0.30$ N $\cdot$ m/rad; 3×100 g; 5 s log after 3 s settle	1
Online modulation			
Fig. 6a	task-space	uniform 10 N/m $\rightarrow$ radial/ulnar 200 vs 0.1 N/m; thumb at a quarter of the finger stiffness; background $K_\theta = 0.1$; ramp 1 s, record 5 s	1
Fig. 6b	task-space	$K_t = 0.1$ (soft), 150 (stiff), soft$\rightarrow$stiff after closure (adaptive); arm 0.50 m at 0.08 m/s, close at 0.20 m	1
Sensing and force control			
Fig. 7c	task-space	probe $K_{\text{sensing}} = 20$ N/m; sweep 50, 100, 200 N/m; others held at 100 N/m; record 5 s	5
Fig. 9a, b	task-space	close at $K_t = 40$ N/m; $\mathbf{K}_d$-descent $\alpha = 10^{-5}$, $\leq 5\%$ change per tick; targets 0.80, 0.20, 0.02 N; converge below 0.07 N for 1 s; descend 0.15 m	1
Controller validation			
Fig. 10d	joint-space	stiff architecture on all kinematic joints; PC_1 and PC_2 targets	1
Supplementary experiments			
Fig. S7	task, mixed	force-descent convergence, index and thumb, three configurations	—
Fig. S13	task-space	time-resolved force and K_n during the apple grasp	1

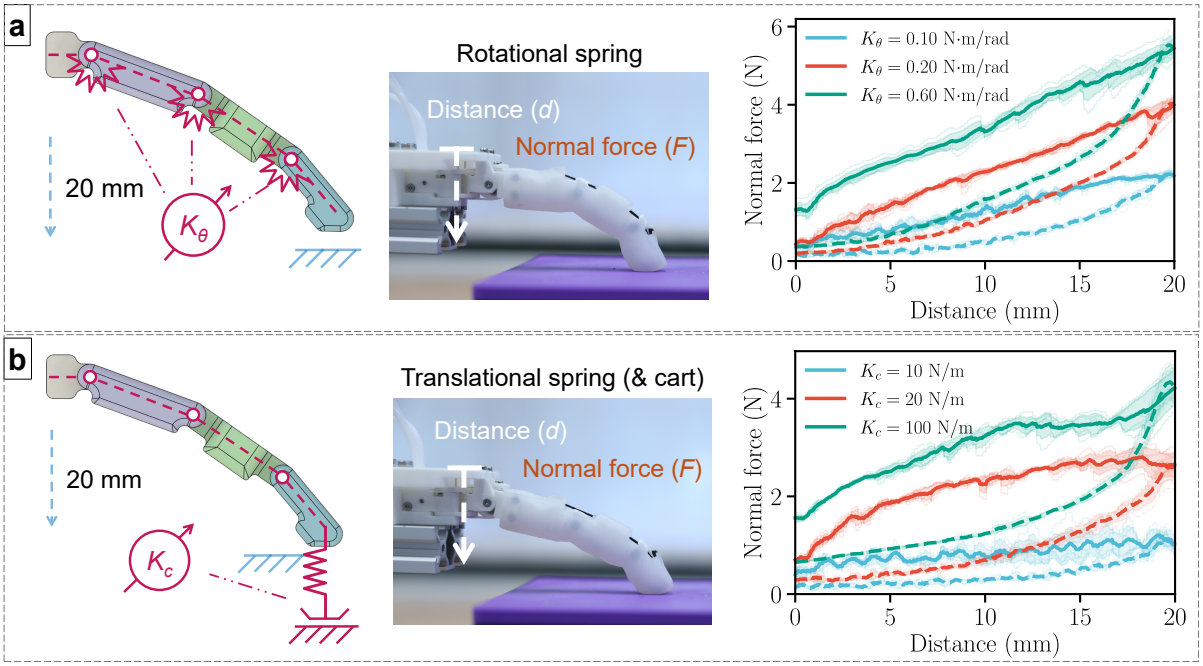


Figure S7: **Extended stiffness sweep on the single-finger platform**. **a** Normal force-displacement profiles for the torsional virtual spring at the finger joints, for $K_\theta = 0.10$, 0.20, and 0.60 N $\cdot$ m/rad. Loading (solid) and unloading (dashed). **b** Normal force-displacement profiles for the translational (cartesian with sliding cart) virtual spring at the fingertip, for $K_c = 10$, 20, and 100 N/m. Loading (solid) and unloading (dashed).

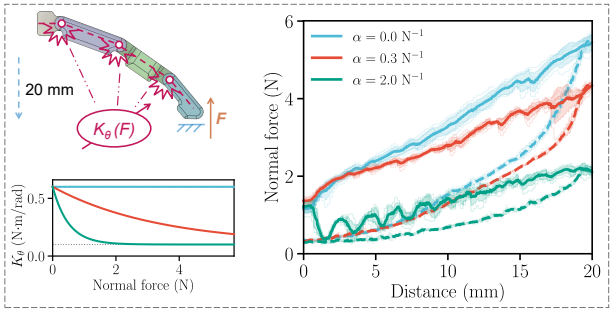


Figure S8: **Softening of the virtual stiffness under contact**. Torsional stiffness at the finger joints decreases with contact force, from $K_{\text{max}} = 0.60$ to $K_{\text{min}} = 0.10$ N $\cdot$ m/rad, for various softening rates, and resulting normal force-displacement curves. Loading (solid) and unloading (dashed).

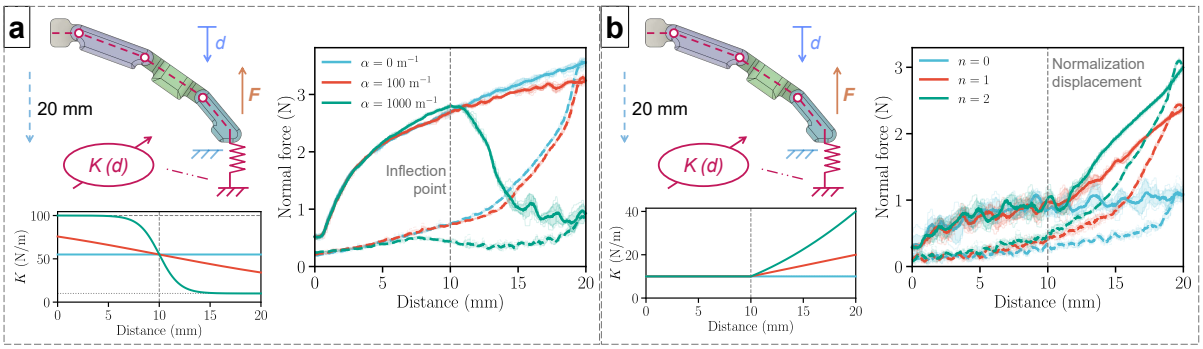


Figure S9: **Displacement-dependent stiffness laws: sigmoidal switch and polynomial increase**. **a** Sigmoidal stiffness law transitioning between a maximum and a minimum stiffness around an inflection point, for different steepness. **b** Polynomial stiffness law of increasing order in displacement, and resulting normal force-displacement curves, normalized to the reference displacement.

D.3: Sigmoidal and polynomial stiffness sweep

Stiffness may also be scheduled on displacement rather than on force, which requires no force measurement at all and, by Eq. (S7), preserves passivity. Fig. S9 reports two such laws applied to a single task-space element at the fingertip. The sigmoidal law of Eq. (S9) switches between two regimes around a threshold displacement, the rate α setting the sharpness of the transition (Fig. S9**a**). The polynomial law of Eq. (S8) grows as a power of normalized displacement, clamped below at K_{min} when d is lower than 10 mm. The order p sets how superlinear the response becomes (Fig. S9**b**). Both shape the force-displacement curve into forms unattainable with a fixed linear element, using the same hardware and only a change of software.

D.4: Force prediction for various VMC configurations

The transmission efficiency was identified on the finger-space configuration. We tested whether it transfers to the others. Fig. S10 shows the task-space (Fig. S10**a**) and mixed-space layouts (Fig. S10**b**). In each, forty trials were run with stiffness drawn uniformly from $[10, 40]$ N/m in task space and $[0.01, 0.20]$ N $\cdot$ m/rad in joint space, each trial averaged over a 1.5 s window

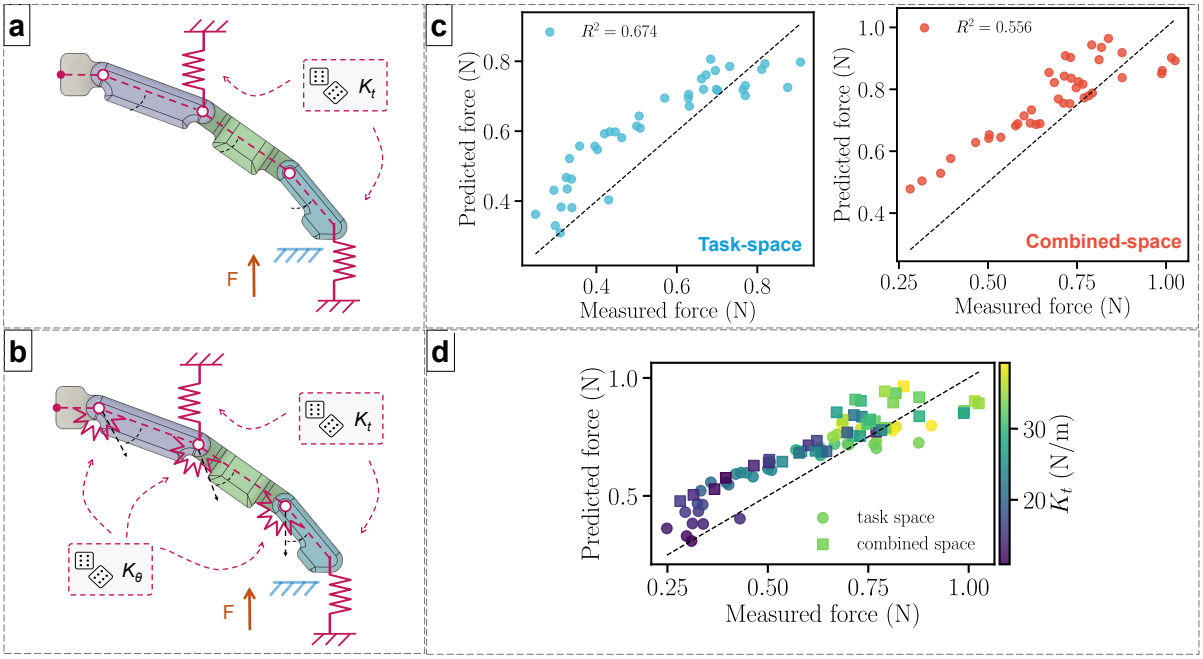


Figure S10: **Force prediction accuracy for task-space and combined-space VMC configurations.**. **a** Task-space virtual element configuration, with cartesian spring at the finger joints. **b** Combined-space configuration, superimposing task-space and joint-space virtual elements. **c** Predicted versus measured normal force for the task-space (left) and combined-space (right) configurations, across randomized stiffness trials. **d** Combined scatter of predicted versus measured force for both configurations, colored by the task-space stiffness K_t.

after settling. Fig. S10**c** compares predicted against measured normal force, while Fig. S10**d** combines the two scatter plots of both configurations, colored by the task-space stiffness K_t. Although with a lower accuracy compared to the baseline, the prediction maintains an accuracy above 67% and 55% in the two respective cases, as $\boldsymbol{\eta}$ characterizes the transmission rather than the particular choice of virtual elements. This licenses its use in the hand experiments, where the elements are cartesian rather than torsional.

E: Description of videos

Supplementary Movie 1: Programmable passive compliance with torsional virtual elements. Single-finger test bed under torsional virtual springs at MCP, PIP, DIP. The arm presses the finger onto the load cell and returns while the shared stiffness K_θ is varied between trials.

Supplementary Movie 2: Programmable passive compliance with cartesian virtual elements. Single-finger test bed under a cartesian virtual spring at the fingertip, constrained to a virtual cart. The arm presses the finger onto the load cell and returns while the stiffness K_c is varied between trials.

Supplementary Movie 3: Guitar strumming across stiffness regimes (with sound). The ADAPT Hand holds a fixed posture under torsional virtual springs while the arm performs a single upward strum. The posture before contact is identical in all three trials; only the virtual stiffness differs.

Supplementary Movie 4: Weight bearing under soft and stiff control. The hand holds a hook posture while an operator adds three 100 g loads in succession, first under a compliant and then under a stiff controller.

Supplementary Movie 5: In-hand manipulation by stiffness redistribution. The hand grasps a printed helicoidal cylinder at uniform fingertip stiffness, then redistributes stiffness towards the radial and subsequently the ulnar digits. The object reorients with no change of grasp pose.

Supplementary Movie 6: Dynamic grasping under three stiffness schedules. The arm translates continuously at 8 cm$/$s while the hand closes onto a yarn ball without interrupting the

motion, under a stiff, a soft, and an adaptive schedule.

Supplementary Movie 7: Sensorless estimation of object compliance. The hand grasps a rigid printed sphere, a kitchen sponge, and a yarn ball, probing each at low thumb stiffness and then squeezing at increasing thumb stiffness while the opposing digits hold.

Supplementary Movie 8: Grip-force regulation while picking an apple. The hand closes on an apple suspended from an elastic band and adapts its fingertip stiffness by gradient descent towards a firm, medium, or light force target, before the arm descends and loads the band.

Supplementary Movie 9: Replication of passive elastic fingers. Force-displacement characterization of the two printed TPU fingers used as physical references, for both the soft and hard passive mechanisms.

Supplementary Movie 10: Pose tracking in free space. With no contact, the same virtual elements act as a distributed position controller. Two targets are tracked, taken from the first two principal components of human grasp postures, with no mode switch separating this regime from other ones.

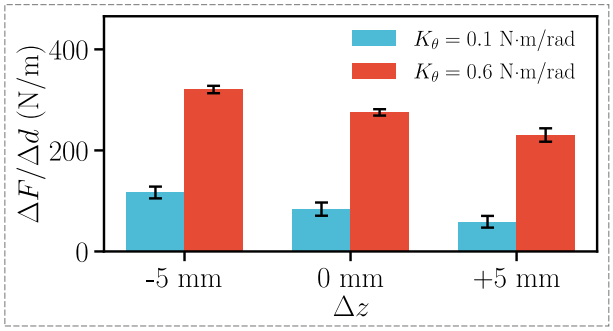


Figure S11: **Effective stiffness of the torsional virtual spring across initial finger poses**. Effective stiffness for the shifted initial poses ($\Delta z = -5$, 0, $+5$ mm) of Fig. 3**c**, for $K_\theta = 0.1$ and 0.6 N $\cdot$ m/rad.

F: Description of further results

This section reports additional results related to the experiments of the main text:

1. **Effective stiffness during pose sweep**

2. **Force and stiffness evolution during grasp adaptation**

F.1: Effective stiffness during pose sweep

Fig. S11 reports the effective stiffness $\Delta F/\Delta d$, obtained by linear regression of force against imposed arm displacement over the descent window, for the three initial arm heights and both virtual stiffnesses. The effective stiffness increases as the finger begins closer to the plate, since the torsional elements are already more deflected at the onset of contact, and the separation between the two K_θ conditions is preserved across poses. Modulation authority is therefore retained across the workspace even though absolute values shift with configuration, a direct consequence of the configuration dependence of $\mathbf{J}_x$ in Theorem 1.

F.2: Force and stiffness evolution during grasp adaptation

Fig. S12 resolves in time what the main text reports only at its endpoints for the apple grasp experiment. Fig. S12**a** shows the mean estimated fingertip force during gradient-descent adapta-

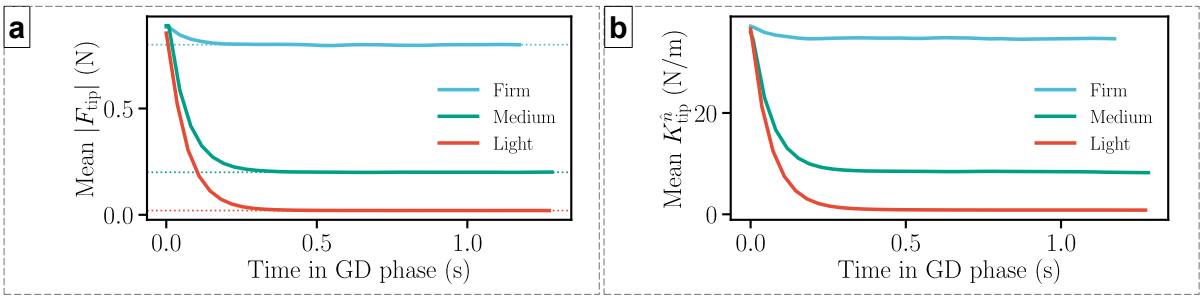


Figure S12: **Time evolution of the estimated fingertip force and stiffness during gradient-descent adaptation of the apple grasp**. **a** Mean magnitude of the estimated fingertip force during the gradient-descent adaptation phase, for the firm, medium, and light grasp targets (cf. Fig. 9). **b** Mean estimated fingertip stiffness, projected onto the normal direction, during the same adaptation phase for the three grasp conditions.

tion for the firm, medium, and light targets. Fig. S12**b** shows the corresponding mean estimated fingertip stiffness, projected onto the contact normal as $K_n = \mathbf{n}^T \mathbf{K}_x \mathbf{n}$. All three conditions converge monotonically and without overshoot, the light target requiring the largest excursion in stiffness. The stiffness trajectories make explicit what the force targets imply mechanically: the three grasps differ not only in the force applied to the apple but in the stiffness with which that force is defended against the elastic disturbance, and it is the latter that determines when the hold is lost during the descent.

Supplementary Files

This is a list of supplementary files associated with this preprint. Click to download.

- Supplementaryhandvirtualmodelcontrol.pdf
- Supplementarymovie2.mp4
- Supplementarymovie1.mp4
- Supplementarymovie3.mp4
- Supplementarymovie9.mp4
- Supplementarymovie5.mp4
- FigureS1.svg
- Supplementarymovie4.mp4
- FigureS2.svg
- FigureS3.svg
- FigureS6.svg
- FigureS8.svg
- FigureS4.svg
- FigureS10.svg
- FigureS11.svg
- FigureS12.svg
- FigureS5.svg
- FigureS9.svg
- Supplementarymovie7.mp4
- Supplementarymovie10.mp4
- FigureS7.svg
- Supplementarymovie8.mp4
- Supplementarymovie6.mp4